

GEOPHYSICAL INVESTIGATION AND ASSESSMENT OF THE RYE PATCH KNOWN
GEOTHERMAL RESOURCE AREA, RYE PATCH, NEVADA

by

Mark Richmond McDonald
Bachelor of Science, University of North Dakota, 1986
Master of Science, University of North Dakota, 1994

A Dissertation

Submitted to the Graduate Faculty

of the

University of North Dakota

In partial fulfillment of the requirements

for the degree of


Doctor of Philosophy

Grand Forks, North Dakota

December
2013

Copyright 2013 Mark R. McDonald

This dissertation, submitted by Mark R. McDonald in partial fulfillment of the requirements for the Degree of Doctor of Philosophy from the University of North Dakota, has been read by the Faculty Advisory Committee under whom the work has been done and is hereby approved.



William D. Gosnold
Chairperson




Richard D. LeFever



Michael D. Mann




Ronald K. Matheney



Hossein Salehfar

This dissertation is being submitted by the appointed advisory committee as having met all of the requirements of the School of Graduate Studies at the University of North Dakota and is hereby approved.



Wayne Swisher
Dean of the School of Graduate Studies



Date

Title: Geophysical Investigation and Assessment of the Rye Patch Known Geothermal Resource Area, Rye Patch, Nevada

Department: Geology and Geological Engineering

Degree: Doctor of Philosophy

In presenting this dissertation in partial fulfillment of the requirements for a graduate degree from the University of North Dakota, I agree that the library of this University shall make it freely available for inspection. I further agree that permission for extensive copying for scholarly purposes may be granted by the professor who supervised my dissertation work or, in his absence, by the Chairperson of the department or the dean of the School of Graduate Studies. It is understood that any copying or publication or other use of this dissertation or part thereof for financial gain shall not be allowed without my written permission. It is also understood that due recognition shall be given to me and to the University of North Dakota in any scholarly use which may be made of any material in my dissertation.

Mark R. McDonald
December 12, 2013

TABLE OF CONTENTS

LIST OF FIGURES.....	vii
LIST OF TABLES.....	ix
ACKNOWLEDGMENTS.....	x
ABSTRACT.....	xi
 CHAPTER	
I. INTRODUCTION.....	1
Purpose.....	1
Location.	1
History.....	4
Hypothesis.....	9
II. PREVIOUS STUDIES.	10
III. GEOLOGY.	21
Regional Overview.	21
Physiography.	21
Regional Geology.....	22
Basin and Range Structure.....	26
Geothermal Setting.....	29
Research Area.....	31

	Lithology	31
	Structure	37
	Geothermal Setting	39
IV.	METHODOLOGY AND RESULTS	45
	Introduction	45
	Station Locations - Global Positioning System	48
	Gravity	49
	Ground-Based Magnetics	76
	Modeling	80
V.	DISCUSSION AND CONCLUSIONS	93
	APPENDIX A - WELL LOGS	100
	APPENDIX B - STATION LOCATION DATA	106
	APPENDIX C - GRAVITY DATA	114
	APPENDIX D - MAGNETIC DATA	126
	REFERENCES	136

LIST OF FIGURES

Figure	Page
1. Map Showing Location of Rye Patch in Pershing County, Nevada..	2
2. Geographical and industrial features of the Rye Patch KGRA..	3
3. Well locations in the vicinity of the Rye Patch geothermal power plant.	8
4. Seismic section from Vertical Seismic Profile study north of the existing geothermal plant.	20
5. Approximate extent of orogenic belts.	24
6. Generalized cross-section of typical Paleozoic/Mesozoic thrust faulting followed by Cenozoic normal faulting.	28
7. Hypothetical cross-section of typical Basin and Range listric normal faulting, fracturing, and magmatism.	28
8. Illustrations of transfer zones and accommodation zones.	29
9. Three possible scenarios for shallow geothermal fluid movement in the Basin and Range..	32
10. Generalized stratigraphic column of rocks exposed in the Humboldt Range..	34
11. Hypothetical structural cross-section based on well and seismic data.	40
12. Temperature gradients and formation tops from a number of wells near the existing geothermal plant..	42
13. Station locations from the 2008 and 2012 gravity surveys.	46
14. Simple Bouguer anomaly map.	58
15. Shaded relief map of the digital elevation model with surface fault traces.	59

16. Terrain corrected - complete Bouguer anomaly map.....	62
17. Quadratic polynomial trend surface map of terrain corrected gravity anomaly data.....	63
18. Map of the terrain corrected anomaly data less the quadratic polynomial trend surface.....	64
19. Wavelength filtered map with filter window from 0.1 to 10 km.....	67
20. Wavelength filtered map with filter window from 0.1 to 8 km.....	68
21. Wavelength filtered map with filter window from 0.1 to 6 km.....	69
22. Wavelength filtered map with filter window from 0.1 to 4 km.....	70
23. Wavelength filtered map with filter window from 0.1 to 2 km.....	71
24. Decultured aeromagnetic anomaly map.....	72
25. Aeromagnetic anomalies (contours)	73
26. Graph of 2nd derivative along profile through Rye Patch and Range Front Faults.....	75
27. Graph of anomaly half-width across Rye Patch and Range Front Faults.....	75
28. Ground-based magnetic anomaly map.	81
29. Aeromagnetic anomalies (contours) over ground-based magnetic anomalies (colors).....	82
30. Ground-based magnetic anomalies (contours) over gravity anomalies with a wavelength filter of 0.1 to 4 km (colors).....	83
31. Locations of modeling profiles..	85
32. Model results for profile A-A'	88
33. Model results for profile B-B'	90
34. Model results for profile C-C'.....	91
35. Shaded relief map of 1 to 4 km filtered gravity anomalies.....	95

LIST OF TABLES

TABLE	PAGE
1. Density and magnetic susceptibility values used in modeling	87
2. GPS Data	107
3. Gravity Data	115
4. Magnetometer Data	127

ACKNOWLEDGMENTS

I wish to express my sincere appreciation to the members of my advisory committee for their guidance and support during my time in the doctoral program at the University of North Dakota. In particular, I am extremely grateful to Dr. William Gosnold who provided funding for the project and research assistantship financial support during my time with the department in addition to the opportunity to further my education. I also express my appreciation to Richard Ellis and Presco Energy who provided data and partial funding for the project and to the Florida Canyon Mine which allowed access to portions of the study area. Finally, I express my sincere gratitude to Eric Zimny and Godswill Njoku for their assistance in the field components of this work.

To my children Jenna, Jamie, and Richmond,
for their love, support, and patience

ABSTRACT

A gravity and ground-based magnetic survey was conducted at the Rye Patch Known Geothermal Resource Area located at Rye Patch, Nevada. The purpose of the study was to attempt to further delineate the geothermal reservoir and/or to identify potential drilling targets. The survey consisted of collecting data at 264 new stations to augment data from 203 stations collected in 2008. Information from previous seismic, aeromagnetic and geochemical investigations was also examined and incorporated. Filtering methods including removal of a polynomial trend surface and wavelength filtering were utilized on the gravity data to remove the strong regional overprint caused by the large density contrast between the low density alluvium within the valley versus the near-surface higher density rock in the higher elevations. After filtering, the Rye Patch Fault, the Range Front Fault, an east-west trending feature at the location of "southeast" fault, and another possible fault at the southern end of the study area are observable in the Rye Patch geothermal anomaly area. In the Humboldt House anomaly area, the northeast trending features identified by MacNight et al. (2005) and Ellis (2011) are not discernable although there is a significant gravity low in this area. Based on estimates arrived at by using 2nd derivative methods, fault dip angles are on the order of 80° and are consistent with previous conceptual models of the site. Computer modeling indicates that the fault blocks may also be rotated back to the east. Due to errors in

collecting diurnal information, the ground-based magnetic information was of limited use. Anomalies identified with the magnetic data do however correlate with the locations of anomalies identified using gravity and aeromagnetic surveys. Results indicate that gravity methods can be an effective method of defining approximate fault locations, lengths, and approximate trends and dip angles.

CHAPTER I - INTRODUCTION

Purpose

The purpose of this study was to attempt to further characterize the Rye Patch Known Geothermal Resource Area (KGRA) and/or to identify potential drilling targets in the area by delineating approximate fault locations, lengths, trends and dip angles. Gravity and ground-based magnetic surveys are augmented with existing seismic, aeromagnetic, remote sensing, and geochemical data.

Location

The Rye Patch KGRA is located along U.S. Interstate 80 approximately 190 km northeast of Reno, Nevada between the cities of Winnemucca and Lovelock, Nevada (Figure 1). It includes what has been referred to as the Humboldt House geothermal anomaly to the north and the more southerly Rye Patch geothermal anomaly. It is bounded on the west by the Humboldt Range and on the east by the Rye Patch Reservoir (Figure 2). The northern boundary of the KGRA is demarcated by the northeast-trending Midas Lineament and the southern boundary by a northwest-trending fault zone that offsets the Humboldt Range from the West Humboldt Range located to the south (Waibel et al., 2003). Ellis (2011) refers to these northern and southern structural features as sinistral slip faults.

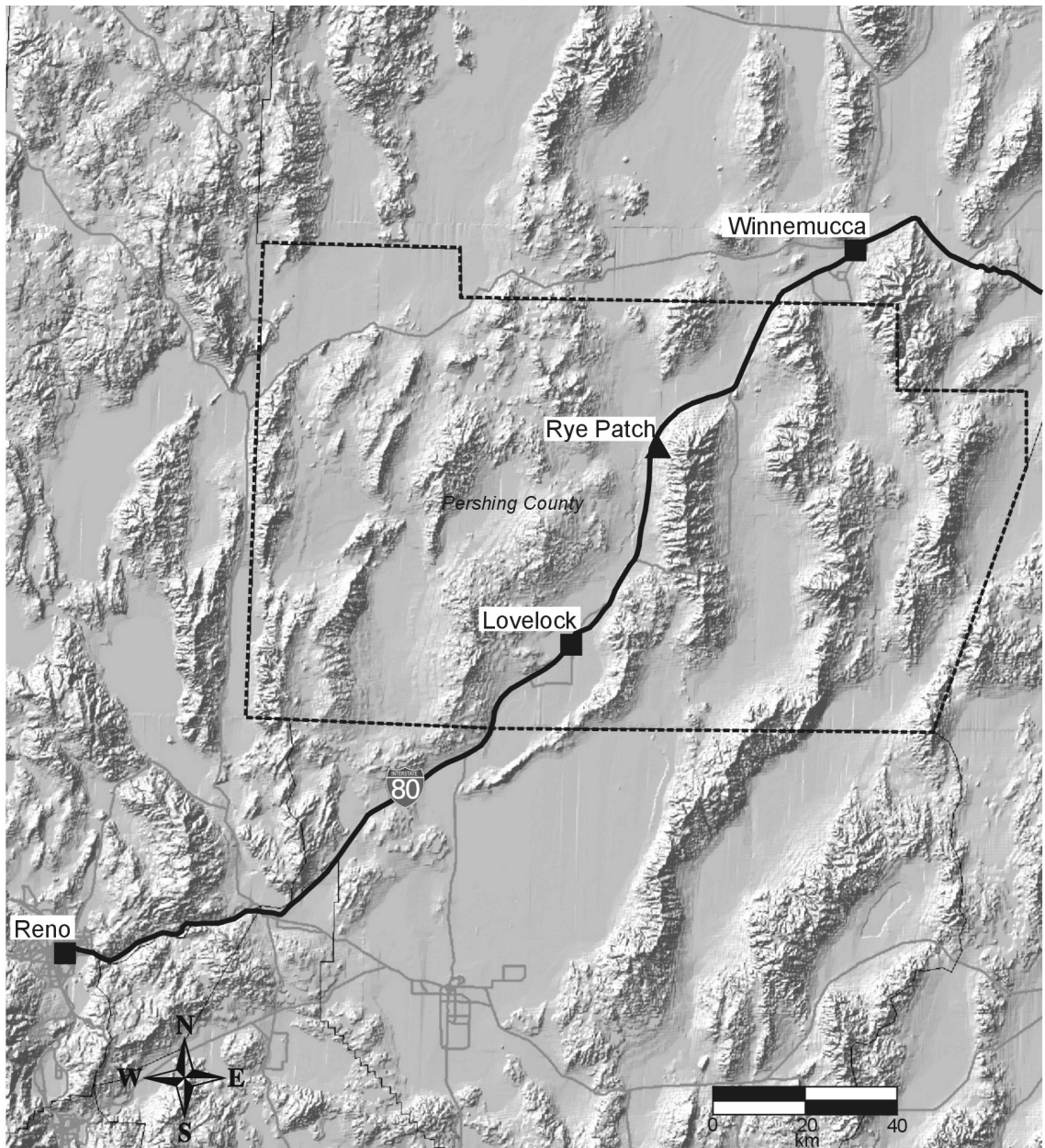


Figure 1. Map Showing Location of Rye Patch in Pershing County, Nevada.

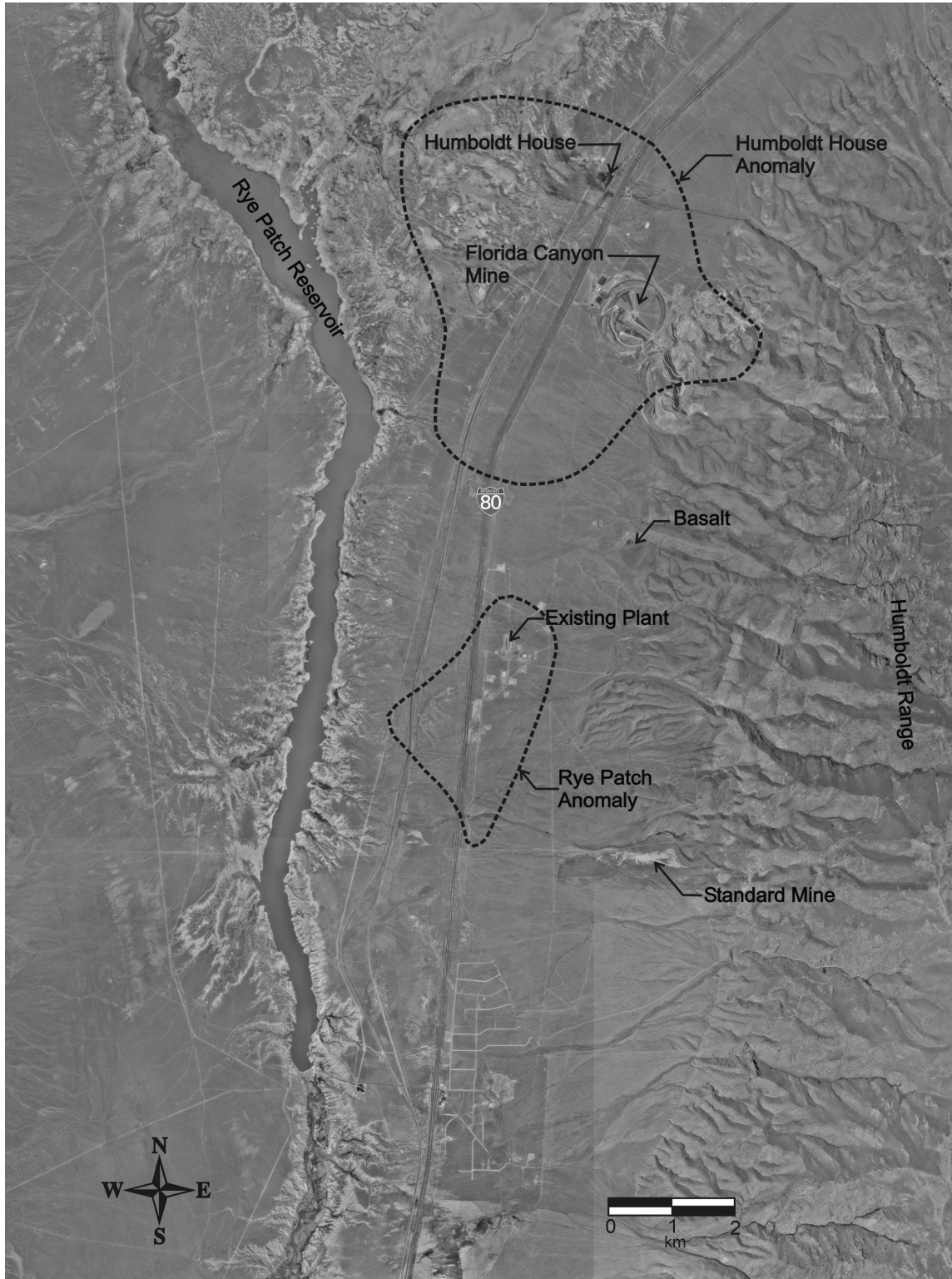


Figure 2. Geographical and industrial features of the Rye Patch KGRA.

History

The first documented reference to the geothermal characteristics of the area was by Croffut in 1872. Specifically, Croffut (1872) notes that at a railroad signal flag station located 11 miles south of the Humboldt House, “to the left of the road, against the hill side, is another hot spring, over whose surface a cloud of vapor is generally floating”. He continues by stating that “a cabin has been erected on the green slope below the spring, as evidence that the property has been appropriated”. As the train would have been heading south traveling from the Humboldt House to the Rye Patch flag station, “left of the road” would be to the east toward the Humboldt Range. This would place the location of the fumarole in Section 21 or 22, T30N, R33E. A review of aerial photographs indicates that a more densely vegetated area appears to be located in Section 21 close to the existing intersection of Old Victory Highway and Humboldt Trail. However there is no other visible evidence of an active hot spring or fumarole in the area.

In addition, siliceous and calcareous sinter deposits occur south and east of the Humboldt House (Vanderburg, 1936; Garside and Schilling, 1979). These hot-spring deposits are also noted by the above authors as containing gypsum, sulfur and detectable amounts of mercury. Specifically, two are described as being located in the SW/4, SE/4, S33, T32N, R33E and NW/4, SW/4, S32, T32N, R33E (Olcutt and Spruck, 1961, as cited by Garside and Schilling, 1979). More deposits in the same area were identified by LiDAR and hyperspectral analysis performed and reported by MacKnight et al. (2005) and Silver et al. (2011).

An old mineral exploration well where warm water (76°C) flows at a rate of about $19 \text{ l}\cdot\text{s}^{-1}$ is also reported in the literature (Desormier, 1979; Benoit and Butler, 1983; Waibel et al., 2003). Desormier (1979) further describes the well as being drilled by Estoril in the SE/4, S32, T32N, R33E, that it is flowing with sodium chloride water, and that the silica and Na-K-Ca geothermometers give estimated reservoir temperatures of 232°C to 254°C.

Desormier (1979) and Benoit and Butler (1983) report that a regional shallow temperature-gradient drilling program (< 20 m) was also conducted by Phillips Petroleum Company in 1974. The drilling program resulted in the identification of the Humboldt House and Rye Patch thermal anomalies (Figure 2) and Phillips Petroleum Company drilled the first geothermal production well in November 1977 in the Rye Patch geothermal anomaly area. Desormier (1979) states that the resulting well, designated as Campbell E-1, was drilled to a depth of 560 m and that it is cased until the final 25 m. He also reports that during an initial flow test, the Campbell E-1 well produced 183°C fluid at a rate of approximately $6050 \text{ l}\cdot\text{min}^{-1}$. Benoit and Butler (1983) also report that the well had a high shut-in pressure of approximately 1030 kPa.

On the basis of the sinter deposits, the above noted mineral exploration well, the geothermal gradient study, and the Campbell E-1 well, the area was designated as the Rye Patch KGRA by the USGS (Muffler, 1978). KGRA is a special designation that was defined in the Geothermal Steam Act of 1970 as “an area in which the geology, nearby discoveries, competitive interests, or other indicia would, in the

opinion of the Secretary, engender a belief in men who are experienced in the subject matter that the prospects for extraction of geothermal steam or associated geothermal resources are good enough to warrant expenditures of money for that purpose” (Godwin et al., 1971).

According to Desormier (1979) two additional production wells were drilled in 1978 and 1979. In 1978, Union Oil Company drilled the Campbell No. 1 well to the north in the Humboldt House geothermal anomaly in the NE/4, S3, T31N, R33E to a depth of 2080 m. Benoit and Butler (1983) report that this well had measured temperatures of approximately 205°C but it only produced 0.17 l·s⁻¹. Phillips Petroleum Company drilled the Campbell E-2 well north of Campbell E-1 to a depth of 2450 m, and also drilled 40 temperature gradient and/or stratigraphic wells to depths of 90 to 610 m across the KGRA (Benoit and Butler, 1983). The E-2 well was essentially a dry hole (Desormier, 1979; Waibel et al., 2003). Benoit and Butler (1983) further state that “these two wells (Campbell E-2 and Campbell No. 1) encountered thick sections of the Triassic Auld Lang Syne Group – shales, slates and phyllites which appear too incompetent to maintain fracture permeability”. They continue by stating that “thick sequences of siliceous sinter have been found interbedded within the Quaternary alluvium and underlying Paleogene and Neogene lacustrine sedimentary rocks in both wells and deep temperature-gradient holes, indicating a long history of geothermal activity at Humboldt House.”

Commercial development of the KGRA was initiated in 1991 and, on the basis of the 40 temperature gradient wells drilled by Phillips Petroleum Company

mentioned above, a successful production well (44-28) was drilled (Waibel, et al., 2003). The success of this well led to the construction of a 12.7 MW capacity power plant by Ormat Energy Services, Inc. (Gritto et al., 2002). Waibel et al. (2003) note that seven additional production wells were drilled concurrently with the plant's construction in the vicinity of the successful well (Figure 3). However, the seven new wells were either too cold or did not produce sufficient quantities of geothermal fluids to operate the plant (Feighner et al., 1999; Gritto et al., 2003).

A number of studies have been conducted in an effort to characterize the geothermal reservoir and to site new, more productive wells. These studies will be discussed in more detail in the following chapter. Waibel et al. (2003) do however report that an additional well (72-28) that was located on the basis of additional thermal gradient wells was successful. Waibel et al. (2003) report that this well is rather shallow and is of relatively low temperature.

Due to the close spacing of the wells (within an area less than 2.6 km²) with one successful well and the remainder unsuccessful with respect to operation of the plant, it has been postulated that the distribution of the reservoir fluids is controlled by fractures and faulting (Gritto et al., 2002) which is in keeping with the general conceptual models of the geothermal systems in this area of the Basin and Range Province (Blackwell et al., 1999). Waibel et al. (2003) present a conceptual model specific to the Rye Patch geothermal system and Ellis (2011) has further refined this model.

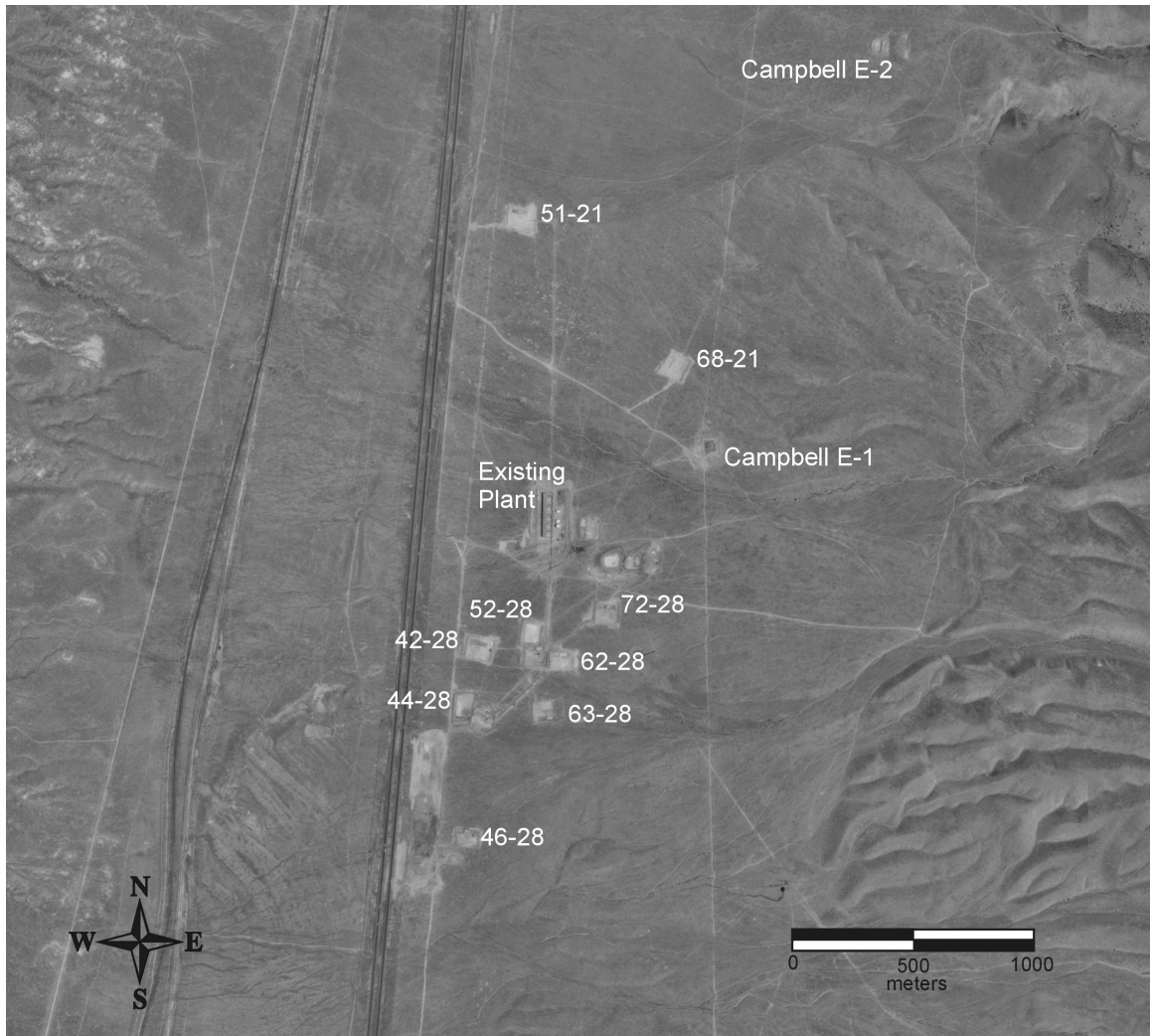


Figure 3. Well locations in the vicinity of the Rye Patch geothermal power plant.

After the initial exploration and reservoir evaluation efforts by Phillips Petroleum Company, the plant and property has exchanged hands a number of times. Presco Energy, LLC, the current owner, acquired the property from Mt. Wheeler Power in 2001.

Hypothesis

I hypothesize that a high resolution gravity survey in combination with a ground-based magnetic survey will better define the locations, trends, lengths, and dip angles of faults and possible solution cavity features and thus lead to the identification of potential geothermal drilling targets. By incorporating other geologic, geophysical and geochemical data, I propose to show that the methodology may be used to develop realistic site models at other locations where such information may be limited. At a minimum, I hypothesize that gravity methods can be used early in the exploration process to identify locations that would warrant further study by other methods and that it can be a valuable tool in geothermal prospecting.

CHAPTER II - PREVIOUS STUDIES

The early history of the geothermal area and exploration efforts prior to the construction of the power plant was discussed in Chapter I. A number of other investigations and studies at the Rye Patch geothermal field both before and since construction of the plant have been conducted in an effort to better define the geothermal resource and to increase production of geothermal fluids to allow operation of the plant.

The earliest study found in the literature was an audiomagnetotelluric study conducted by Long and Batzle (1976). The data are reported in an U.S. Geological Survey open-file report (76-700c) which includes a map of the station locations and copies of hand recorded values for the apparent resistivity at various frequencies. No analysis or interpretation of the data was found during a subsequent literature search.

Sibbett and Glenn (1981) produced a detailed description of the cuttings and well logs from Phillips Petroleum Company's Campbell E-2 well. Based on the lithologic log and surface geology, they also prepared a cross section extending from west of the well eastward into the Humboldt Range and provided two possible interpretations of the subsurface along the cross section. Their principle conclusions were:

- that it seemed unlikely that a geothermal reservoir exists in the horst block of the Humboldt House anomaly area principally on the basis that all known sinter deposits occurred in the graben block northwest and southwest of the Campbell E-2 well and due to the range front fault dipping to the west; and,
- that the Grass Valley and Auld Lange Synne Group are generally fine-grained argillaceous and slaty rocks with very low intergranular permeability and that they may not be competent enough to maintain sufficient fracture permeability.

A gravity survey was also conducted at the site in 1981 with the data reported in another U.S. Geological Survey open-file report (Duffrin et al., 1985). A total of 172 gravity stations were occupied along four major transects and several offshoots across the valley between the Humboldt Range on the east and the Trinity and Antelope Ranges on the west. Schaefer (1986) produced a map of the Bouguer gravity anomalies, depth to bedrock, and shallow temperatures based on the gravity readings, thirty shallow-temperature measurements (two meters in depth) and six seismic lines.

A report of the integrated geophysical studies that had been performed at the site prior to 1999 was prepared for Mt. Wheeler Power by Teplow (1999). However, a copy of this report was not available for review at the time of preparation of this paper. Gritto (2002) reports that interpretation of 3-D seismic reflection data from the Teplow (1999) report indicated the location of a possible

fault with a strike of N 76° W and a dip of 73° NE. The paper also reportedly included a gravity survey that consisted of 334 stations that calculated the Bouguer residual by subtracting a best fitting plane of the regional trend from the individual stations to obtain the local gravity trends. Gritto et al. (2002) interpreted an anomaly shown on the residual map as a mass excess of the uniform sloping plane of the Triassic basement rocks. They continue by stating that the mass excess could be the result of hydrothermal mineralization or an uplift of high-density basement rocks relative to the lower density overlying sediments. Feighner et al. (1999) also note that the Teplow report included self-potential (SP) and magnetic surveys.

Beginning in 1997, the Lawrence Berkeley National Laboratory (LBNL) conducted several studies in the vicinity of the Rye Patch power plant. Specifically, Feighner et al. (1998) performed a vertical seismic profile (VSP) at Well 46-28 (Figure 3) to determine the seismic reflectivity of the geologic strata and to obtain velocity information to be used in the design and subsequent processing of a proposed three-dimensional seismic survey. The results of the VSP indicated that coherent reflector beds were observed at two layers which, on the basis of corresponding lithologic well logs, they presumed to be from the permeable clastic unit within the Natchez Pass Formation and from the lower portions of the Natchez Pass Formation.

As these reflector beds were discernable, the project moved forward and a 3-D seismic imaging investigation was performed to “determine if modern seismic techniques could be successfully applied in geothermal environments” and “to map

the structural features which may control geothermal production in the reservoir” (Feighner et al. 1999). The 3-D survey covered an area of approximately 7.8 km² with 12 north-south receiver lines and 25 east-west receiver lines with a spacing of 245 m. The results indicated the presence of at least one dominant fault that was believed to be part of a graben structure and that may be controlling the migration of fluids to the reservoir (Feighner et al., 1999). They also report that the throw of the structure appears to be approximately 105 m at the northern end to 60 m at the southern end. Feighner et al. (1999) also note that an isolated velocity high occurs at a depth of between 90 and 120 m that coincides with the low SP anomaly and the intersection of two steep magnetic gradients, one trending to the northwest and the other to the south-southwest per Teplow’s 1999 report.

During the conduction of the 3-D seismic survey, in addition to the surface receivers, the LBNL also deployed a three component seismometer at a depth of 1190 m in well 46-28 (Gritto et al., 2000, 2001, 2002, 2003). This surface-to-borehole configuration recorded the waves generated by all of the surface sources in an effort to use the collected data to determine the subsurface structure as a function of azimuth by means of ray-path tracing. The results of this study confirmed the regional trend of the normal faulting in the area with a north-south strike and westward dip. They also identified a local disturbance that was striking in an east-west direction that they described as being at an elevation consistent with the interface between the carbonate basement and the overlying sedimentary sequence that they tentatively identified as being a fault.

In 2000, Mt. Wheeler Power (then owner of the site) received a grant from the DOE's Geothermal Resource Exploration and Definition Projects (GRED) program to test the productivity of the intersection of the Rye Patch fault with the east-west trending feature identified in the 3-D seismic survey (Mansure et al., 2001). The testing required the reopening of well 72-28 which had been temporarily abandoned at a depth of 298 m due to a lost circulation zone with high cross flows that prohibited deepening of the well to the desired completion depth. Prior attempts to seal the well with cement plugs had been unsuccessful so the reopening entailed using a polyurethane grout (Mansure et al., 2001). The grouting was successful between the depths of 223 to 230 m and the well was eventually deepened to 643 m although additional lost circulation zones were encountered between 230 m and the bottom of the well (Warpinski et al., 2004). Warpinski et al. (2004) also reported that the results of the well testing showed that the well was capable of producing $8460 \text{ l}\cdot\text{min}^{-1}$. They further estimated that the composite for the field would be capable of producing of $11,350 \text{ l}\cdot\text{min}^{-1}$ of geothermal fluid for 27 years at a temperature of between $150^{\circ}\text{C} - 179^{\circ}\text{C}$.

In 2002, Michels prepared a detailed report on the hydrogeochemistry of the thermal waters at the Rye Patch development. He performed a comprehensive evaluation of 82 sets of analyses from water produced from nine wells. Michels (2002) reported two features that he found particularly significant: 1) there was a substantial uniformity in the concentrations of sodium, potassium, chloride, lithium, and boron that he believed indicated a common heat source with a temperature of

274°C, and 2) that all of the fluids showed substantial depletion of silica content indicating precipitation of silica and reduction in permeability resulting in the hydraulic isolation of the “active” reservoir.

Michels (2002) also notes that the “active” reservoir is the principal source of the water that was produced during the well testing and that it is over pressured as the result of being sealed by an impervious cap and sides. He continues by stating that recharge to the bottom is “meager” and that circulation is driven by density gradients associated with cooling at the cap. Michels (2002) also states that some of the circulation flow moves through fracture (zones) and speculates that the upper part of the limestone reservoir near the cap has been partially dissolved. He also puts forth the idea that the lower portion of the “active” reservoir is isolated from the heat source by silica deposition resulting in a system of “stacked” reservoirs which leads him to estimate drilling depth required to reach the 274°C source water at between 2100 and 2440 m.

The University of Nevada Reno Great Basin Center for Geothermal Energy was awarded a grant from the DOE to work cooperatively with Presco Energy LLC and the Florida Canyon Mine to conduct research and to drill additional wells in an effort to expand the development on to Florida Canyon Mine property. From May to July 2003, they drilled five wells; one to 152 m, three to 305 m, and one to 457 m. A total of 564 m of core was obtained from the wells (Johnson et al., 2004; Nevada Bureau of Mines and Geology, 2005). The drilling report of the exploratory program provides a summary of the drilling conducted at the Humboldt House geothermal

anomaly near the Florida Canyon Mine and includes lithologic descriptions and gamma ray and temperature logs (Nevada Bureau of Mines and Geology, 2003).

Johnson (2003 as cited by Davis, 2011) and Johnson et al., (2004) originally logged and described the drill core and performed petrographic analyses and laboratory tests on the core. Analytical methods included Scanning Electron Microscopy (SEM) to determine mineral phase relationships; Inductively Coupled Plasma - Mass Spectroscopy (ICP-MS) for whole rock geochemistry to determine major, minor and trace elements; petrographic study of fluid inclusions, followed by laser ablation - ICP-MS; and x-ray diffraction (XRD) for clay identification (Johnson et al., 2004).

Davis (2011) re-logged, described, and sampled the core, and photographed the entire core set and samples for three of the above noted wells. In addition, cuttings and core from the interval from 198 - 306 m from well 3-1 were analyzed with infrared spectrometry by Calvin et al. (2010) in an effort to rapidly identify temperature dependent mineral assemblages including layered silicates, zeolites, opal, calcite and iron oxides and hydroxides. Their analyses identified weakly altered mafics, illite/chlorite, hydrated quartz/opal, kaolinite and jarosite.

In 2003, the University of California, Santa Cruz used hyperspectral imaging that was validated by field observations (ground truth) to detect and map hydrothermally associated minerals (MacKnight et al., 2005). They found a more abundant distribution of hot spring and fumarole deposits in the Humboldt River Valley than what was near the mountain ranges. They also postulated that the

linear distribution of the deposits implied a structurally controlled deposition and that the age could be constrained to Holocene sediments overlying all Lake Lahontan (Pleistocene) deposits. MacKnight et al. (2005) also note that the fault conduits that the geothermal fluids followed have since sealed and that the hot springs were therefore no longer active at the surface but that hydrothermal circulation was probably still active at depth where permeability was sufficient.

In 2005, the UC Santa Cruz group also acquired light detection and ranging (LiDAR) imaging information from the Humboldt River basin (Silver et al., 2011). By combining the LiDAR with the hyperspectral data discussed above, they were able to identify faults and paleo-shorelines of Lake Lahontan. In the area of the Rye Patch geothermal anomaly in the southern portion of the study area they identified a set of faults that displaced the surface of the alluvial fans and several that cut the paleo-shorelines. Silver et al. (2011) determined that the shorelines were at an elevation of 1290 m which corresponds to an age of $12,500 \pm 500$. However, they did not observe any signs of surface alteration in the Rye Patch anomaly area from their hyperspectral analysis. In the northerly Humboldt House geothermal anomaly area, they found abundant evidence of alteration including jarosite, hematite, montmorillonite, carbonate and siliceous sinter.

Silver et al. (2011) also identified at least two sand volcanoes and a field of low-carbonate mounds which they attributed to both recent and paleo-seismicity that initiated liquefaction. The authors state that while some may be fairly recent, it

is more likely to be associated with highstands of Lake Lahontan when the ground was saturated.

Sanyal et al. (2006) presented a conceptual model of the Rye Patch geothermal field utilizing lithologic, geophysical, and temperature logs in addition to production, injection and pressure data from the eight production wells. Their study identified a structure in the location of the east-west striking feature noted in the previous studies although the feature was mapped as trending more to the northeast than what had been presented in earlier studies. In their model, thermal fluid is believed to migrate up-dip in the permeable clastic unit from the west to the east. However they postulate that the pathway is diverted by the aforementioned fault to the southwest of well 44-28 from the east-southeast to the east-northeast along a relatively narrow channel. Continued up-dip flow results in the thermal water reaching an upper medium-enthalpy aquifer.

A recent magnetic survey was conducted by Presco Energy in 2008. The survey consisted of flying 867 line-kilometers encompassing an area of 124 km². It was flown with 150 m terrain clearance, and extensive deculturing (removal of man-made signals) was required to process the data. The results of the aeromagnetic survey have been incorporated into this study to provide a comparison of the aeromagnetic potential field with the gravity and ground-based magnetic anomalies identified herein.

Presco Energy also conducted new 2-D vertical seismic profiling using wells 51-21 and 68-21 as receiver wells and well 44-28 as a validation well. The VSP

used large, spatially dense vertical and horizontal apertures to develop optimal raypaths and a new algorithm was used to expedite processing. Presco also tried to dynamically cool the wellbore to decrease temperatures below the limits of the sensors. Even with the cooling, rapid receiver well reheating limited the vertical aperture and imaging was limited in the horizontal dimension due to heterogeneities and poor reflectivity. One result of the VSP was the identification of east dipping layers west of the well field which they postulate as indicating a series of antithetic faults. Prior conceptual models had the faults all dipping to the west. A summary of the aeromagnetic and VSP surveys is given in Ellis (2011) and Figure 4 shows one of the seismic sections produced by the VSP survey.

In 2011, Presco Energy deepened well 44-28 from 1059 m below ground level to 1275 m in an attempt to reach the postulated high enthalpy zone below the Natchez Pass clastic layer. The preliminary well testing after completion of the drilling indicated a weir flow rate of $2385 \text{ l}\cdot\text{m}^{-1}$ and a temperature of 200°C after 20 hours of pumping.

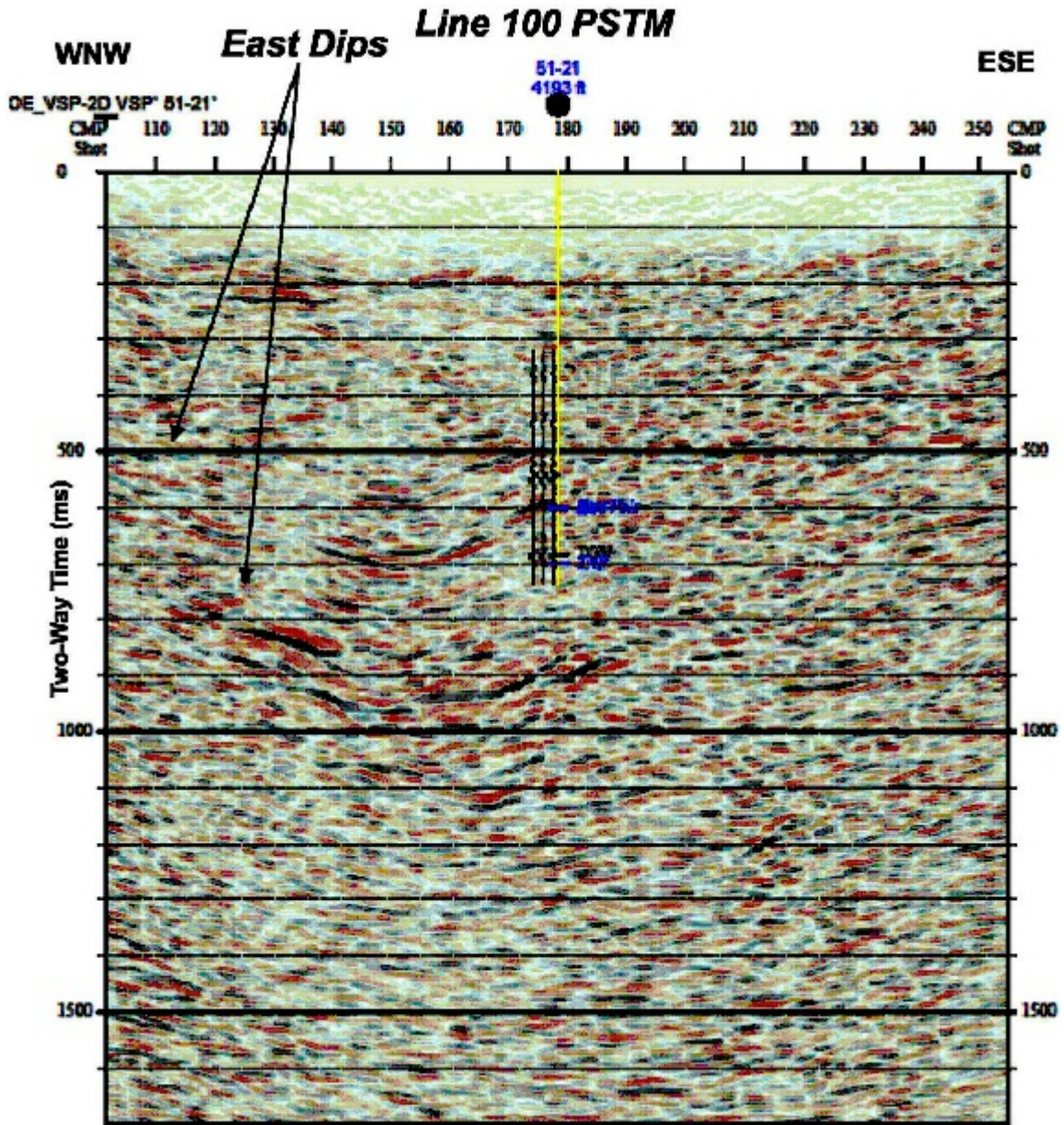


Figure 4. Seismic section from Vertical Seismic Profile study north of the existing geothermal plant (taken from Ellis, 2011).

CHAPTER III - GEOLOGY

Regional Overview

Physiography

The site lies within the Great Basin which is a portion of the Basin and Range geographical province. The Basin and Range as a whole occupies an area of approximately 775,000 km² and is typified by an anomalously thin crust, low upper mantle seismic wave velocities, regionally high elevations, and high heat flow all of which that can be attributed to crustal extension and subsequent normal faulting (Lachenbruch and Sass, 1978; Eaton, 1979; Wallace et al., 2008). Within the Great Basin, drainage is principally confined to enclosed basins and the only outlets to the sea are through the Colorado River system in the southern portion and the Snake River system in the northeast. In general, water discharges into the centers of the basins forming playas where it is ultimately returned to the atmosphere through evapotranspiration (Wallace, 1964). In the vicinity of the study area, drainage is to the Rye Patch reservoir and Rye Patch River system which ultimately discharges into the Humboldt Sink, a large playa lake that is a remnant of the deeper portions of Pleistocene Lake Lahontan (Thomas, 1964; Wallace, 1964).

The Great Basin is characterized by north or northeast trending arcuate mountain ranges alternating with wide valleys (Wallace, 1964; Stewart, 1998). Stewart (1998) states that the spacing between adjacent mountains is typically 30

km and that the valleys range in elevation from approximately 1,200 m to 2,000 m with the mountain crests ranging from 1,500 m to nearly 4,000 m. Broad alluvial fans are generally present at the base of the mountains grading from boulders to gravel to sand and silt at the base of the fans. The majority of the valley floors between the mountains and alluvial fans are playas which are often bordered by seeps and springs (Hunt, 1979).

Regional Geology

The oldest exposed rocks in Nevada are in the East Humboldt Range and have been dated to be greater than 2.5 Ga. The Precambrian rocks in Nevada are principally metamorphic and include gneiss, schist, and marble although granite and younger sedimentary rocks also outcrop in areas (Price, 2002). Price (2002) also states that beginning around 1.1 Ga, Antarctica and Australia may have rifted away from North America. Poole et al. (1992) and Miller et al. (1992) present a model where rifting began in the Proterozoic. They also conjecture that highlands developed from thermal bulging at the edge of the rifting which resulted in erosion and terrigenous detrital deposition along the continental margin during the Late Proterozoic and Cambrian. Igneous rocks and diamictite and other sedimentary rocks were deposited within intra-rift valleys (fault bounded basins) as spreading continued. These deposits form the Belt Supergroup which consists of argillite, shale, siltstone, quartzite, dolostone, limestone, conglomerate and thin mafic and gabbroic lavas or diabase sills (Poole et al., 1992).

From the Mid-to-Late Cambrian up to the Devonian, the region is believed to have been a passive margin that, in addition to the carbonate shelf, also had deep embayments, river deltas and estuaries. The general sedimentary record consists principally of alternating siliciclastic to carbonate deposits related to cycles of transgression and regression and thicknesses of the Early to Middle Paleozoic rock sequences may approach 1100 m (Poole et al., 1992). Roberts (1965) and Price (2002) note that carbonates are more prominent in Eastern Nevada and represent continental shelf environments, and that there is a greater ratio of siliciclastics that include shale, sandstone, and chert to the west representative of continental slope, continental rise and deep marine environments of deposition.

In the Late Devonian to Early Mississippian, it is believed that the continent collided with a small landmass or volcanic arc that resulted in the Antler orogeny (Price, 2002). This collision resulted in the thrusting and folding of lower and middle Paleozoic rocks from the west to the east and that the thrust interval principally consists of deeper water strata to include radiolarian chert, shale, sandstone and siltstone, greenstones and some ultra-mafic rocks over younger continental-shelf carbonates. This sequence is referred to as the Roberts Mountain allochthon and estimates of maximum displacement of the thrust range from 75 to 200 km (Miller et al., 1992; Poole et al., 1992). The approximate extent of the Antler Orogenic Belt is shown on Figure 5.

Erosion of the resulting uplifted Antler highlands resulted in the deposition of conglomerate, sandstone, siltstone and shale within the backarc basin area with

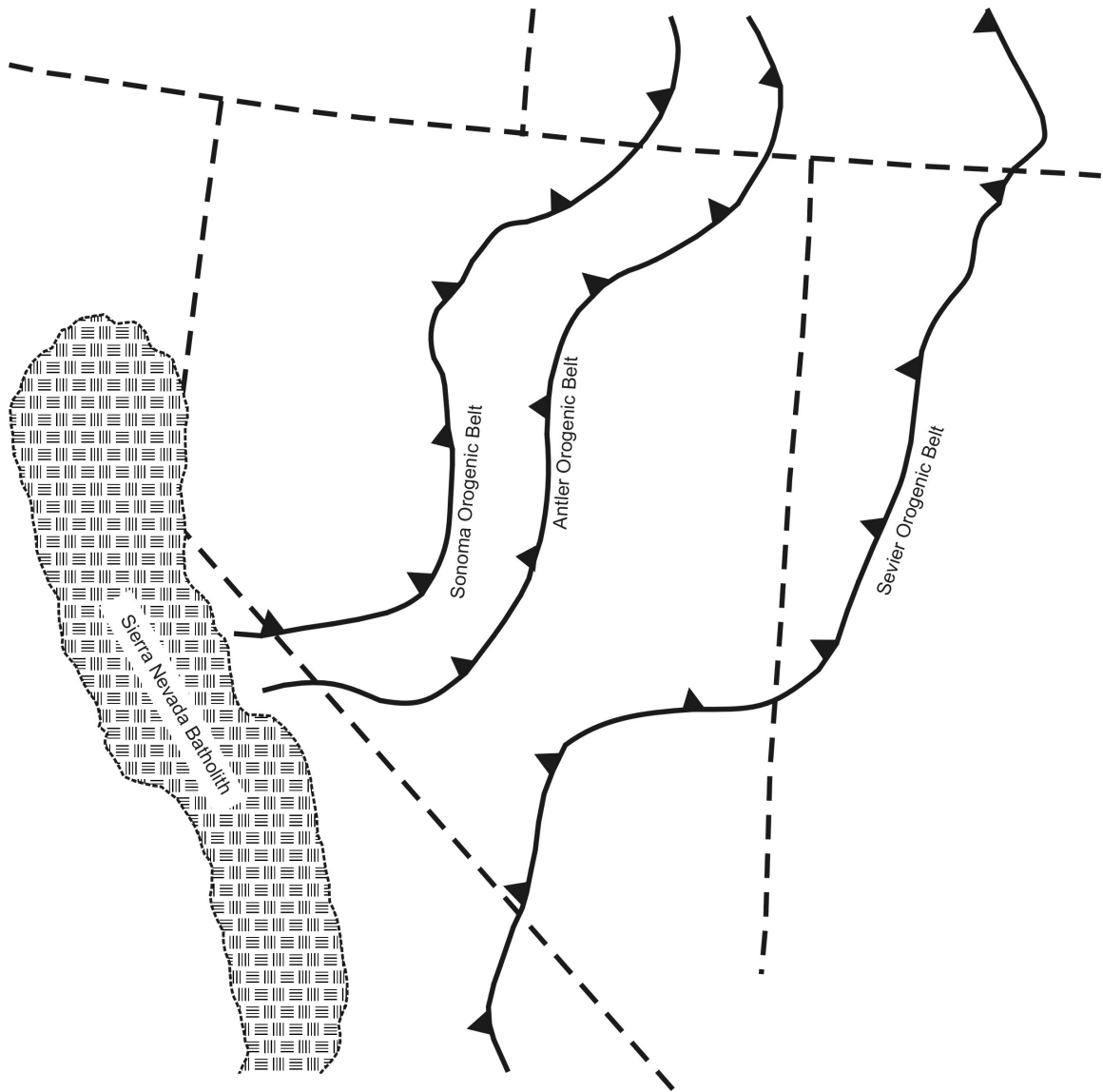


Figure 5. Approximate extent of orogenic belts (modified from Poole et al., 1992 and Saleeby and Busby-Spera, 1992).

carbonates continuing to be deposited in the east along the continental craton during the remainder of the Mississippian, Pennsylvanian and into the Early Permian (Miller et al., 1992). During the Late Permian and continuing into the Triassic, another collision and subduction occurred on the western margin resulting

in the Sonoma orogeny (Miller et al., 1992) the approximate extent of which is illustrated on Figure 5 . Thrusting and extensive volcanism again occurred in the western portion of the region with continued carbonate deposition in the east (Roberts, 1965; Price, 2002).

The thrusting from the Late Permian and Early Triassic from the Sonoma orogeny resulted in the emplacement of the Golconda allocthon sequence which is comprised of rocks from the latest Devonian to the Late Permian (Miller et al., 1992; Poole et al., 1992). During the later part of the Early Triassic and continuing into the Early Jurassic, igneous activity including explosive volcanic eruptions resulted in the deposition of thick ash-fall tuffs in the west along with continued deposition of sedimentary rocks presumably from the uplifted areas from the Sonoma orogenic event. Shallow marine carbonate rock deposition continued on the eastern side of the Great Basin (Price, 2002; Saleeby and Busby-Spera, 1992).

Beginning in the Middle Jurassic and continuing into the Cretaceous, more folding and thrusting occurred with the Nevadan and Sevier orogenic events. The approximate extent of the Sevier orogenic belt is shown on Figure 5. Subduction along the west coast of continent also resulted in the emplacement of granitic igneous intrusions (Price, 2002). As a result of the uplift that occurred with the Nevadan and Sevier orogenic events, there was significant erosion and little deposition resulting in an unconformity between the Mesozoic and Cenozoic rocks (Albers, 1965).

Extension of the Basin and Range began approximately 30 to 40 Ma. The extension combined with continued subduction to the west, and possible movement over the Yellowstone hotspot resulted in abundant volcanism and igneous activity (Price, 2002). Albers (1965) reports the earliest dated volcanic rocks at 39 Ma during the Early Oligocene. The extension also resulted in considerable block faulting with areas of higher relief separated by intervening basins and lakes. Deposition during the Paleogene and Neogene therefore consists principally of volcanics along with lacustrine and fluvial sedimentary rocks (Albers, 1965; Price, 2002).

During the Pleistocene ice ages, glaciers formed in the higher elevations with pluvial lakes occupying the lower elevations including Lake Lahontan. Quaternary deposits principally consist of unconsolidated alluvium (Albers, 1965).

Basin and Range Structure

Davis (1979) reports that the southwest and northwest boundaries of the Great Basin are defined by intraplate strike-slip faults that separate the region of extension from the terrains to the north and south that lack the general structure of the Basin and Range, i.e. elevated areas with high-angle normal faults and intervening basins. As noted in the previous section, there were at least five major tectonic events affecting the region: 1) rifting and continental divergence during the Late Precambrian; 2) the Antler orogeny and associated folding and thrust faulting during the Late Devonian to Early Mississippian as the result of collision with a small landmass or volcanic arc; 3) Late Permian to Early Triassic thrusting and

volcanism due to plate collision and subduction during the Sonoma orogeny; 4) additional folding and thrusting as the result of several episodes of plate collision and subduction from the Nevadan and Sevier orogenic events during the Middle Jurassic into the Cretaceous; and 5) extension and rifting and associated normal faulting and igneous activity during the Cenozoic. In summary, there are a series of thrust faulting episodes during the Paleozoic and Mesozoic followed by the extensional features and volcanism in the Cenozoic.

The present day physiography of the region generally consists of complex system of grabens or half-grabens and mountain horsts of tilted blocks with interspersed volcanic features including cinder cones (Stewart, 1998). The range front faults on the boundaries of the horsts are believed to flatten at mid-crustal levels (listric faults) and that extension below these depths may be occurring by ductile flow of crustal rocks (Davis, 1979). In addition to the range front faults, a series of parallel piedmont faults often occur towards the valleys and antithetic faults dipping the opposite direction may occur on the opposite side of the valleys. Figures 6 and 7 illustrate hypothetical cross-sections across the region.

The normal faults are terminated by either transfer zones or accommodation zones where strain is transferred to adjacent parallel fault systems. Faulds and Varga (1998) define transfer zones as discrete zones of strike-slip and oblique-slip faulting that parallel fault strike direction and that are perpendicular to extension. They define accommodation zones as belts of overlapping terminations that can

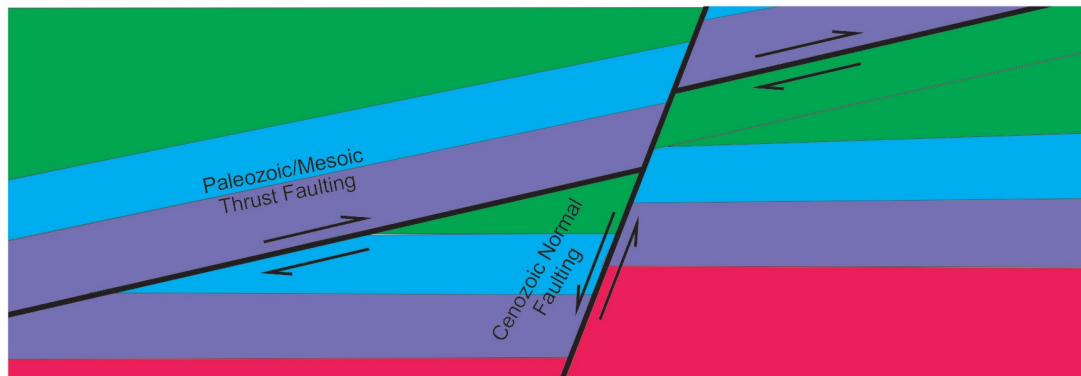


Figure 6. Generalized cross-section of typical Paleozoic/Mesozoic thrust faulting followed by Cenozoic normal faulting.



Figure 7. Hypothetical cross-section of typical Basin and Range listric normal faulting, fracturing, and magmatism (heavy lines) (modified from Eaton, 1979).

trend parallel , perpendicular, or oblique to the extension direction. Figure 8 presents simple conceptual diagrams of transfer zones and accommodation zones.

Geothermal Setting

As previously discussed, the Basin and Range is characterized by thin crust, low upper mantle seismic wave velocities, regionally high elevations, and high heat flow. High heat flow may result from the thin crust as well as from near-surface sources of heat such as magma chambers or hot, recently emplaced and solidified rock (Garside and Schilling, 1969). In addition to conduction of heat through the rock, water may act as a transport mechanism for the heat. Potential sources of this water include connate water, magmatic water, and meteoric water that circulates to depth and rises back to the surface. Repeated intrusions of the crust by magma and

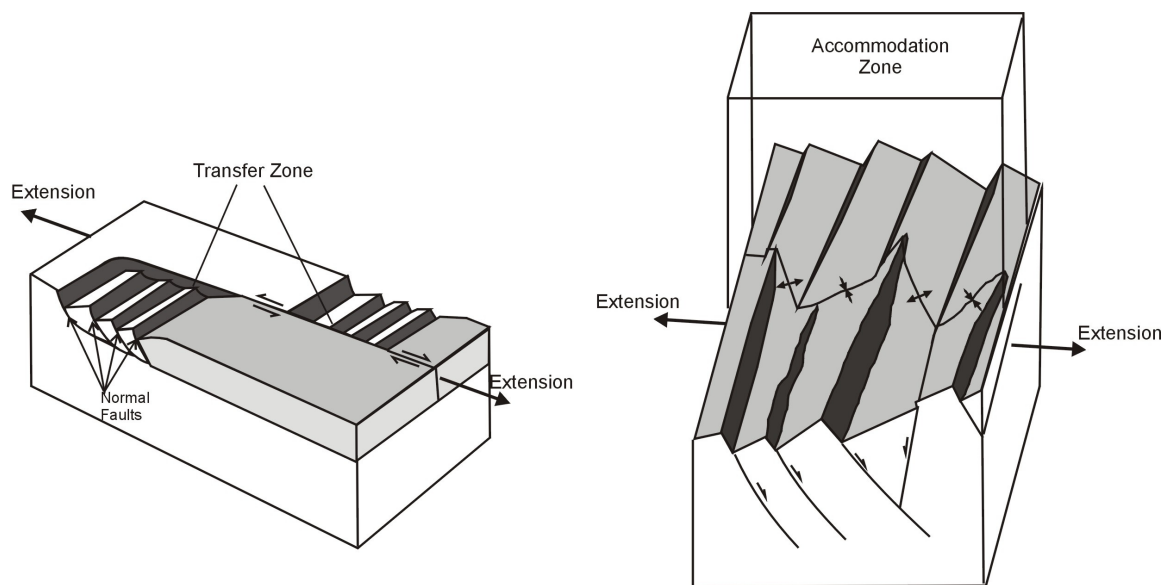


Figure 8. Illustrations of transfer zones and accommodation zones (modified from Faulds and Varga, 1998).

hydrothermal circulation has also resulted in the transportation and deposition of ore minerals during both compressional and extensional phases within the province (Eaton, 1979).

While there has been a significant amount of magmatic activity in the region during the Cenozoic, most is older than 10 Ma and would be cooled to temperatures that would not contribute significant heat to geothermal systems (Lachenbruch and Sass, 1978). It should be noted however, that Quaternary volcanics do occur scattered throughout the Basin and Range including a mapped outcrop along the edge of the Humboldt Range just north of the existing plant as shown on Figure 2.

Flynn and Buchanan (1990) note that the early hypotheses of geothermal recharge were that relatively recent precipitation that fell on nearby mountain highlands flows downward along faults and fractures to depths of three to five km, is heated, and returns to the surface. They present an alternative hypotheses that the geothermal fluids were recharged during the Pleistocene when there was greater precipitation.

Regardless of the age, the general conceptual model that has been developed for the region is that water flows downward along faults and returns to the surface along similar pathways. Richards and Blackwell (2002) and Blackwell et al. (2003) present three possible scenarios to account for the different geothermal and groundwater systems and features that are commonly found in the Basin and Range including fumaroles near range front faults, hot springs located further down in the

valleys, and areas with shallow warm outflow dependent on the groundwater piezometric surface and flow. These scenarios are illustrated in Figure 9.

Research Area

Lithology

The Rye Patch geothermal area is located in the Humboldt River Valley in Pershing County, Nevada. As previously mentioned, the study area is bounded by the Humboldt Range on the west and by the Rye Patch Reservoir on the east (Figure 2). Johnson (1977) presents a detailed discussion of the Geology of Pershing County. In the study area, the Humboldt Range is described as being a north-trending anticlinal structure with a complex network of faulting formed by the Nevadan orogeny during the Jurassic and Cretaceous periods (Johnson, 1977; Hastings, 1993)

The oldest exposed rocks consist of the Lower Triassic Koipata Group which consists of the Limerick Greenstone, the Rochester Rhyolite and the Weaver Formation. The Koipata Group is overlain by the Star Peak Group, also Triassic in age. The Star Peak Group consists of the principally carbonate rocks of the Prida and Natchez Pass Formations. Pelitic and fine-grained clastic rocks of the Upper Triassic Grass Valley Formation, part of the Auld Lang Syne Group, overlie the Star Peak Group. Burke and Silberling (1973) report that the Dun Glen Formation also of the Auld Lang Syne Group, is present at the southern end of the Humboldt Range.

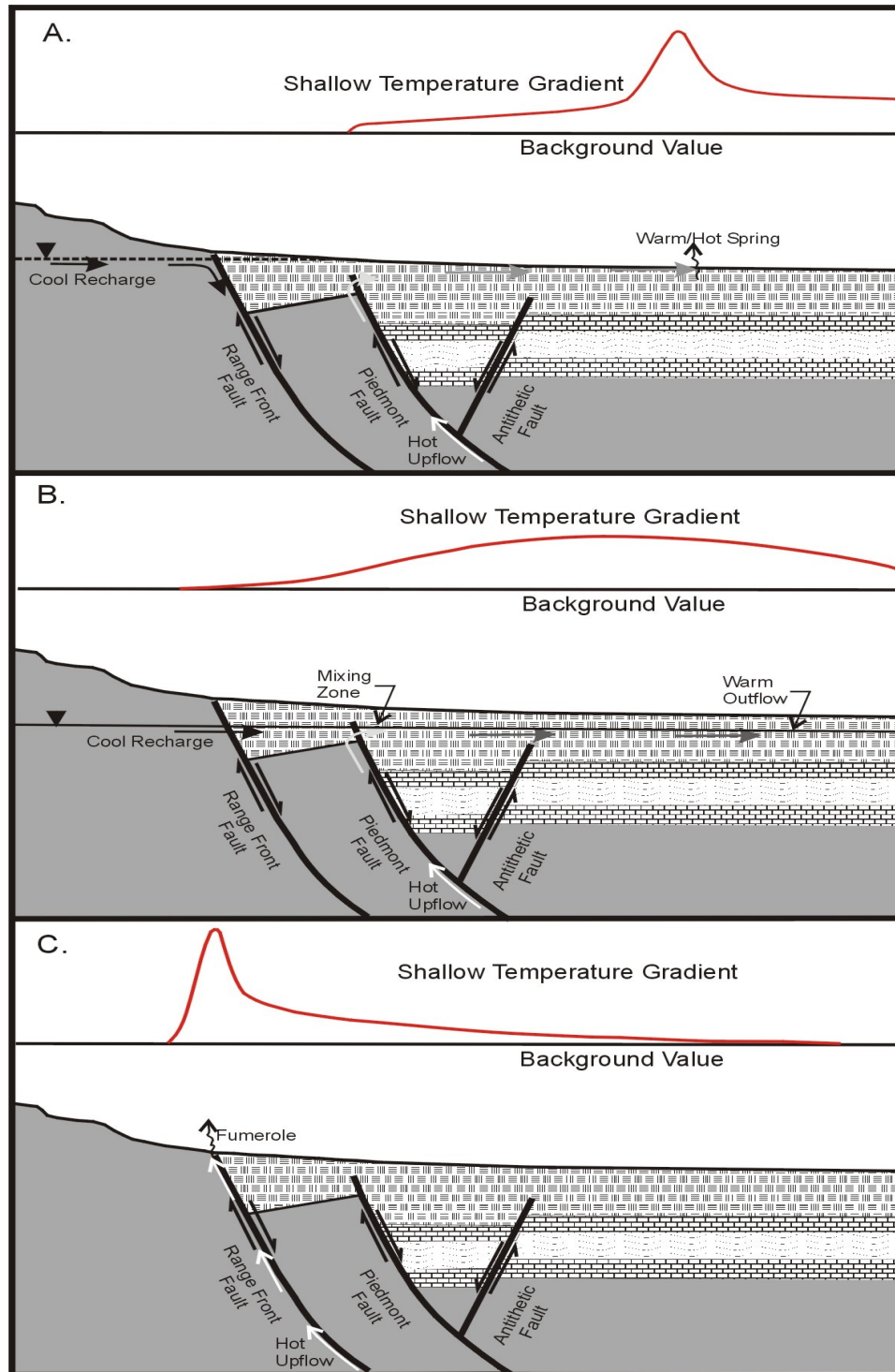


Figure 9. Three possible scenarios for shallow geothermal fluid movement in the Basin and Range. The hot fluids flowing along the faults interact differently with the water table, creating varied surface effects (modified from Richards and Blackwell, 2002).

On the western side of the Humboldt Range, the upper member of the Natchez Pass and the Grass Valley Formation are thrust over the Prida Formation along the Humboldt City thrust fault and the Grass Valley Formation has been locally metamorphosed to argillite, phyllite, slate and quartzite (Silberling and Wallace, 1969; Johnson, 1977).

Within the valley, the Grass Valley Formation is overlain by Paleogene and Neogene clays, shales, and volcanics. The Paleogene and Neogene deposits are followed by Quaternary clays, silts, sands and gravels with interbedded sinter deposits (Johnson, 1977; Michels, 2002). The deposits capping the valley floors and the along the mountain flanks consist of alluvium, flood-plain and playa lake deposits, and sand dunes. A generalized stratigraphic column is shown in Figure 10.

The Limerick Greenstone consists of altered andesitic flows and volcanoclastics (Hastings et al., 1993). Johnson (1977) describes the Rochester Rhyolite as a pale-colored altered felsite with lenses of coarse-grained tuffaceous sedimentary rocks that have been locally metamorphosed. It is believed to have been deposited in non-marine environments as an ash-flow tuff (Johnson, 1977). As much as five percent of the Rochester Rhyolite is comprised of poorly sorted tuffaceous mudstone to boulder breccia that is characterized by lenticular bedding (Johnson, 1977). The Weaver Formation is described by Hastings et al. (1993) as also consisting of rhyolitic tuffs, flows, and volcanoclastics.

Age	Group	Formation	Description
Quaternary	--	Unnamed	Clays, silts, sands and gravels with interbedded sinter deposits
Paleogene and Neogene	--	Unnamed	Volcanics, sands, gravels, clays, and shales with minor amounts of limestone
Unconformity			
Upper Triassic	Auld Lang Syne	Dun Glen	Limestone and dolomite with interbedded sandstone and argillite
		Grass Valley	Mudstone and fine-grained sandstone that is variably recrystallized to argillite, slates and quartzite
Middle Triassic	Star Peak	Natchez Pass	Limestone with volcanics and terrigenous clastics grading into massive carbonates
			Massive limestone with interfingers of mafic volcanics
		Prida	Upper Member - limestone and dolomite with thin interbeds of chert
			Middle Member - silt, shale and siltstone with interbedded carbonates
Lower member - siltstone, sandstone, and carbonates			
Unconformity			
Lower Triassic	Koipato	Weaver	Rhyolitic tuffs, flows and volcaniclastics
		Rochester	Altered felsite with tuffaceous sedimentary rocks
		Limerick	Altered andesitic flows and volcaniclastics

Figure 10. Generalized stratigraphic column of rocks exposed in the Humboldt Range.

The Prida Formation is divided into three members. In the Humboldt Range, the lower member is composed of a lithologically heterogeneous sequence of three units. The basal unit consists of detrital rocks, the middle unit consists of carbonate rocks, and the upper unit is composed of siltstone and sandstone (Johnson, 1977).

The middle member of the Prida Formation is relatively homogeneous and consists of thin-bedded silty shale and siltstone with lesser amounts of thin- to medium-bedded fossiliferous limestone. The upper member is composed of dark, thin- to medium-parted limestone and dolostone with thin beds of dark chert that interfinger with the lower part of the overlying Natchez Pass Formation (Johnson, 1977).

Johnson (1977) describes the Natchez Pass Formation as consisting of a massive deposit of carbonate rocks intermixed with andesitic lava flows and volcanic breccia. In the Humboldt Range, the Natchez Pass Formation is divided into two members. The lower member consists of massive limestone interfingered with mafic volcanic rocks that thin to the north (Silberling and Wallace, 1969). The upper member is described by Johnson (1977) as having a basal section of impure limestone and lesser amounts of volcanic and terrigenous clastic rocks that grade upward into massive carbonate rocks.

The Late Triassic Grass Valley Formation is described by Johnson (1977) as consisting of primarily of mudstone and fine-grained sandstone that is variably recrystallized to argillite, slates and quartzite. Thin, discrete beds of well-sorted sandstone are abundant in higher parts of the sections and show cross-stratification features that suggest beach, bar, and fluvial deposition. The argillite is composed of quartz, silt, chlorite, sericite, and muscovite (Johnson, 1977; Hastings, 1993). The Dun Glen Formation consists of thickly bedded limestone and dolomite with interbedded sandstone and argillite (Burke and Silberling, 1973). Sibbett (1981)

notes that, in general, the principally argillaceous and slaty Auld Lange Syne Group rocks have very low intergranular permeability and that they may not be competent enough to have significant fracture permeability.

As previously mentioned, Paleogene and Neogene deposits consist of volcanics, sands, gravels, silts, clays, and shales with minor amounts of limestone. Michels (2002) postulates that the Paleogene and Neogene siltstones and claystones above the Triassic rocks act as an impermeable cap that may be enhanced by sinter deposits. The upper valley fill consists of Quaternary alluvium along the flanks of the range and flood-plain deposits, playa lake deposits, and dune sand in the area of the Rye Patch Reservoir and along the Humboldt River with sinter deposits interspersed throughout. A mapped unit of Quaternary Basalt is located to northeast of the geothermal plant (Figure 2). Johnson (1977) describes the basalt flows as being highly vesicular, dark gray to black basalt, with phenocrysts of plagioclase, pyroxene, and olivine in an aphanitic ground mass. It is believed that local dikes, sills, and plugs of porphyritic basalt were feeders for these lava flows, and the basalts are considered to be related to Basin and Range normal faulting. Hastings et al. (1993) also note that intrusive dikes and plugs are present throughout the Triassic, Jurassic, and Cretaceous rocks of the Humboldt Range. These include granite, aplite, rhyolite, andesite, diorite, diabase, and mafic flows. Hastings et al. (1993) also report a quartz monzonite stock of late Cretaceous age as being located in the west central part of the Humboldt Range. Sanyal et al. (2006) postulate that the contact between the Mesozoic rocks and the overlying

sedimentary and volcanic rocks of Paleogene age may be an eroded land surface that resulted in karst features. In addition, well logs indicate that there is a sandstone and siltstone unit within the Natchez Pass Formation (basal section of the upper member) which may be 120 to 150 m thick in areas and that separates massive limestone units. It is believed that geothermal water is produced from both the interface between the Mesozoic and Cenozoic rocks and the Natchez Pass clastic unit and that fractures and faulting controls the flow patterns (Feighner et al., 1999; Gritto et al., 2003; Sanyal et al., 2006).

The majority of wells and bore holes in the area have apparently been terminated within or above the Natchez Pass Formation with only a few possibly reaching the upper member of the Prida Formation. Logs of several of the wells near the plant prepared by Presco Energy are presented in Appendix A.

Structure

Hastings et al. (1993) and Sanyal et al. (2006) report that the Mesozoic rocks dip to the west-northwest at an angle of between 20 to 40 degrees. The overlying sedimentary and volcanic rocks of Paleogene, Neogene and Quaternary age are nearly horizontal and the contact between the Mesozoic and Cenozoic rocks is unconformable with the dip of the unconformity approximately 30 degrees to the northwest (Sanyal et al., 2006).

The major Basin and Range (Cenozoic) faulting generally trends northward and bounds the mountain ranges with parallel piedmont faults occurring in the alluvial valleys and possible antithetic faults on the opposite side of the valley and

this general pattern is observed in the study area. These north-trending fault systems cut and are cut by shorter east-west trending transfer faults or accommodation zones (Faulds and Varga, 1998). The Midas Lineament, a left lateral strike-slip zone, truncates the Humboldt Range on the north (Rowan and Wetlauger, 1981; Hastings et al., 1993) and another east-west trending transfer fault or accommodation zone offsets the West Humboldt Range and the Humboldt Range to the south (Waibel et al., 2003).

The normal faulting has been intermittent from about 16 Ma to the present with maximum displacement that may be on the order of several thousand meters (Johnson, 1977). Ehni (2001) states that at Rye Patch, geothermal fluids may be fed to cavernous limestone beds (presumably at the Mesozoic/Cenozoic contact noted above) by high angle normal faults. It should also be noted that evidence suggests that the geothermal fluid circulation may be enhanced in areas where fault systems merge (Smith, 2003).

Thrust faults within the Humboldt Range include the Golden Stairs Thrust and the Humboldt City Thrust along which the upper member of the Natchez Pass and the Grass Valley Formation are thrust over the Prida Formation. These thrust faults are believed to have been formed during the Nevadan orogeny (Johnson, 1977). Known normal faults include the Range Front Fault along the base of the Humboldt Range and the Rye Patch Fault, a piedmont fault located to the west of the Range Front Fault and near the existing plant. Seismic sections, LiDAR, and aeromagnetism suggest that there may be other parallel faults to the west of the Rye

Patch Fault and dip reversals identified in the most recent seismic survey may indicate antithetic faults further to the west (Ellis, 2011). A hypothetical structural cross-section is presented as Figure 11.

Geothermal Setting

The Rye Patch KGRA includes what has been referred to as the Humboldt House geothermal anomaly to the north and the more southerly Rye Patch geothermal anomaly located near the existing plant (Figure 2). Based on the numerous studies, explorations, wells and other borings, and observations at the site, it appears that all three scenarios of Richards and Blackwell (2002) as presented diagrammatically in Figure 9 may be operating in the KRGAs. Specifically, the sinter deposits located in the Humboldt House area are indications of hot springs and fumaroles (MacKnight et al., 2005) indicative of cases a) and possibly c) of that figure. MacKnight et al. (2005) also speculate that as the sinter deposits are younger than the Pleistocene Lake Lahontan sediments, that they must be fairly recent (< 10,000 y) and the linear nature observed by LiDAR suggest that they were structurally controlled by piedmont or antithetic faults in that area. The shallow, laterally-flowing outflow discharge plumes have been identified by temperature measurements in wells and exploration borings, shallow temperature measurements and drill holes and mining operations associated with the Florida Canyon mine (Waibel, et al., 2003) and are indicative of scenario b) of Figure 9. In addition, the fumarole reported by Croffutt in 1872, if it was close to the Humboldt Range as speculated, is also an indication of scenario c).

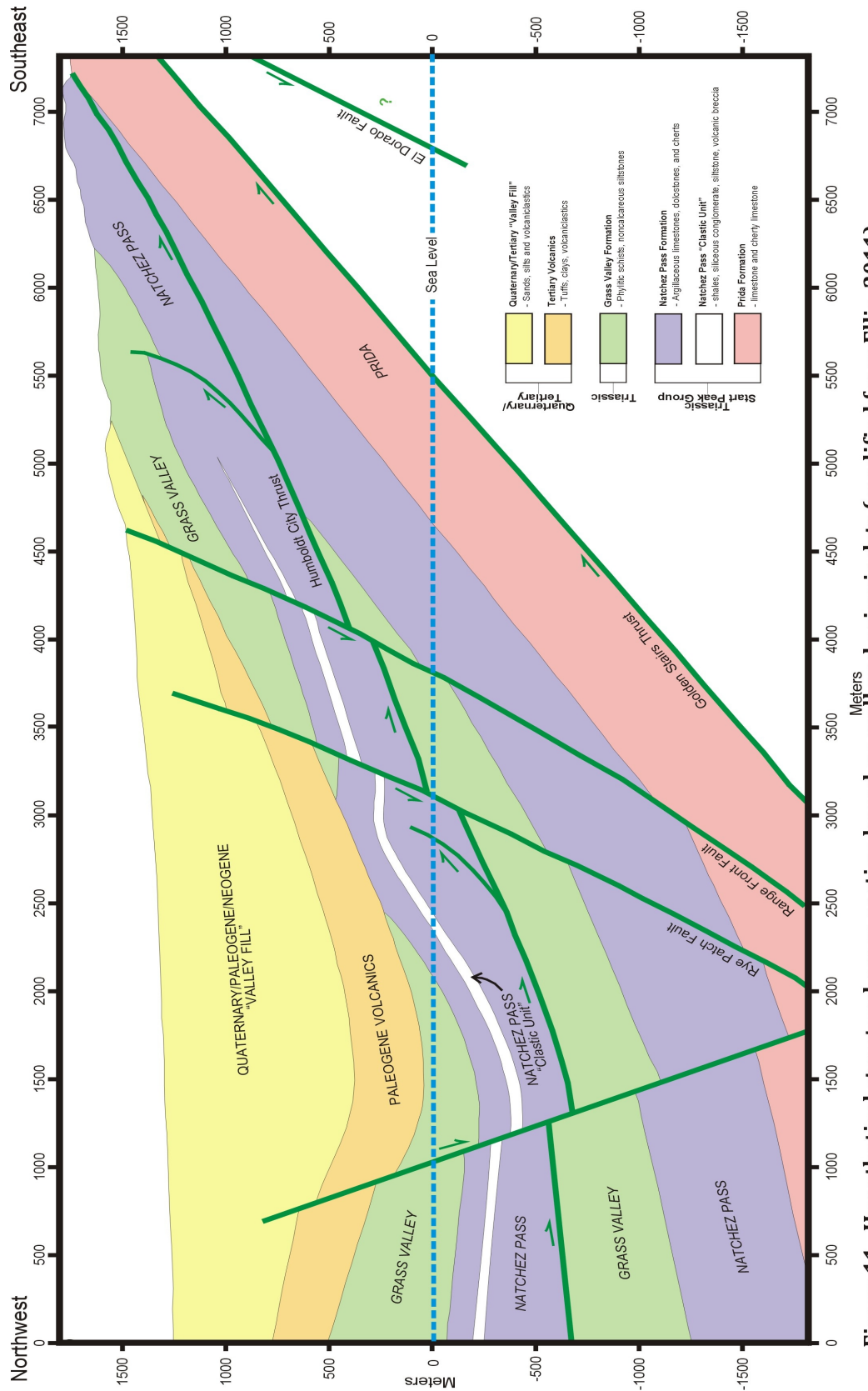


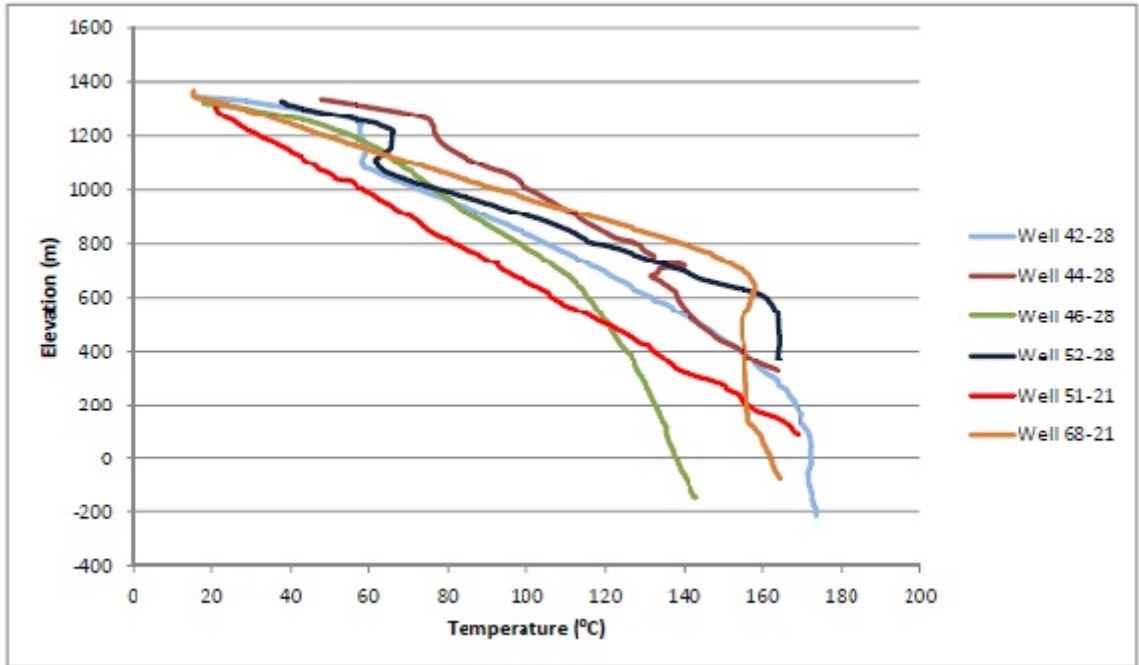
Figure 11. Hypothetical structural cross-section based on well and seismic data (modified from Ellis, 2011).

Ellis (2011) reports that on the basis of measured geothermal gradients and temperature profiles of wells and borings within the KGRA, it is believed that there are three principle geothermal zones:

- 1) a shallow, low enthalpy outflow zone located in the valley fill with temperatures on the order of 65°C to 95°C;
- 2) a medium-enthalpy zone located at the interface between Paleogene and Triassic rocks at depths of approximately 550 m to 640 m with temperatures ranging from around 150°C to 175°C; and
- 3) a higher-enthalpy zone within the clastic unit of the Natchez Pass formation at depths on the order of 1040 m with estimated temperatures above 200°C .

Figure 12 shows temperature vs. depth profiles of a number of wells in the vicinity of the existing plant. Temperature gradients calculated for these profiles are approximately 120°C·km⁻¹ to depths of approximately 750 m, and then decreasing to approximately 30 to 35°C·km⁻¹ presumably where there is a transition to Triassic carbonates.

Michels (2002) presents support for these zones by noting that the static temperature profile of well 72-28 indicates that there are various conductive and convective zones above and below the aforementioned impermeable layer. He also notes that the high wellhead pressures in some of the wells are an indication of the separation of the low- and medium-enthalpy wells by his postulated impermeable cap.



Well	Easting	Northing	Elevation	Pgv	Trgv	Trnu	Clastic	Trnl	Prida
42-28	392155	4486835	1357	640		594	335	138	-137 ?
44-28	392180	4486555	1352	736		703	392		
46-28	392070	4486070	1347	884		709	451	381	-30 ?
51-21	392340	4488700	1337	631	190	152			
52-28	392380	4486820	1361			671	488	366	
68-21	392600	4487340	1375	800		564			61 ?
Qoa	Quaternary and older alluvium								
Pgv	Paleogene volcanics								
Trgv	Triassic - Grass Valley - shales, argillites								
Trnu	Triassic - Natchez Pass upper member - carbonate								
Clastic	Triassic - Natchez Pass clastic unit (siltstone and sandstone)								
Trnl	Triassic - Natchez Pass lower member - carbonate								
Trpu	Triassic - Prida upper member - carbonate with chert								

Figure 12. Temperature gradients and formation tops from a number of wells near the existing geothermal plant.

On the basis of water chemistry and geothermometers, Michels (2002) also arrived at the conclusion that all of the wells had a common heat source with a temperature in excess of 270°C and estimated that drilling depths of between 2100 and 2440 m would be required to reach these temperatures. The Nevada Bureau of Mines and Geology (2012) lists resource temperatures from several wells in the KGRA as ranging from 209°C to 247°C using the calcium/sodium/potassium geothermometer developed by Fournier (1981) but much lower temperatures using the quartz geothermometer ranging from 166°C to 226°C. However, silica is sensitive to changes in pH and also requires careful sampling and preservation (Fournier, 1981, Reed and Mariner, 2007). Michels (2002) also notes that the water from the wells was depleted in silica. Desormier (1979) also reported both silica and Ca-Na-K resource temperatures ranging from 232°C to 254°C. MacKnight et al. (2005) estimated water temperatures in excess of 200°C were necessary for the deposition of opal that was identified in their hyperspectral analysis. These results lend support for the high enthalpy region and, as noted above, Ellis (2011) estimates that the 200°C temperature would be achieved at depths of around 1050 m.

In summary, the evidence suggests that all three scenarios illustrated in Figure 9 may be occurring at the site. It is likely that recharge is occurring or did occur along the Range Front Fault, circulates to depth and rises along other faults or conduits, e.g. the Rye Patch Fault, which feeds the three zones. In addition, the postulated three enthalpy zones of Ellis (2011) are supported by the evidence although complicated by the heterogeneous nature of the geology and the tendency

of the deposition of sinter to reduce permeability and seal flow paths. It is probable that the flow and “reservoirs” or “aquifers” are highly compartmentalized. In general, there is the upper outflow zone where mixing of groundwater and upwelling geothermal fluid occurs and which acts as unconfined aquifer or reservoir, the middle zone which may be located at the interface between Mesozoic and Cenozoic strata and whose relatively high pressures indicates a confined reservoir, and the deeper and hotter zone that may be within the clastic unit of the Natchez Pass Formation. However, based on the geochemical and mineralogical and temperature gradients, water must be circulating to greater depths to achieve the estimated reservoir temperatures of $>270^{\circ}\text{C}$.

The location of upwelling appears to be structurally controlled and probably occurs along faults that have been recently seismically active although over time these flow paths are eventually restricted or sealed by mineral deposition. Production and permeability appear to vary widely within short distances and the mineral deposition is also likely to affect flow.

CHAPTER IV - METHODOLOGY AND RESULTS

Introduction

In 2008, Dr. William Gosnold of the University of North Dakota was requested by Presco Energy, LLC to conduct a gravity survey of the area. The original gravity survey was performed during the summer of 2008 and encompassed an area of approximately 78 km² within the boundary of the Rye Patch KGRA along with parts of 8 sections directly to the west and 8 sections directly to the east. The survey area specifically included Sections 26-36 of T32N, R33E, and Sections 1-23, and 26-35 of T31N, R33E. The survey consisted of occupying a total of 203 stations that were spaced at intervals of approximately 400 m along nine east-west lines to the west of the Humboldt range where terrain and access permitted, and along two north-south lines that were parallel to Interstate 80 and the adjacent railroad line. In addition, six four-wheel drive accessible trails that extended into the Humboldt range were used to obtain additional gravity readings to supplement the east-west profiles, and several readings were taken west of the Rye Patch Reservoir. The station locations of the 2008 survey are shown on Figure 13.

In 2010, I was requested to assist in processing and evaluating the data from the initial survey. Upon producing a simple Bouguer anomaly map, it was evident that the anomaly patterns were coincident with the elevation. For this reason,

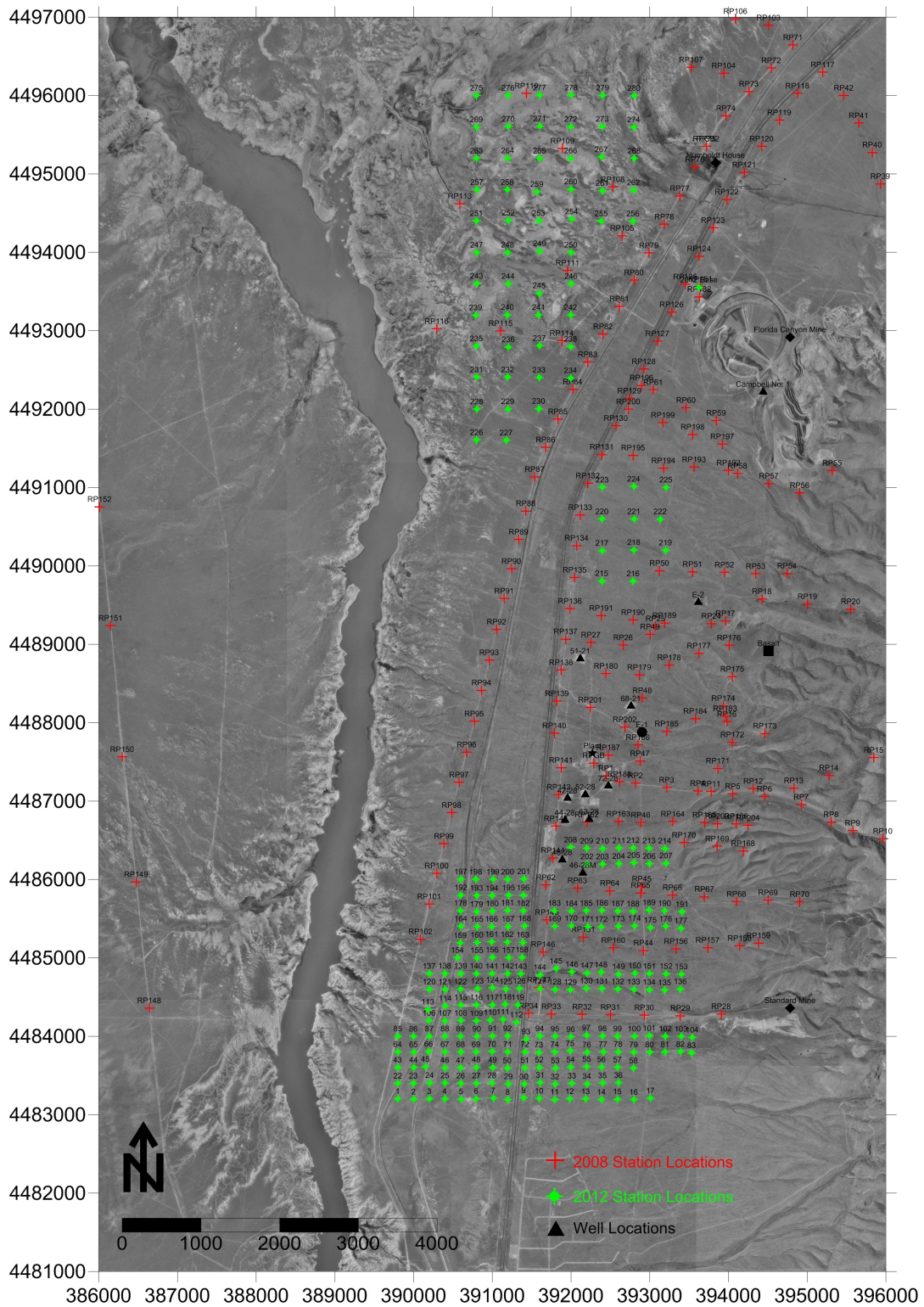


Figure 13. Station locations from the 2008 and 2012 gravity surveys.

terrain corrections were performed in an effort to reduce the topographic influence on the observed gravity readings. While the magnitudes of the anomalies were diminished after applying the terrain corrections, the strong regional influence was still apparent. For this reason, filtering methods were employed to remove the regional trends.

The results of the filtering and comparison with the aeromagnetic survey conducted by Presco Energy in 2008 indicated that the location and trend of major fault systems can be identified after implementation of filtering methods. Dip angles can be inferred by the anomaly contour gradients. However, the initial study was not extensive enough to delineate all features that are critical to the understanding of the geothermal field. For example, lengths of the features were difficult to interpret as the wavelength filtering tends to truncate features in accordance with the bandpass window and several areas did not have sufficient data points to produce contours with any degree of confidence.

Therefore, this study was proposed to augment the existing data by obtaining additional gravity measurements in areas with relatively low sampling density and to expand the study area in an effort to identify potential new geothermal targets within the basin. Specific areas of interest included the area around the Humboldt House in the northern portion of the KGRA and south of the existing plant extending beyond the areas previously sampled. In addition, I decided to obtain ground-based magnetic readings at the new stations to provide additional information. The field effort was conducted in May, 2012.

Station Locations - Global Positioning System

Prior to mobilizing to the field, potential station locations were determined by establishing a grid system. In the area with the conspicuous anomaly in the southern portion of the study area the grid was established at a spacing of 200 m to provide greater resolution. The southern Rye Patch anomaly area is also where the binary geothermal power plant is located and where the production wells have been completed. In the area of the Humboldt House, the principle goal was to establish if the anomalies and linear trends identified by the aeromagnetic and LiDAR surveys could be detected by gravity. A lower resolution grid spacing of 400 m was established in this locale and the area investigated was expanded from the survey performed in 2008 by Gosnold. Additional data points were also added in the central part of the study area to fill in data gaps from the 2008 survey. A total of 280 additional stations were planned, however due to the objections of adjacent land owners, a number of planned locations were eliminated and, including the base station, 264 stations were occupied for the 2012 survey. The locations are also shown on Figure 13.

After the grid system had been established using UTM coordinates, the coordinates were converted into latitude and longitude and entered into a handheld Global Positioning System (GPS) instrument. Once in the field, the handheld unit was used to find the approximate locations of the grid nodes. After the approximate locations had been found using the handheld unit, the more robust Trimble® 5700 geodetic receiver was deployed to acquire location to the desired level of accuracy.

It was desired to have an accuracy of 0.03 mGal to obtain results that could be confidently rounded to the nearest 0.1 mGal. To obtain this level of accuracy, vertical and horizontal stationing accurate to within 9 cm and 37.5 m respectively, were required.

The Trimble® 5700 system was used in the “fast-static” mode. In most cases, the system was able to track seven to ten satellites and observation times were typically on the order of eight minutes. Exceptions were points 195 and 240 where only six satellites were observed. The GPS site location data was referenced to the National Geodetic Survey Continuously Operating Reference Station designated TUNG that is located at 40° 24' 11.50757” latitude and -118° 15' 26.96344” longitude. In addition, a base station was established in the parking lot of the Florida Canyon Mine for added control. Post-processing was performed using the Trimble® Business Center software version 2.70 (2012). The post-processing resulted in vertical precision within +/- 6 cm with the exception of stations 24 (6.3 cm), 93 (7.5 cm), 111 (8.4 cm), and 195 (6.0 cm). Horizontal precision for all stations was within +/- 6 cm. Therefore, the data quality objectives for stationing were obtained for all points. The baseline processing report is included as Appendix B.

Gravity

The gravity measurements were obtained with a LaCoste and Romberg Model G gravity meter. The meter has a resolution of 0.01 mGal and a range of 800 mGal. As mentioned above, 203 measurements were obtained in the 2008 survey

and 264 were obtained in the 2012 survey. Prior to the start of the 2012 field survey, a reading was obtained at the International Geodetic System Network (IGSN71) absolute base station designated WINCH at the Winnemucca Court House. This station has an absolute observed gravity of 979,826.01 mGals. We then drove to the project site and established the base station at the Florida Canyon Mine and obtained a reading and thus were able to establish an absolute value for that station which allowed for the tie-in for the remaining stations in the 2012 survey to the IGSN71. Ideally, a loop would have been performed where measurements were obtained at the reference station and the Florida Canyon base station multiple times to account for tides and instrument drift, however the distance between the two stations (~ 65 km) made this impractical. Instead, tide corrections were made using MEGSYSTEMS Ltd. tide correction utility (tide tables) available at: www.megsystems.ca/webapps/tidecorr/tidecorr.aspx which uses the algorithm developed by Longman (1959).

The Florida Canyon base station was occupied at the beginning and end of each day to identify major tares that may have occurred as the result of instrument wear or inadvertent mishandling of the meter and to tie-in the absolute values for each of the subsequent temporary base stations which were established at locations near the stations that were to be occupied each day. Generally, the temporary base stations were established either near the center of the stations to be measured that day or at easily accessible locations such as near roadways.

The survey was conducted in a loop manner whereby a reading would be obtained at the temporary base station followed by readings at a number of stations and then a return to the base station. In almost all cases this was done within three hours although there several times where intermediate stations were re-occupied as we were too far from the temporary base station to make a return within a reasonable time. This looping procedure was performed to correct for tides and instrument drift. Each day was completed by taking another reading at the Florida Canyon base station.

After collection, the data was processed in accordance with the new standards for reducing gravity data as presented by Hinze et al. (2005). It should be noted that due to a lack of processing software, all corrections and data reduction was performed using a spreadsheet. This was greatly facilitated by the spreadsheet formulas published by Holom and Oldow (2007). Several steps were required prior to data reduction per Hinze et al. (2005). First, the raw data needed to be adjusted by means of interpolation using the calibration tables that were provided by the manufacturer for the gravity meter that was used. Once this was accomplished, corrections for tidal and instrument drift were performed per standard methodology (Telford et al., 1976; Robinson and Coruh, 1988). The data was then referenced to the IGSN71 absolute values discussed above. This resulted in what may be referred to as the “observed gravity” and the remainder of data reduction operations were then performed.

The normal (or theoretical) gravity was calculated using the 1980 Geodetic Reference System (GRS80 or Somigliana) ellipsoid:

$$g_T = \frac{g_e(1 + k \sin^2 \varphi)}{(1 - e^2 \sin^2 \varphi)^{1/2}}$$

where: g_T = theoretical gravity

g_e = normal gravity at the equator = 978032.67715 mGal

k = derived constant = 0.0019318513538639

e^2 = first numerical eccentricity = 0.00669437999013

φ = latitude

Per Hinze et al. (2005) a correction for the mass of Earth's atmosphere is required as it is included with the mass of Earth in the 1980 International Gravity Formula. Hinze et al. (2005) provide a correction based on an expression derived by Ecker and Mittermayer (1969, as cited by Hinze et al., 2005):

$$\delta g_{atm} = 0.874 - 9.9 \times 10^{-5} h + 3.56 \times 10^{-9} h^2$$

where: δg_{atm} = gravity effect of atmosphere (mGal)

h = height of station (m)

While this correction had a significant effect on the absolute values, it had very little influence on the relative values as the correction ranged from between 0.74 to 0.76 mGal for all stations.

Hinze et al. (2005) provide two methods for the height or free-air correction. The conventional method uses a first-order approximation where $\delta g_{FA} = 0.3086 h$

where h is in meters. The other method uses an second-order equation based on the GRS80 ellipsoid and Hinze et al. (2005) provide the following formula:

$$\delta g_{FA} = -(0.3087691 - 0.0004398 \sin^2 \varphi)h + 7.2125E^{-8}h^2$$

where: δg_{FA} = height (free-air) correction (mGal)

φ = latitude (degrees)

h = height of station above datum (m)

A comparison of the methods indicates that the difference between the first and second methods is relatively insignificant with values that are within 0.14 mGals. While this difference may be of note for absolute values, it was generally uniform and has little to no effect on the resulting anomaly patterns. However, for the purposes of this study, the second-order equation was used.

The attraction of the mass of material between the station and the vertical datum is accounted for by the Bouguer correction. The standard correction assumes that this mass can be represented by an infinite horizontal slab:

$$\delta g_{BC} = 2\pi G\sigma h = 4.193E^{-5}\sigma h$$

where: δg_{BC} = Bouguer correction using infinite slab (mGal)

G = gravitational constant = 6.673×10^{-11} ($m^3/kg/s^2$)

σ = density of slab (kg/m^3)

h = height of station(m)

However, LaFehr (1991) developed a revised procedure, the Bullard B correction, that accounts for the effect of Earth's curvature and that is based on the original work done by Bullard (1936, as cited by LaFehr). Instead of assuming a horizontal slab, a spherical cap with a surface radius of 166.7 km is used and the resulting equation is:

$$\delta g_{sc} = 2\pi G\sigma(\mu h - \lambda R)$$

where: δg_{sc} = Bouguer correction using a spherical cap

G , σ , and h are as before

μ and λ are dimensionless coefficients as defined by LaFehr (1991)

R = radius of the earth at the station (mean earth radius plus h)

Bouguer corrections were calculated by both methods for comparison and differences were typically on the order of 1.5 to 2 mGal. Again, these differences would be important for absolute gravity values but differences were uniform on a relative basis. For this project, the Bullard B correction was used. Making the above corrections results in the simple Bouguer anomaly which can be summarized as:

$$\delta_B = g_{obs} - (\delta g_n - \delta g_{atm}) + \delta g_{FA} - \delta g_{SC}$$

Processing software had been used to reduce the 2008 data. The software used the GRS67 ellipsoid model for the theoretical gravity calculations, did not include the atmospheric correction, used the first-order equation for calculating the free-air correction, and used the infinite slab equation for the Bouguer correction. Therefore, to make the data from 2008 and 2012 comparable, the tide and drift

corrected observed gravity values were used and the remaining corrections were performed in the same manner as the 2012 data. In addition, slight adjustments were required to tie the data from the two surveys together. The 2008 survey had been undertaken as a local survey and was not tied into absolute values. Anomalies were calculated by subtracting the base station from the simple Bouguer values. Therefore, as there was no common “datum”, the two surveys should have been tied together by re-occupying the exact locations of several of the stations from the first survey during the second survey. As this was not done, it was necessary to develop a methodology that would make the data from the two surveys comparable and to arrive at a common datum.

The first step was to calculate the anomalies for both sets of data without using an absolute or reference value in the observed gravity term but rather just using the calibrated and tide and drift corrected values from both data sets and then performing the remainder of the corrections. Once this was accomplished, the data were gridded using the Kriging algorithm in the Surfer[®] software package (v. 9, Golden Software, 2010). It was very evident that the data sets would need to be adjusted as the contours were not smooth and there were rather abrupt changes where locations from the 2008 survey were near the 2012 locations. As this pattern was observed across the study area, it was deemed that it was an issue with data comparability and not due to local anomalies. Therefore, to arrive at a correction scheme, I first identified two areas where a station from the first survey was in close proximity to a station from the second survey. The two areas selected had stations

that were 16 and 19 m apart. The gravity gradient in the vicinity of these data points from the 2008 survey was calculated which was then multiplied by the distance between the two stations to arrive at a predicted value at the location of the 2012 station. This predicted value was compared with the value of the 2012 data and the difference was used as the correction factor to be applied to all stations. The correction factor was slightly different between the two locations, so a weighted average was calculated based on the distance between the 2008 and 2012 data points at both locations. After this value had been determined, it was applied to all of the 2008 data and the combined set was again re-gridded. There were still small jogs in the contour lines between 2008 and 2012 stations so small adjustments to the anomaly values were made on a trial and error basis until the contour lines between 2008 and 2012 data sets were nearly smooth and continuous. Ultimately, the correction factor employed was -0.25 mGals to the 2008 data set. While this adjustment may appear excessively large, the following quotation was taken from a LaCoste and Romberg data sheet posted on EDCON-PRJ, Inc. website and available at: <http://edcon-prj.com/Services/documents/gmeter.pdf>.

“Gravity meter drift for a new meter is less than 1 mGal per month. As a LaCoste & Romberg meter ages, the drift often improves to rates of less than 0.5 mGal per month. Once initial expansion takes place, the sensor does not radically change its characteristics with time, in fact they become more stable.”

Both surveys utilized the same gravity meter (G-774 manufactured in 1984) and, as there was a difference of 46 months between surveys, the difference does not seem unreasonable based on the above. Once it was applied, the “absolute” value was added back into both data sets, the corrections made and a combined simple Bouguer anomaly map was produced as shown on Figure 14. A reduction density of 2.67 g/cm^3 was used as is typically used in similar surveys. Both Nettleton’s (1971) method and Parasnis’ (1979) method were attempted in an effort to determine a site-specific reduction density, however both resulted in unrealistic values on the order of 3.2 g/cm^3 . It is apparent that, while both methods can reduce or remove the influence of topography on determination of a reduction density, they do not take into account scenarios where less dense material is located in the valley’s (alluvium) with greater density material near the surface or outcropping in the higher elevations.

Upon examination, it was apparent that there was a strong correlation between the simple Bouguer map and the topography as shown on the shaded relief image underlying the anomaly map on Figure 14 and as presented as Figure 15. For this reason, terrain corrections were performed in an effort to reduce the topographic influence on the observed gravity readings. Terrain corrections were initially performed utilizing the computer program InnerTC (Cogbill, 1990) which calculates terrain corrections by essentially using the methodology developed by Hammer (1939). The program calculates mean elevations from Digital Elevation

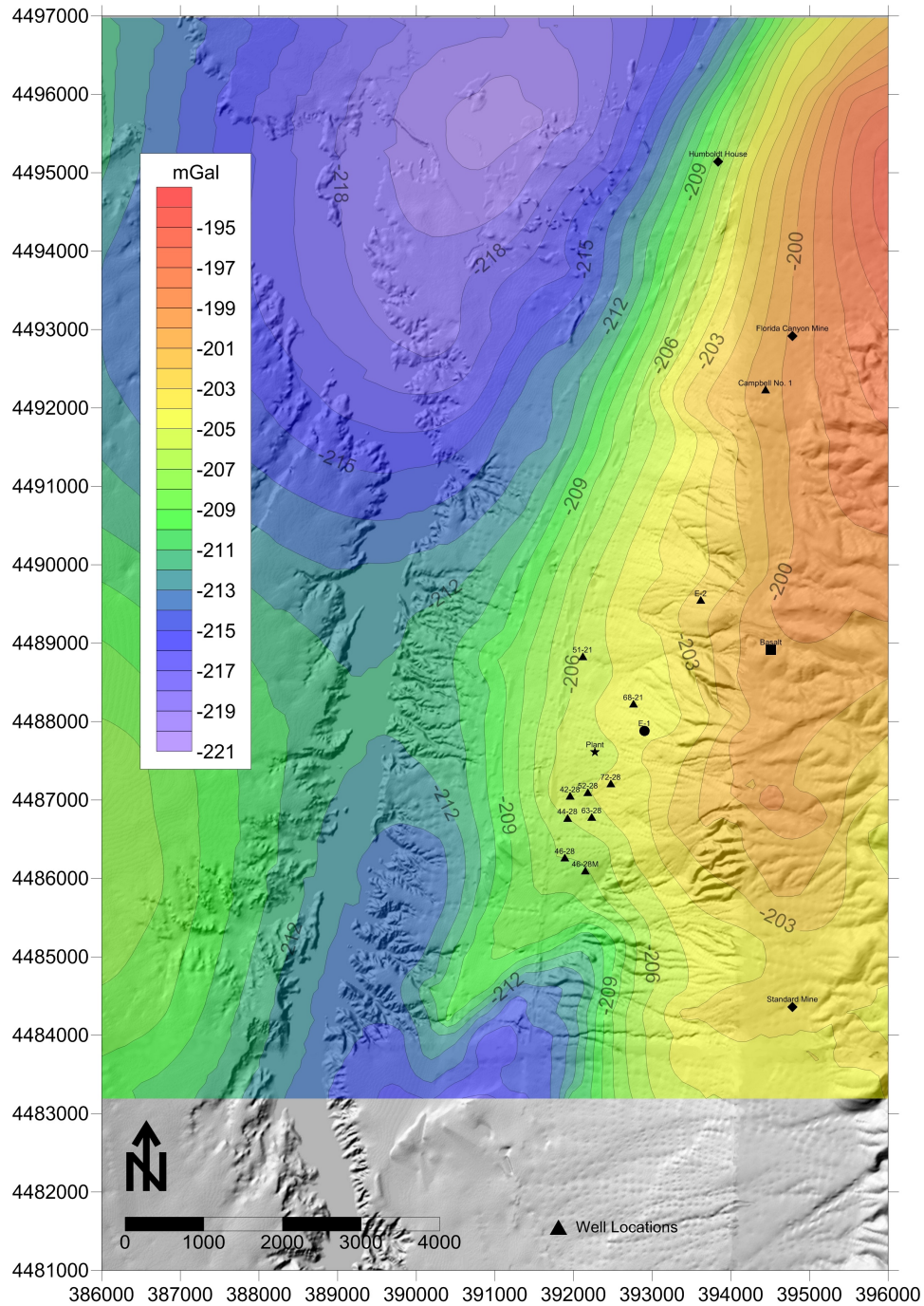


Figure 14. Simple Bouguer anomaly map. Note that the high anomaly values correspond with the higher elevations of the Humboldt Range per the underlying shaded relief map of the DEM and the lows with the lower elevations in the valley.

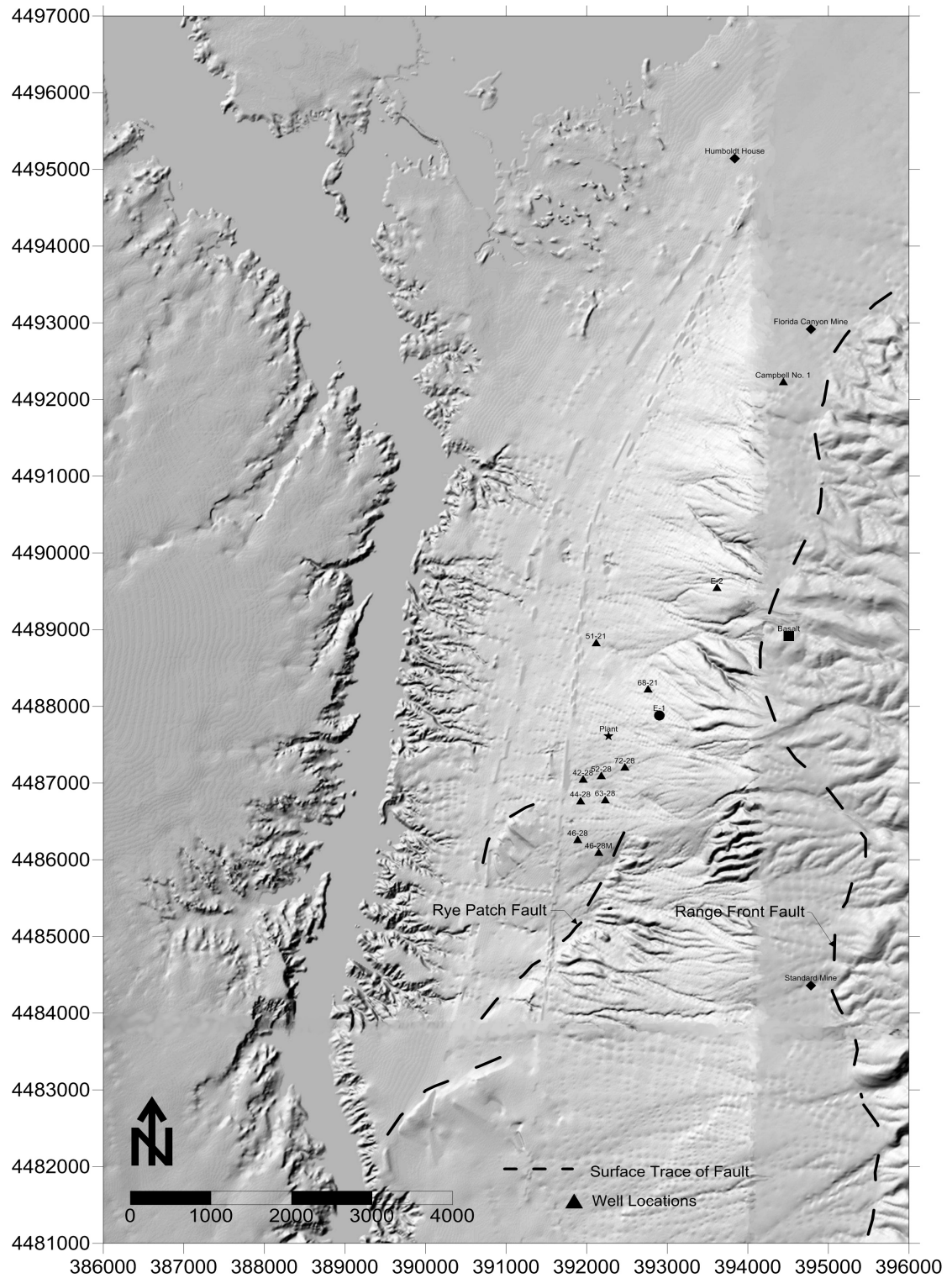


Figure 15. Shaded relief map of the digital elevation model with surface fault traces.

Models (DEMs) available from the USGS. For the InnerTC corrections, 7.5 minute DEMs with 10 meter resolution were used. The sensitivity of the terrain corrections to variations in the Hammer method circle radii was evaluated. This was performed by selecting an initial outer circle radius of two km and sequentially increasing the radius by one km at a time and re-running the InnerTC program. The results indicated that the terrain corrections for each station continued to increase even at a radius of 10 km. Hand calculations using the Hammer (1939) method at two selected locations showed that using the InnerTC values alone at the 10 km distance would underestimate the terrain correction and that the radius should be increased. Based on the recommendations presented in Nowell (1999) and Plouff (1966), the maximum radial distance was extended to 167 km (100 miles). However, increasing the radius to such a distance using the InnerTC program would have required the use of numerous additional 7.5 minute quadrangles. It was also felt that increasing the radii to such distances would have greatly increased the zone areas used in the Hammer method and therefore would result in a decrease in the desired resolution. For these reasons, the OuterTC program developed by Plouff (1966) and Cogbill (1990) was also used.

The OuterTC program is again based on the Hammer method and the corrections are also calculated using data from DEMs although at a much coarser grid. Specifically, 1-degree DEMs were used and the maximum circle radii were increased to a distance of 167 km. The results from the InnerTC program were utilized to a distance of 2.5 km, and the terrain corrections beyond that distance to

the 167 km maximum were calculated by the OuterTC program. The results ranged from a minimum terrain correction of 0.09 mGals to a maximum of 13.69 mGals.

The corrected gravity data are included as Appendix C.

However, while the magnitude of the anomalies was diminished after applying the terrain corrections, the strong regional influence was still apparent (Figure 16). For this reason, it was deemed necessary to employ filtering methods to remove the regional overprint. The first method used was calculating a quadratic polynomial trend surface by means of Surfer[®] and subtracting this surface from the complete (terrain corrected) Bouguer anomaly map. The polynomial trend surface is shown on Figure 17 and the difference between the complete Bouguer anomaly and the polynomial is shown on Figure 18. The regional trend is largely removed and local anomalies appear to be present. In particular, the Rye Patch Fault becomes quite evident but it does appear that areas in the Humboldt Range on the eastern flank of the area appear to be over-corrected and areas in vicinity of the Florida Canyon Mine and in the northwestern portion of the study area west of the Humboldt House appear to be under-corrected. Geologically, it would not be expected to have lows in the higher elevations where bedrock is outcropping nor to have highs in an area where material has been removed by mining or in the valley which contains significant quantities of low-density alluvium even after filtering.

The next method used was band pass (wavelength) filtering. The basis of wavelength filtering is that any pattern of variation along a profile can be reproduced by combining an appropriate selection of cyclic curves (Robinson and

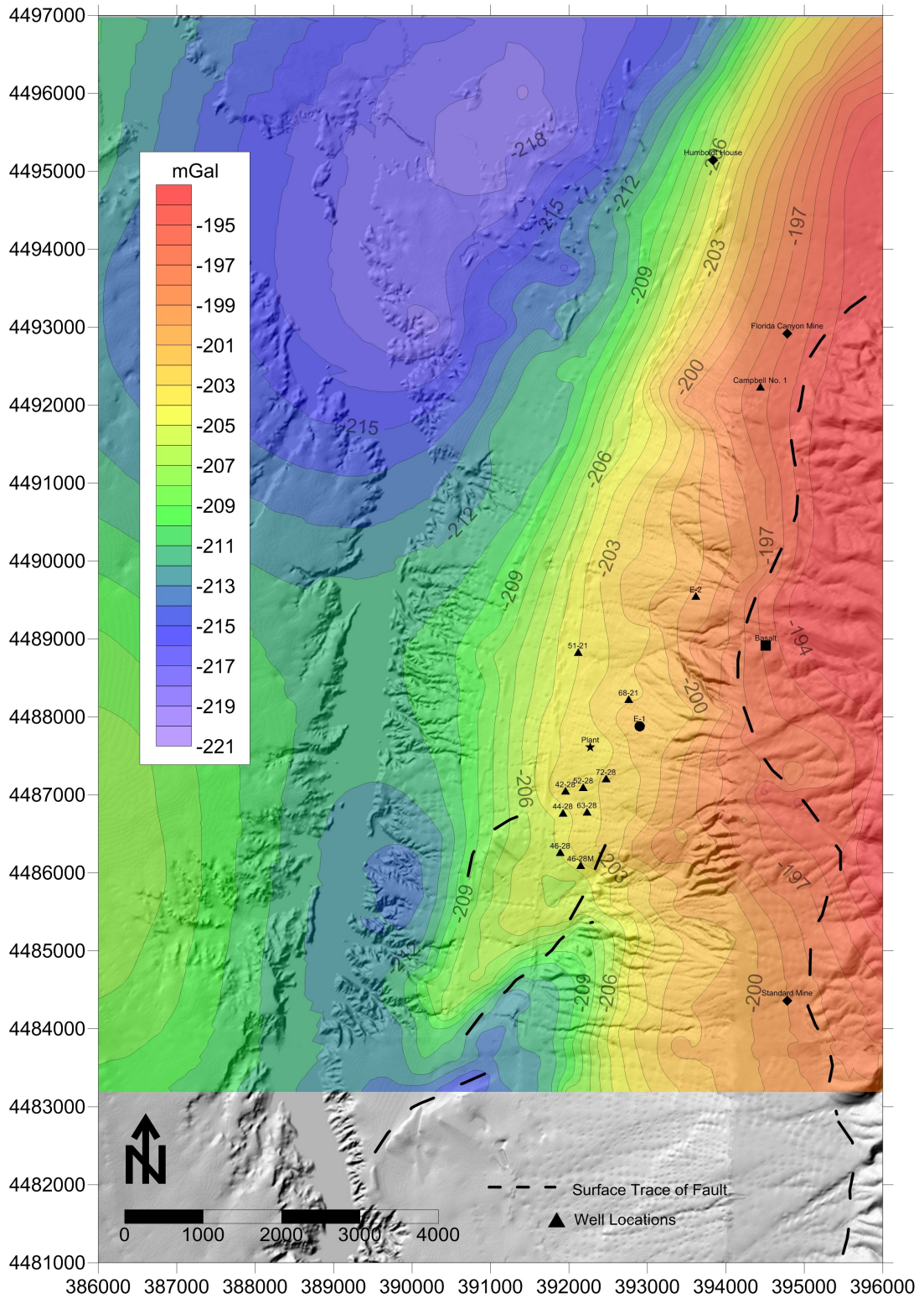


Figure 16. Terrain corrected - complete Bouguer anomaly map. Again note the strong correlation with topography.

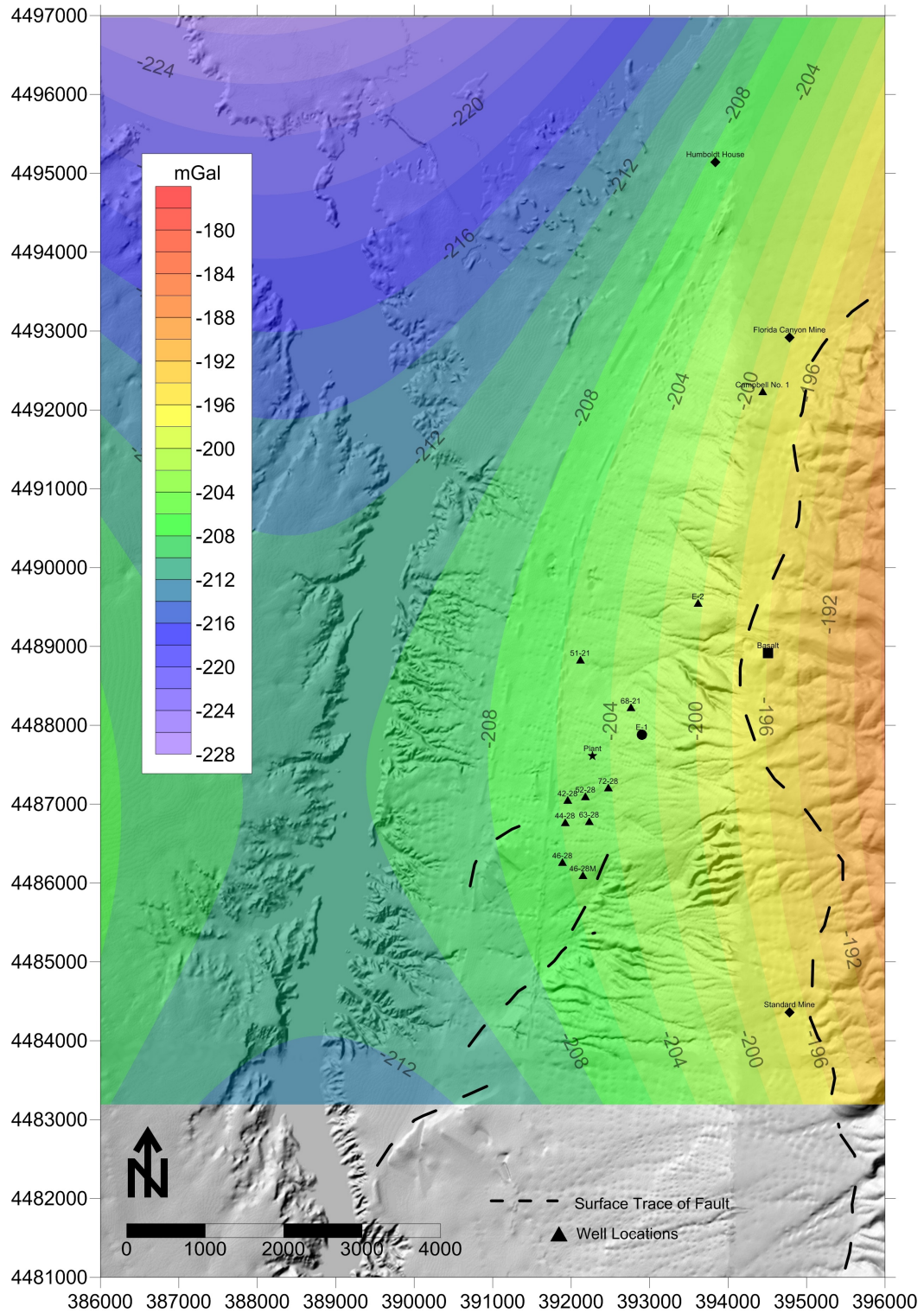


Figure 17. Quadratic polynomial trend surface map of terrain corrected gravity anomaly data.

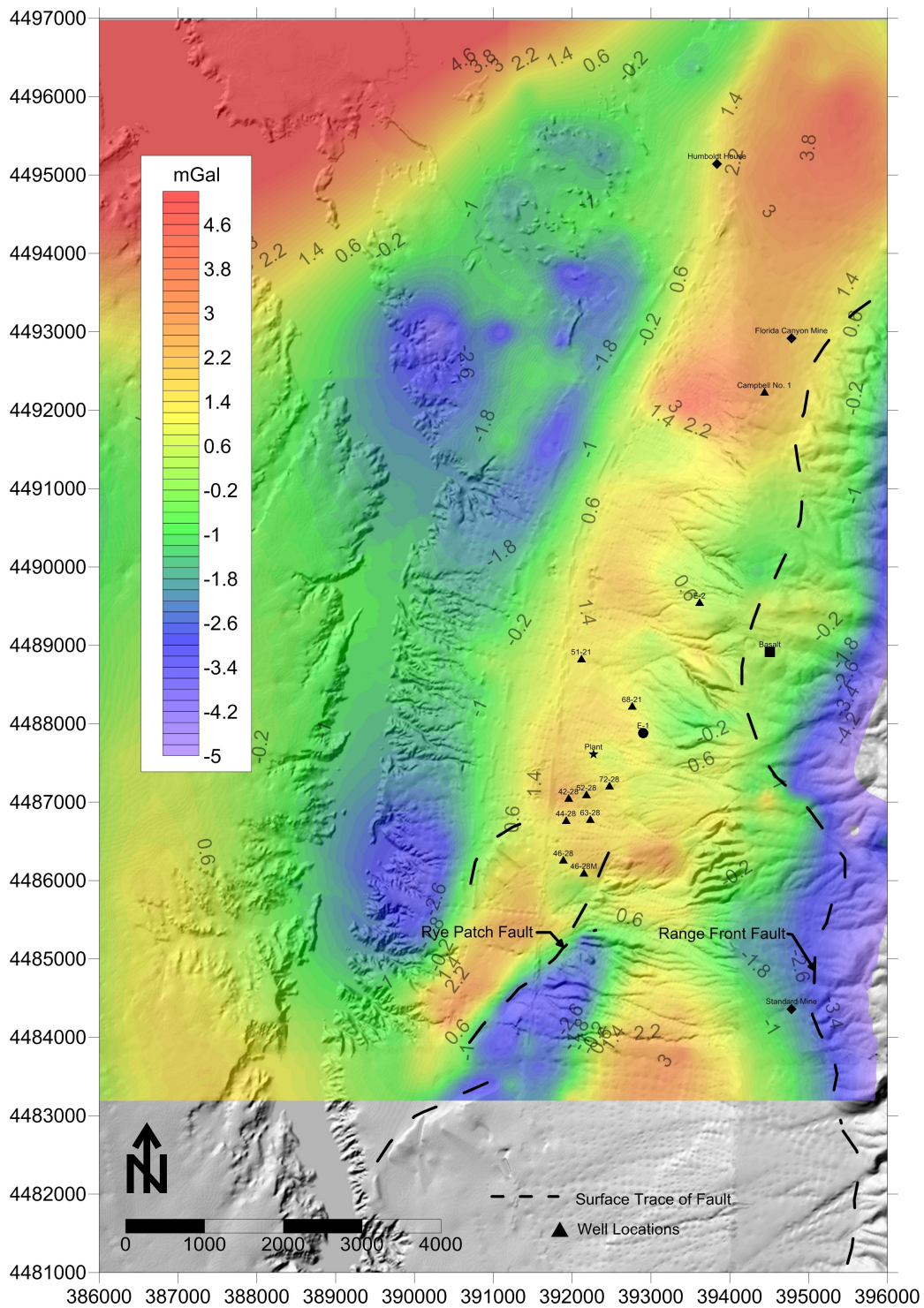


Figure 18. Map of the terrain corrected anomaly data less the quadratic polynomial trend surface.

Coruh, 1988). Any periodic waveform may be written as the sum of a number of sinusoidal terms and can be expressed in an equation. Thus, if the anomaly map can be represented by a number of cyclic curves, long wavelength or regional features or very short wavelength features that may represent noise possibly caused by variations in tidal drift not accounted for using the looping and periodic re-occupation of a base station method, slight operator errors, small undersampled anomalies between stations, or gridding artifacts (Lyatsky, 2004), those wavelengths can be removed by deleting those terms from the equation. The wavelength filtering was performed utilizing the program FFTFIL written by Hildenbrand (1983). This program transforms the input data into the wave number domain by fast Fourier transforms. The Fourier coefficients are multiplied by the wave number response of the appropriate digital filter and the resulting coefficients are inversely transformed back into the space domain. Initially, the upper band of the filtering window was established by using the approximate distance from the topographic high of the Humboldt Range to the topographic low area of the Rye Patch Reservoir (approximately 5 km) and doubling it, a distance of approximately 10 km. This was used as it should be a good representation of the regional field, i.e. the general Basin and Range structure as discussed in Chapter 3. The lower band was established somewhat arbitrarily using a value 0.1 km, approximately one-half the distance between stations, to remove short-wavelength noise as discussed above.

At the 10 km upper band, little to no reduction in the regional trend was apparent (Figure 19). Therefore the upper band was gradually reduced by trial and error with the results shown on Figures 20 through 23. As illustrated in the Figures, the regional trend is gradually diminished until at an upper window of 2 km, the apparent linear local anomalies begin to be broken up into more “bullseye” like patterns. This indicates that the filtering window has become too small and that the filter is removing linear trends that may be indicative of faults. Geologically, normal faults would not generally be expected to terminate abruptly unless encountering some other structural feature such as a transfer or accommodation zone or where the strength properties of the underlying rock drastically changed. Boring and well logs indicate that the stratigraphy is relatively consistent and drastic changes to the rock properties are not evident.

While subjective, the window of 0.1 to 4 km seems to provide the most useful representation of local anomalies as the Rye Patch Fault and Range Front Fault can be observed and generally correspond to the mappable surface traces as shown on Figure 15 and Figures 19 through 23. Also of interest is the anomaly located at the south end of the study area which corresponds with the large anomaly observed on the 2008 aeromagnetic anomaly map (Figure 24). An overlay of the two data sets is shown on Figure 25.

In addition to the filtering methods described above, the 2nd derivative of the terrain corrected data was calculated using Surfer[®] and Stanley's (1977) method of estimating the dip angle of the Rye Patch Fault and the depth to the top of the

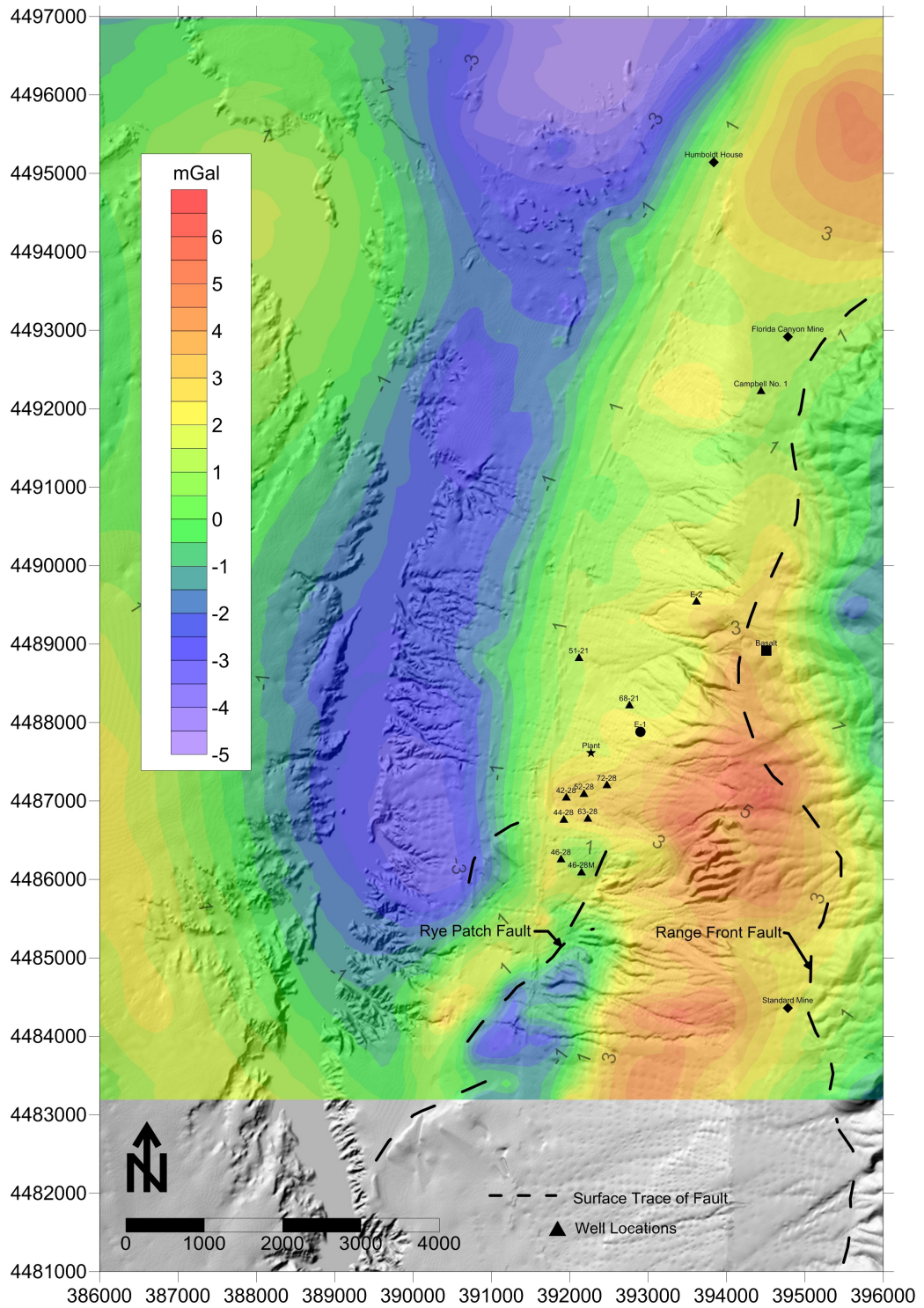


Figure 19. Wavelength filtered map with filter window from 0.1 to 10 km.

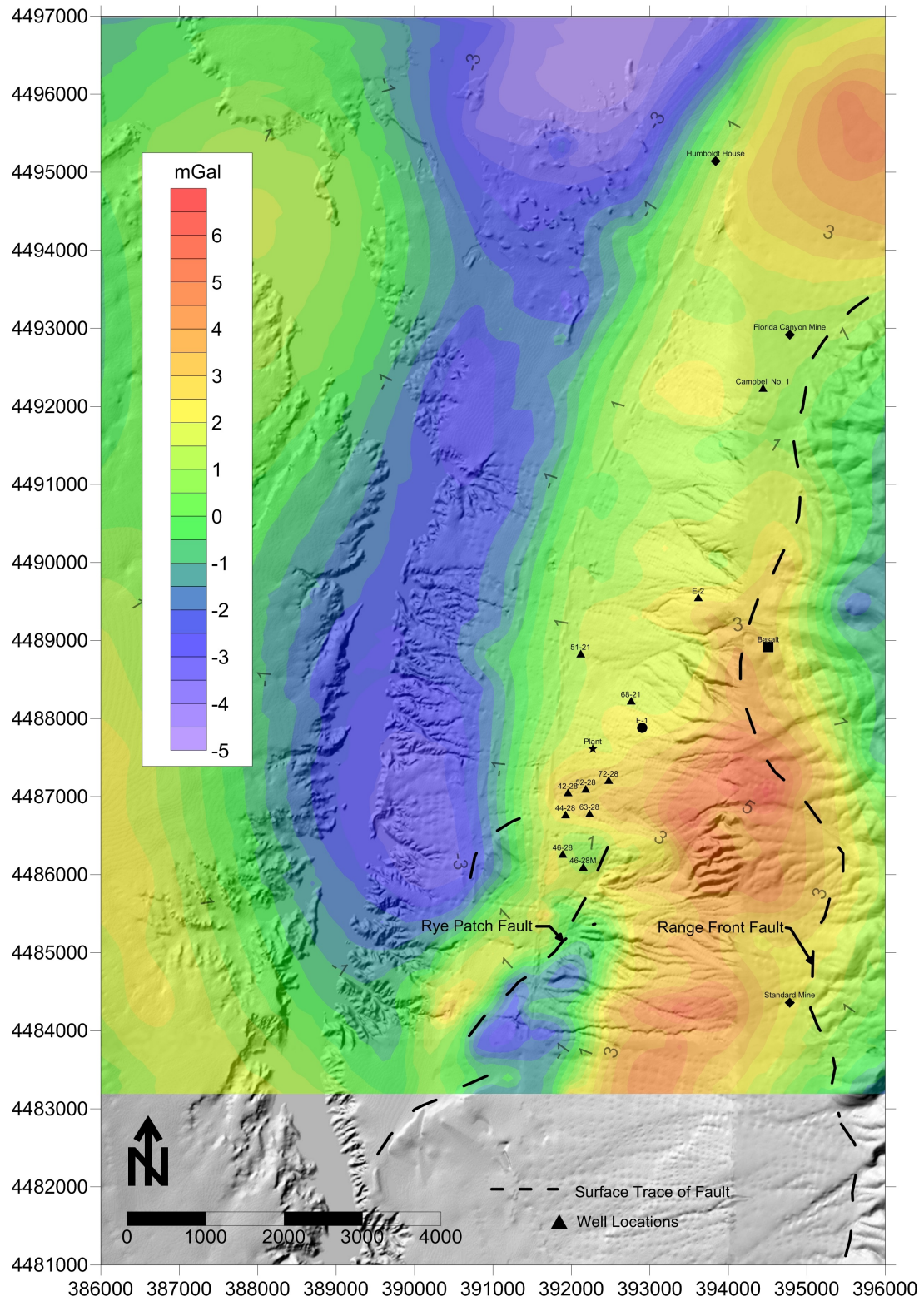


Figure 20. Wavelength filtered map with filter window from 0.1 to 8 km.

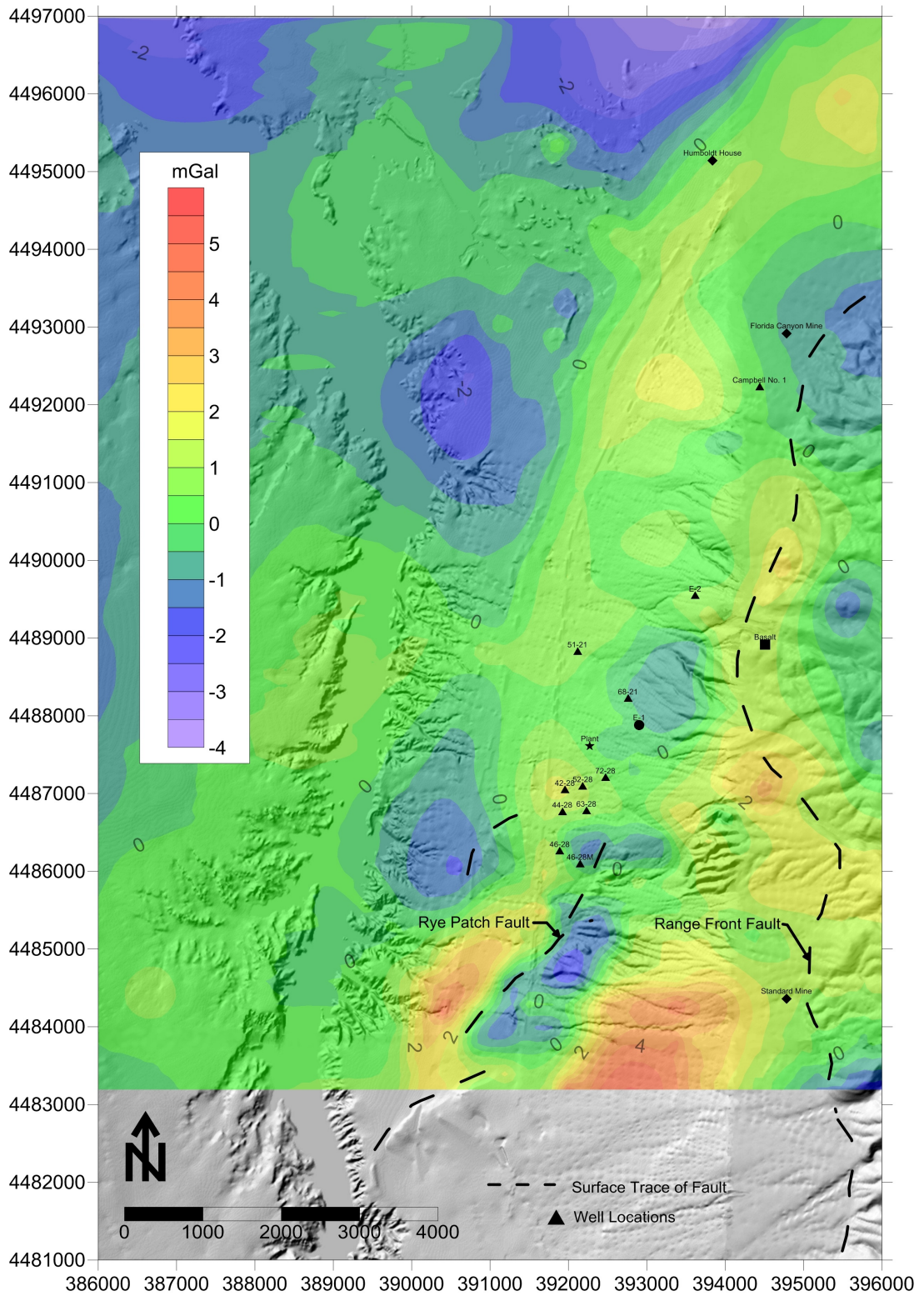


Figure 21. Wavelength filtered map with filter window from 0.1 to 6 km.

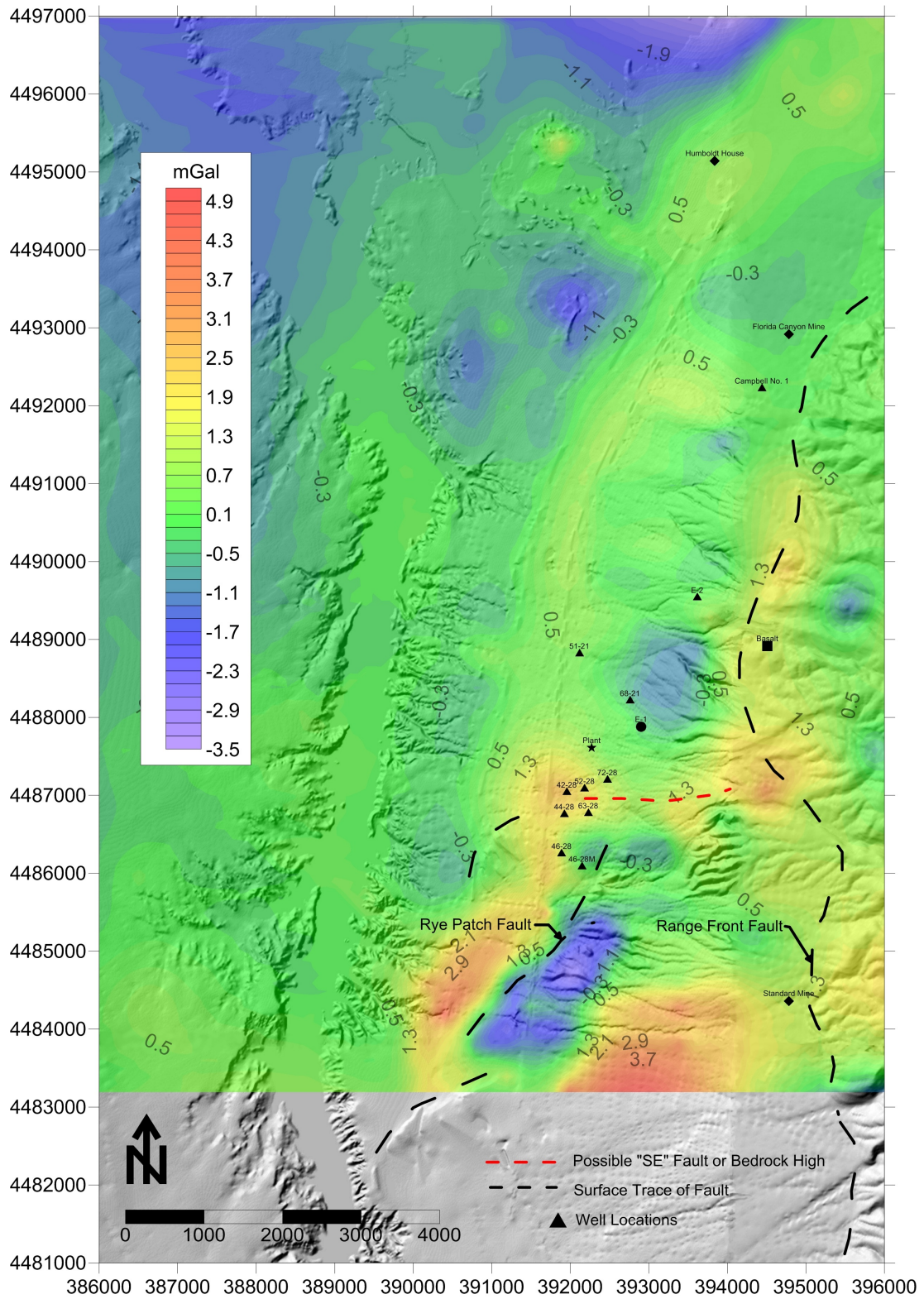


Figure 22. Wavelength filtered map with filter window from 0.1 to 4 km.

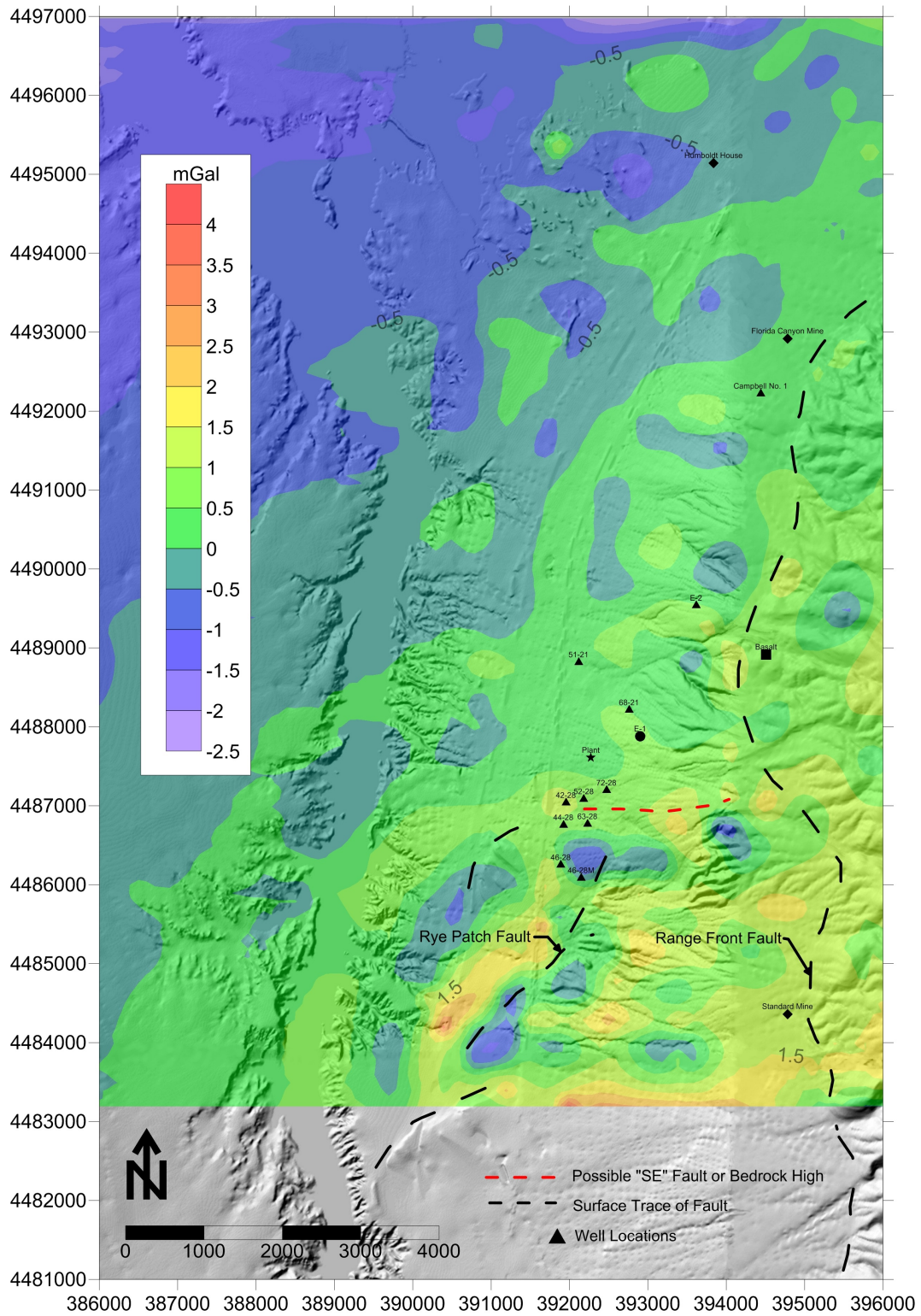


Figure 23. Wavelength filtered map with filter window from 0.1 to 2 km.

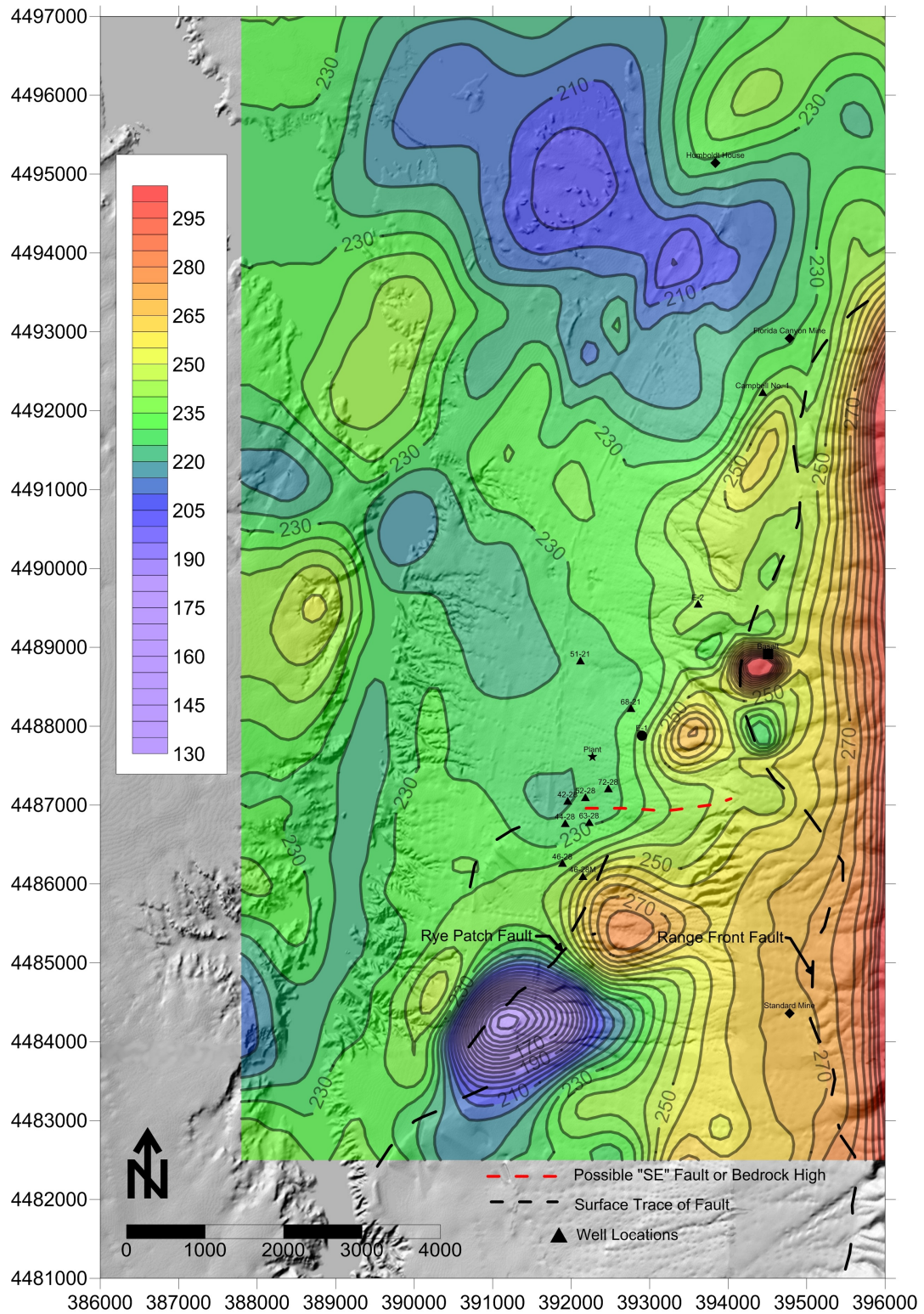


Figure 24. Decultured aeromagnetic anomaly map (modified from Ellis, 2011).

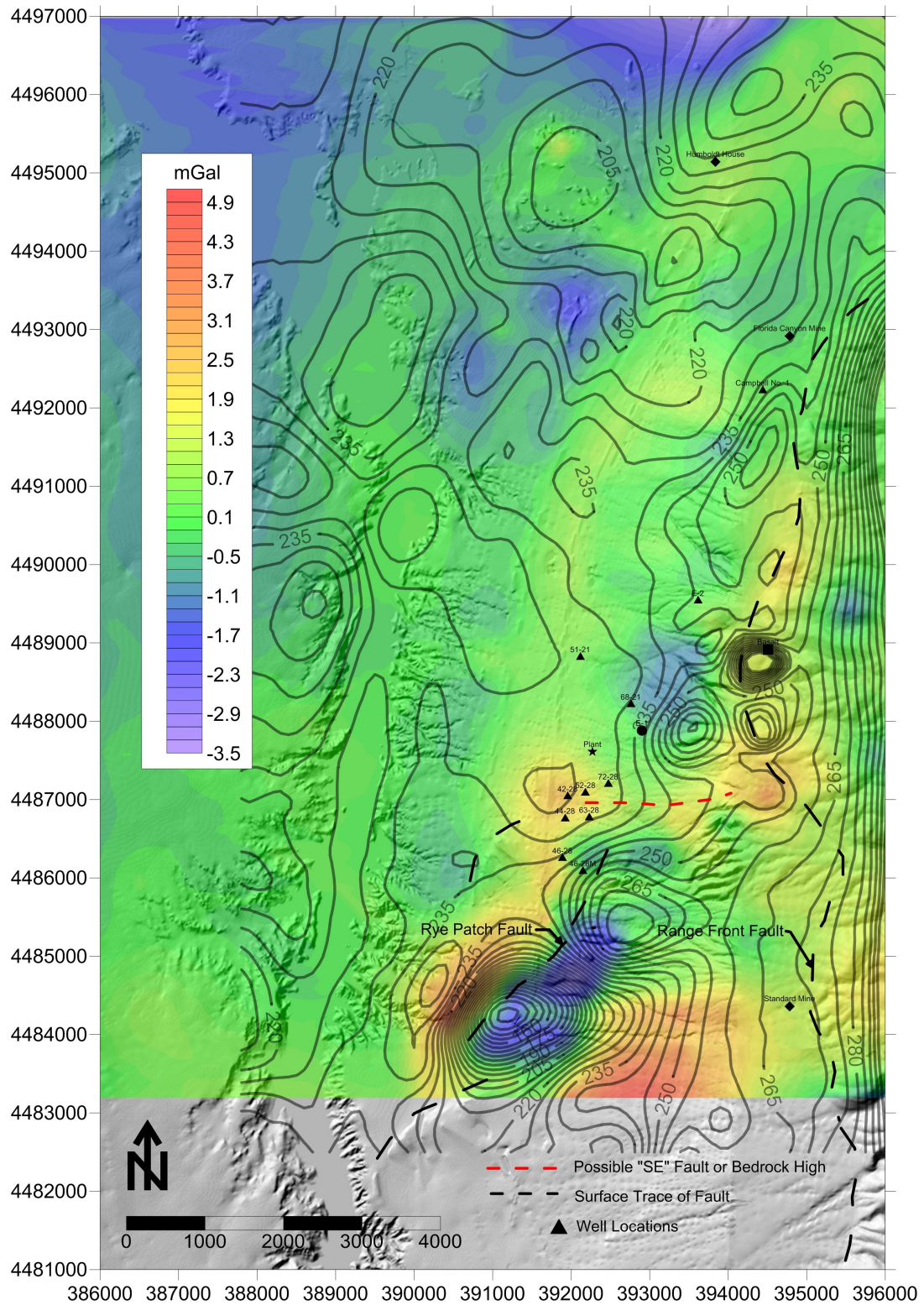


Figure 25. Aeromagnetic anomalies (contours) over gravity anomalies with a wavelength filter of 0.1 to 4 km (colors).

Paleogene volcanic layer were determined. A graph of a profile of the 2nd derivative values across the Rye Patch Fault and extending beyond the Range Front Fault (profile B-B' of Figure 31) is presented as Figure 26. The equations used to determine the dip angle and depth were:

$$\frac{(g''_{\max} + g''_{\min})}{(g''_{\max} - g''_{\min})} = \cos \alpha$$

$$-\frac{\sin \alpha (x_{\max} - x_{\min})}{2} = t$$

The equations result in a dip angle of approximately 81° and a depth of approximately 150 m. In addition to the 2nd derivative method, one-half the maximum anomaly and the equation given by Sharma (1997) for a semi-infinite slab representing an near vertical fault estimates of depth were also employed across the same profile using the filtered gravity values. The profile is shown on Figure 27 and the analysis resulted in:

$$\frac{(x_{\max \frac{1}{2}} - x_{\min \frac{1}{2}})}{2} = t = \frac{(2400 - 1420)}{2} = 490 \text{ m} \quad (\frac{1}{2}\text{-maximum technique})$$

$$Xf = (x_{\min \frac{1}{2}} - x_{\min \frac{1}{4}}) = (1420 - 1210) = 210 \text{ m} \quad (\text{from Sharma, 1997})$$

The simple 1/2-maximum technique compares more closely with the depths to the base of the alluvium in wells 42-28 (~ 715 m) and 44-28 (~ 615 m).

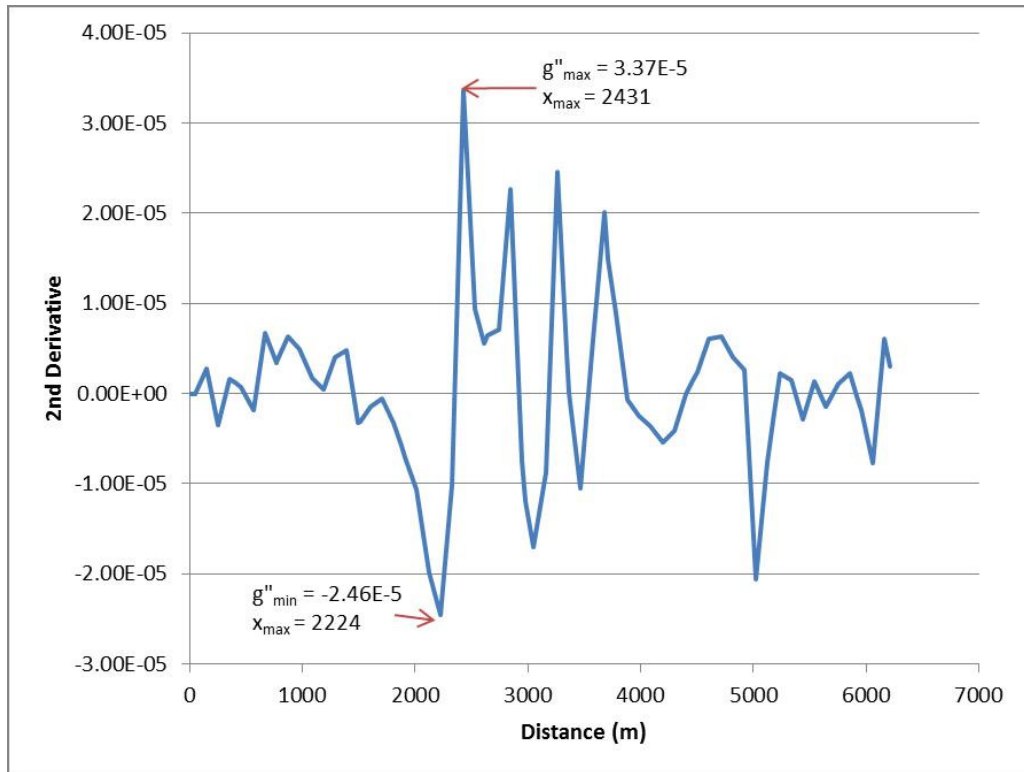


Figure 26. Graph of 2nd derivative along profile through Rye Patch and Range Front Faults (profile B-B' of Figure 31).

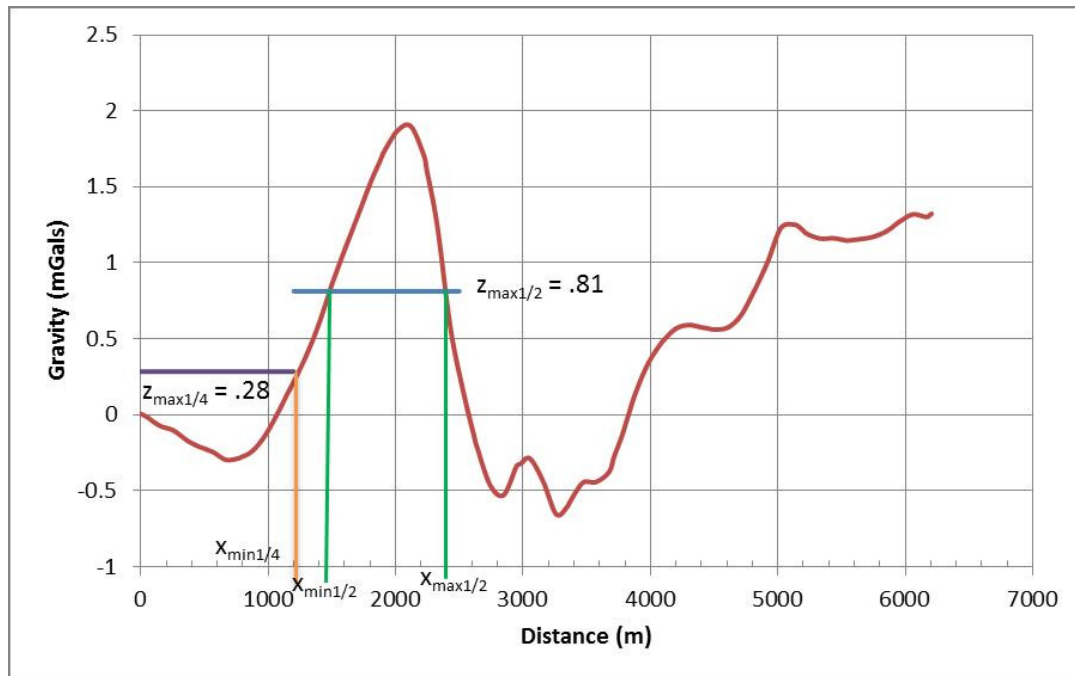


Figure 27. Graph of anomaly half-width across Rye Patch and Range Front Faults(profile B-B' of Figure 31).

Ground-Based Magnetics

In conjunction with the 2012 gravity survey, ground-based magnetometer readings were also obtained. The readings were taken with a Geometrics G-856AX Memory Mag proton precession magnetometer that has a resolution of 0.1 nanoTesla (nT) and an accuracy of 1.0 nT. At each station, several readings were taken until two consecutive readings agreed to within 1 nT. The reading was then stored into memory and also recorded in the field notebook. At several locations, the magnetometer was offset 5 to 20 m due to the presence of overhead power lines, fence lines, or railroad tracks. The offset was determined by moving away from the obstruction and taking successive readings until the readings did not change appreciably with further distance.

Typical corrections that may be required for magnetic surveys include the normal main field correction, diurnal corrections, and corrections for changes in elevation or the influence of terrain. Initially, the field readings were corrected for main field variations which account for the variation of the geomagnetic field intensity with respect to latitude and longitude. This was accomplished by using the online calculator of the National Oceanic and Atmospheric Administration (NOAA) that is available at www.ngdc.noaa.gov/geomag-web/#igrfid. Specifically, minimum and maximum values for latitude and longitude along with the survey dates were entered into the calculator and data for declination, inclination, horizontal intensity, Earth's main field intensity, and X, Y, and Z components of the main field intensity were downloaded. Gradients for the change in the main field intensity between the

minimum and maximum latitude and longitude were then calculated and an interpolation was performed for each station by first taking the difference between each station's latitude and the minimum latitude multiplied by the main field gradient of the latitude plus the main field value at the minimum latitude value. A similar operation for the longitude was then performed. Once this had been accomplished, the result was subtracted from the measured readings leading to the local intensity at each station.

The next correction that was made was to account for the diurnal variations that are the result of electromagnetic radiation emanating from the sun which ionizes particles in the ionosphere, and the tidal forces of the sun and moon that produce cyclic wind currents in the ionosphere. This correction is generally accomplished by either re-occupying a station periodically as was done for the gravity tide correction, or by establishing a base station that automatically records variations at a specified interval. For this survey, we attempted to utilize the second method. However due to operator error, the results were unsatisfactory. Specifically, on the first two days, due to security concerns, I established the base station in the parking lot of the Florida Canyon Mine. Unfortunately, car traffic in the parking lot and truck traffic from the mine caused tremendous spikes apparently each time a vehicle passed. The software that is included with the instrument, MagMap[®] 2000, allows one to filter out values above or below a specific range and this may have been possible except for another error that was made. I

also made the mistake of setting the “tune” function of the instrument to “automatic tuning” rather than entering an approximate value from the International Geomagnetic Reference Field (IGRF). The documentation of the magnetometer states that when using this option, the meter is tuned to the last reading which seemed reasonable. However, with the vehicle traffic described above, the previous value was frequently greatly influenced resulting in poor tuning for subsequent readings. After downloading and evaluation of the first two days of the base station measurements, it became obvious that the parking lot was a poor choice of locations.

For the remaining days of the field work, we established the base station at the same location as the temporary gravity base stations taking care to place it in locations where it was difficult for a passerby to observe (e.g. hiding it behind sage brush). Unfortunately, I continued to use the auto-tune feature and while the data were downloaded and viewed each evening, it was not apparent that the data were poor as the diurnal variations appeared to follow a similar pattern as an example provided in the meter’s documentation. Upon return from the field and while processing the data, it became apparent that the diurnal variations that had been recorded were an order of a magnitude different than what would normally be expected. As a magnetic storm was not recorded at permanent global stations for the dates the field work was conducted, it was determined that the base station data that had been recorded was erroneous and unsuitable for use. To test this assumption, I set the meter up at a local park by first taking measurements using the

auto-tune option for an hour, and then manually tuning the instrument and taking recordings for an hour. Upon doing so, it was found that the maximum auto-tune values that were recorded were approximately an order of magnitude different than the values obtained using the manual tune method similar to that which was recorded during the field work.

As an alternative, data for the survey dates from the two closest permanent continually recording INTERMAGNET Magnetic Observatories (IMOs) located at Boulder, CO and Fresno, CA were downloaded from the INTERMAGNET website at: <http://www.intermagnet.org/data-donnee/data-eng.php>. A weighted average based on the distance from the IMOs to the project site was calculated and this data was used to account for diurnal variations on the premise that perturbation at the three locations would occur at approximately the same time. The recorded times of the station readings were adjusted to match Greenwich Mean Time (GMT) and interpolation of the diurnal corrections as calculated above was performed.

Corrections for elevation and terrain were not performed as at the latitude of the project site, the gradient of variations in the main field from changes in elevation is on the order of 0.025 nT/m. As the difference between the maximum and minimum elevations was approximately 180 m, the maximum correction would be on the order of 4.5 nT which would be insufficient to appreciably vary the anomalies or outweigh general background noise.

After performing the corrections, an anomaly map was produced using Surfer[®]. Examination of the anomaly map indicated that there were a number of

isolated points that varied greatly from adjacent points resulting in “bullseye” features on the map indicating probable erroneous data. These points were removed from the dataset and a new map was generated. There were again several “bullseye” features but at much less magnitude than the prior ones that had been removed, so the mean and standard deviation of the data (minus the aforementioned major outliers) were calculated. The data were then screened and any values that exceeded two times the standard deviation from the mean were also removed. An anomaly map of the processed data is presented as Figure 28. Overlays of the aeromagnetic and gravity data in comparison to the ground-based magnetic data are shown in Figures 29 and 30 and the processed data is included as Appendix D.

Modeling

After the gravity and magnetic data had been processed, forward modeling was performed using Geosoft’s GM-SYS[®] Profile Modeling software version 4.1, laboratory edition. Certain limitations with this version and edition required some simplification of the models. Specifically, the software was limited to 35 stations and 8 blocks per profile.

Other simplifying assumptions that were used included that the model layers (or formations) were homogeneous of constant density and of relatively constant thickness. Additionally, it was assumed that the model layers extended laterally to infinity although in practice this was accomplished by extending the layers 30 km in both directions.

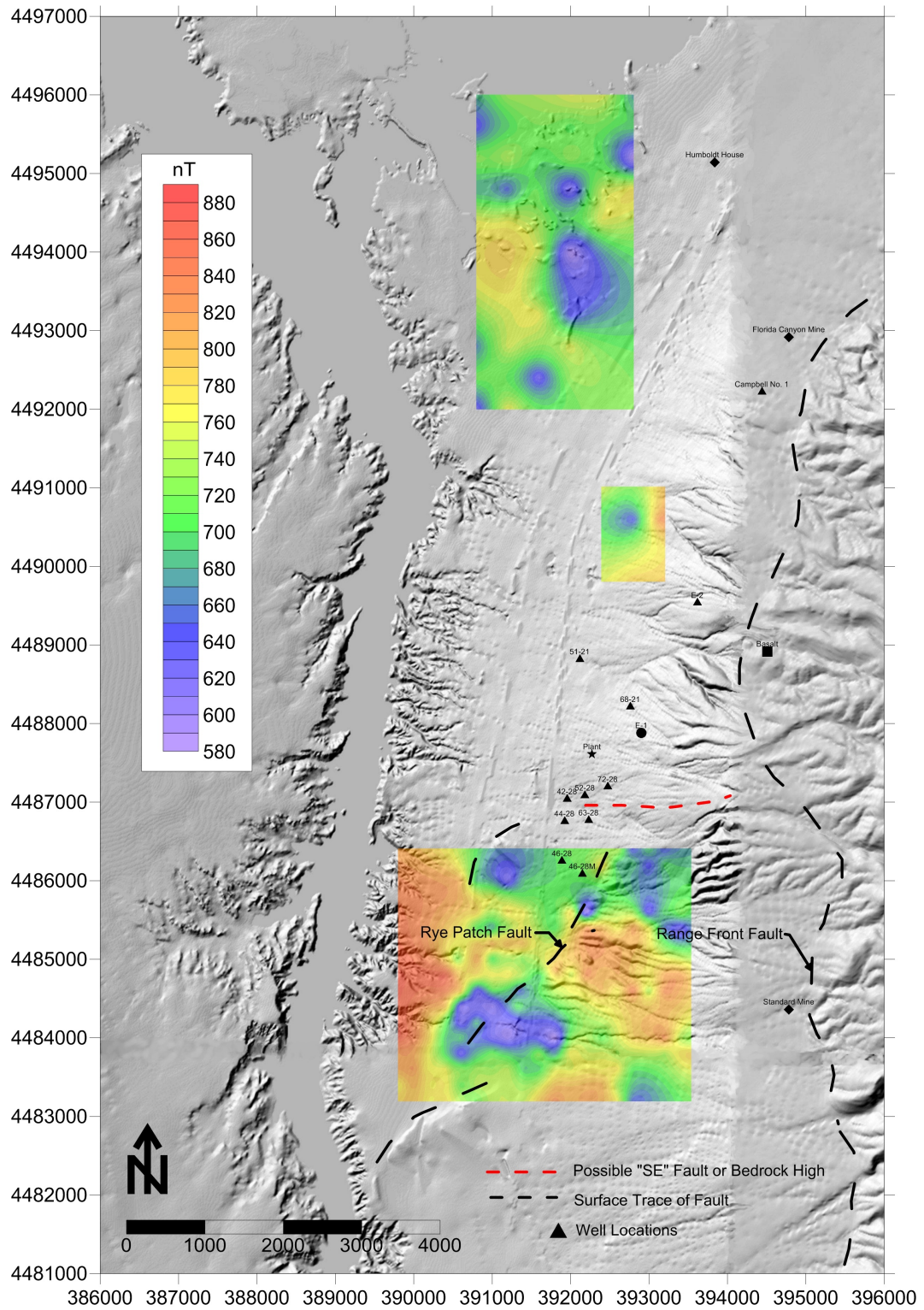


Figure 28. Ground-based magnetic anomaly map.

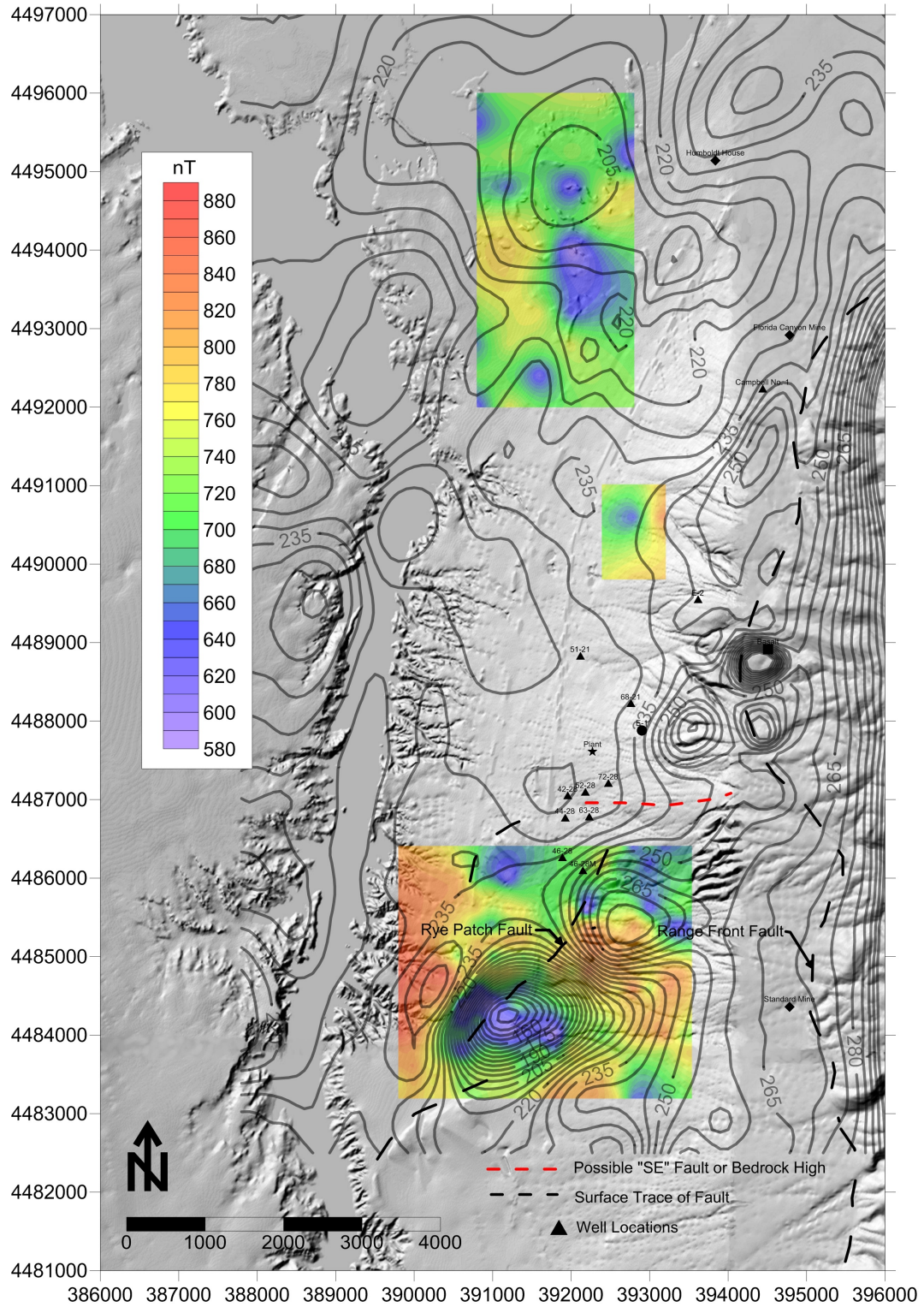


Figure 29. Aeromagnetic anomalies (contours) over ground-based magnetic anomalies (colors).

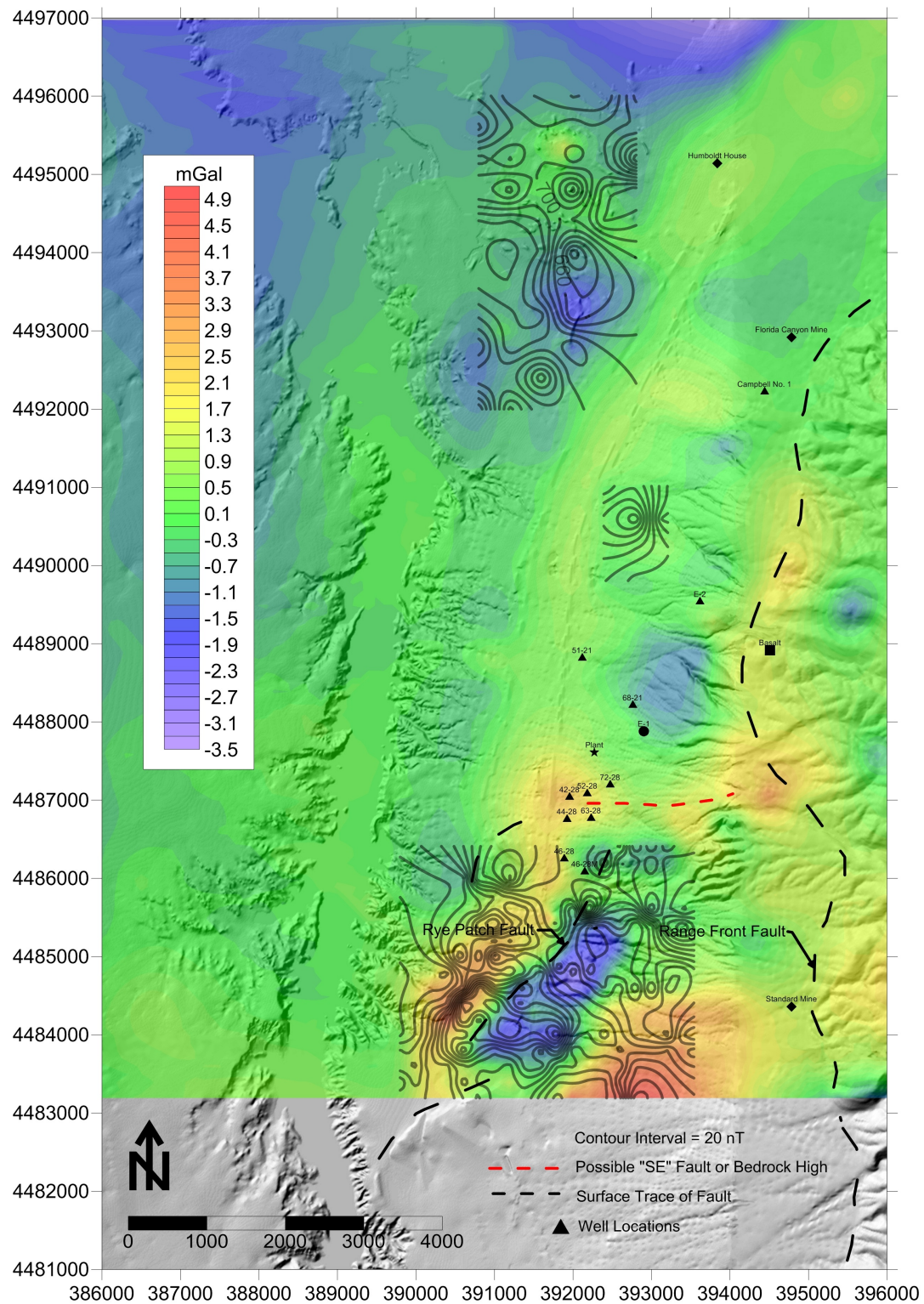


Figure 30. Ground-based magnetic anomalies (contours) over gravity anomalies with a wavelength filter of 0.1 to 4 km (colors).

Three profiles were constructed at the locations shown on Figure 31. The first profile, A-A', was constructed north of the existing plant along the approximate VSP Line 100 of the seismic survey conducted by Presco Energy (Ellis, 2011). This location was used as Ellis (2011) also constructed a structural cross-section along this line as presented as Figure 11 above. The principle purpose of this profile was to evaluate the probable gravity and magnetic response to such a cross-section and to provide a rough calibration of the densities of the respective formations. Section B-B' was located just to the south of the existing plant at a location that crossed the Rye Patch Fault anomaly, the adjacent gravity low, and extending across the Range Front Fault. In addition to crossing these features, it was close to two wells (42-28 and 44-28) that had detailed logs (see Appendix A) thus providing some information on formation thicknesses and depths.

Section C-C' was chosen at the location of the southern anomaly. While control such as well logs or seismic information was very limited in this area, it was hoped that the modeling would provide some insight as to what structural features could be causing this anomaly. The well data used for Section B-B' was also used as a starting point for this profile.

Gravity, magnetic, and topographic data for each profile were obtained by using the "slice" feature of Surfer[®] on previously gridded data. This resulted in obtaining northing, easting, distance along profile, and the selected parameter (e.g. filtered gravity) data in ASCII space delimited format which was then entered into a

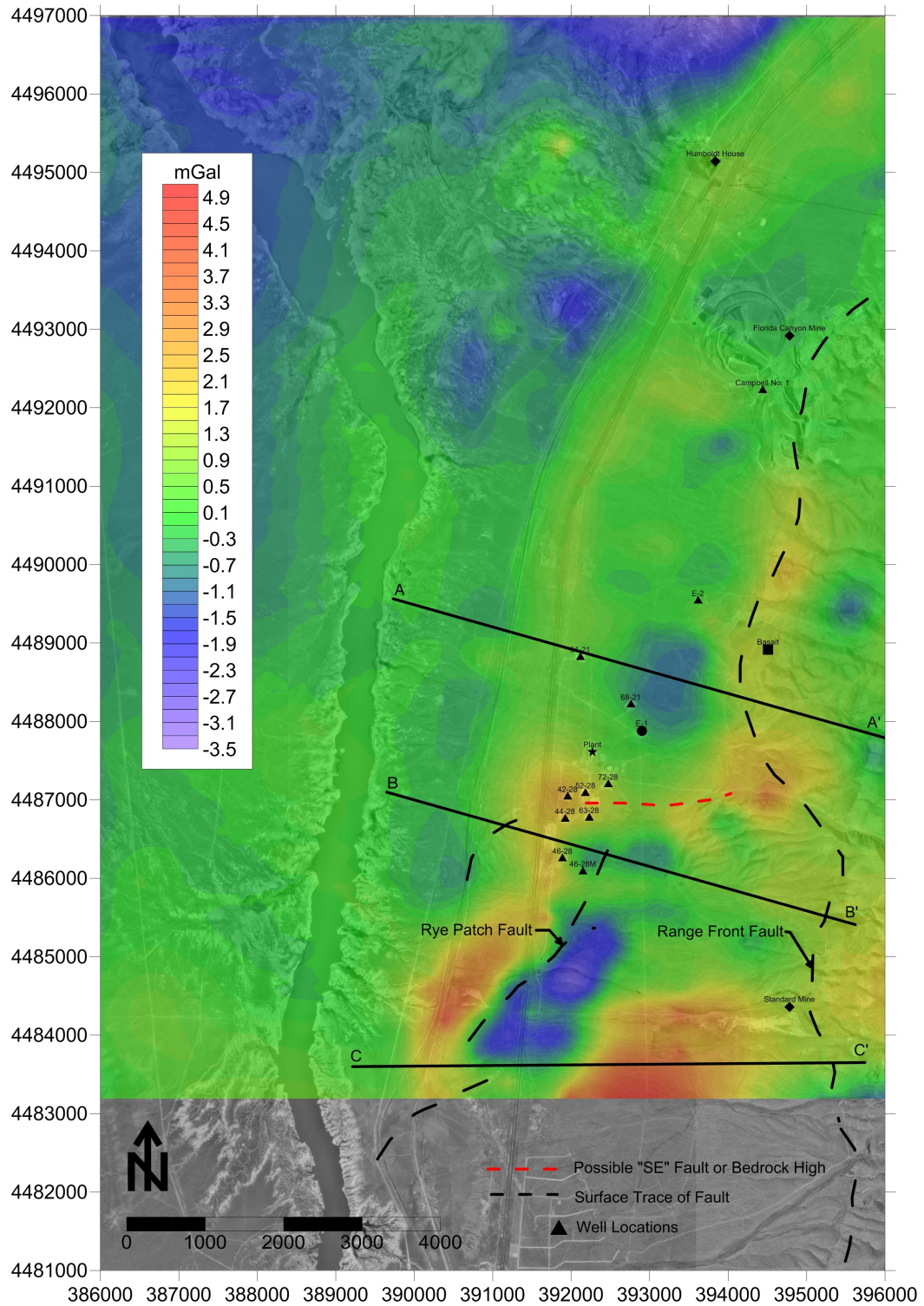


Figure 31. Locations of modeling profiles. A-A' is located along existing seismic line, B-B' located across Rey Patch Fault and Range Front Fault, and C-C' crossing large anomaly in southern portion of the study area.

spreadsheet. The slice feature takes data from grid nodes along the profile resulting in approximately 80 points for each profile based on the grid size that had been used and the lengths of the profiles. As mentioned above, the GM-SYS[®] version and license used for the modeling was restricted to 35 points for each profile, therefore data points were eliminated based on distance between stations. This resulted in profiles of 35 points with a typical distance between stations of around 200 m.

Once the profiles had been reduced to 35 stations, the data to be modeled for each profile was entered into the GM-SYS[®] program. For Section A-A', the elevations, terrain-corrected gravity data, and the aeromagnetic data were entered. After this had been completed, a raster image of the structural cross-section (per Figure 11) was imported into the GM-SYS[®] program to be used as a backdrop. Two points on the image were selected and horizontal and vertical coordinates for both points were entered for each which resulted in the image being scaled in both directions to match the profile data. During data input, the profile azimuth and strike (105° and 15°, respectively) were entered along with the local magnetic main field intensity (51150 nT), declination (13.9°) and inclination (64.5°) per the IGRF. The structural cross-section backdrop was then “traced” for the formations and values for density and magnetic susceptibility were assigned to each formation. Initial estimates of the density and magnetic susceptibility values were obtained from Telford et al. (1976) and these parameters were adjusted during modeling ultimately resulting in the values listed in Table 1.

Table 1. Density and magnetic susceptibility values used in modeling.

Formation	Lithology	Density (g/cm³)	Susceptibility x 10⁶ emu
Alluvium	Clays, silts, sands and gravels with interbedded sinter deposits	2.2	20
Paleogene Volcanics	Volcanics	2.8	350
Grass Valley	Mudstone and sandstone variably recrystallized to argillite, slates and quartzite	2.7	80
Natchez Pass	Massive carbonates with volcanics	2.67	130
Natchez Pass Clastic	Sandstone, siltstone and claystone	2.5	30
Prida	Limestone and dolomite	2.7	20
Crustal Rock	--	2.67	30

The terrain corrected gravity and aeromagnetic data was modeled for profile A-A'. The terrain corrected data were chosen because the structural cross-section that was used as a basis for the model was not filtered and reflects the dip of the formations extending into the Humboldt Range. The aeromagnetic data were chosen because ground-based gravity measurements were not obtained in the vicinity of the profile. As the program was constrained to eight blocks, the Upper Natchez Pass was excluded and a crustal block was included for this profile. Again, the general purpose of this profile was to determine reasonable values for the densities and magnetic susceptibilities and to evaluate the modeled gravitational and magnetic response to the cross-section as developed by Ellis (2011). The results are presented as Figure 32. Upon examination, it is apparent that both the modeled gravity and magnetic anomalies are greatly subdued by the regional trend providing additional support for the filtering that was discussed above. The error

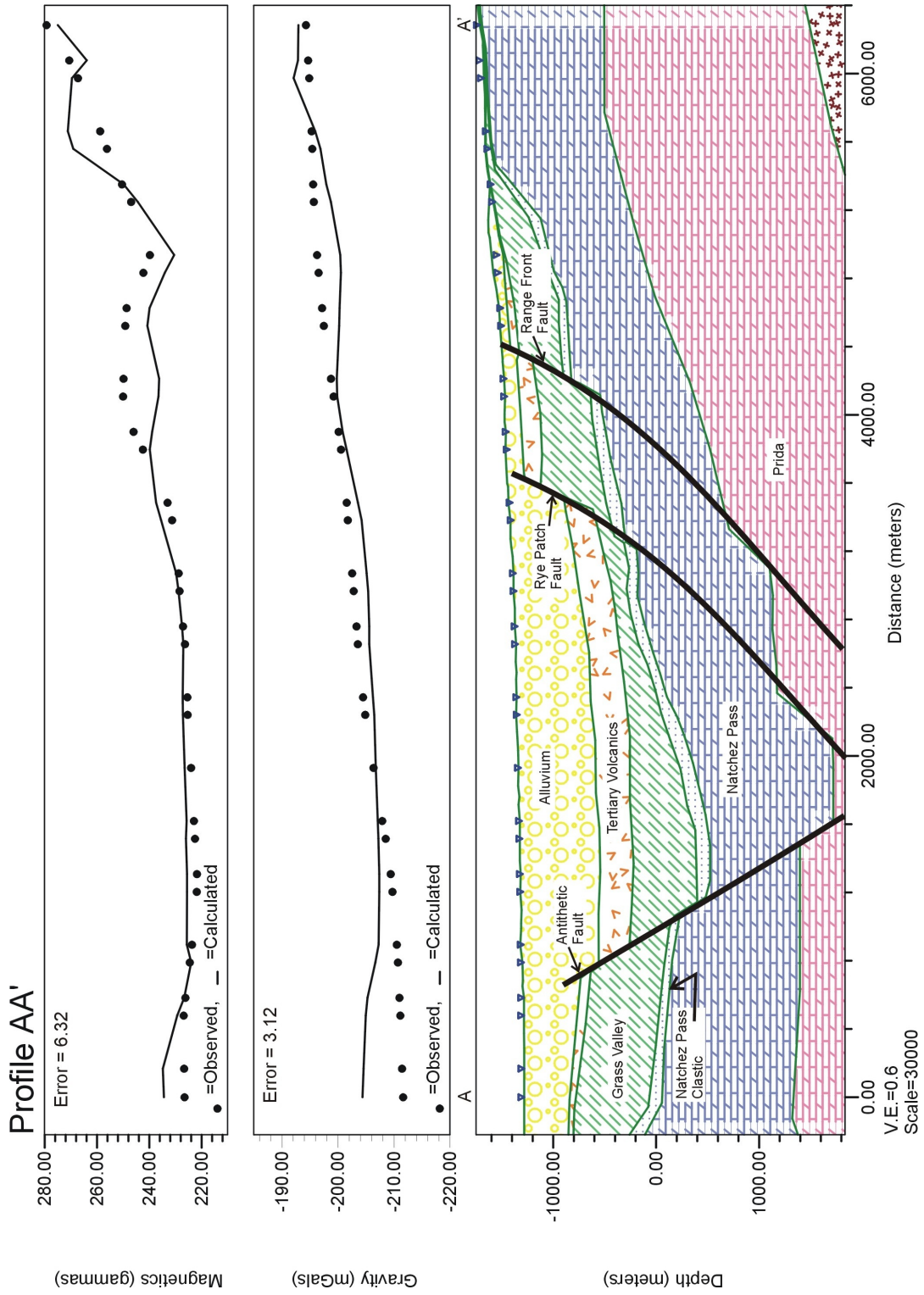


Figure 32. Model results for profile A-A'.

noted in the magnetic and gravity panes of the figure is the cumulative difference between the observed and calculated values.

For sections B-B' and C-C', the filtered gravity (1 to 4 km) was used in the model. Initial depths and thicknesses were based on the information from wells 42-28 and 44-28. The dips of the faults were assumed to be steep to the west and the value of 81° calculated using the 2nd derivative method as discussed in the gravity section above was initially used. For these two profiles the Natchez Pass Formation was divided into upper and lower segments separated by the clastic unit and, in essence, the Prida Formation was taken to be "crustal rock" by adjusting its density to 2.67 g/cm^3 . Once the blocks had been constructed, an iterative (although manual) process was used until the error was minimized. The results are shown in Figures 33 and 34.

It should be noted that modeling of potential field data is non-unique in that a number of different configurations can generate similar gravity and magnetic signals. However, based on the standard conceptual models of basin and range faulting and of the geothermal systems in the area (Figures 6 through 10) combined with the local geologic information from wells and seismic surveys, the models presented appear to be good estimates of the basic structure of the southern portion of the KGRA. As there were no major anomalies in the northern portion of the KGRA near the Humboldt House and as there was very little information that could be used as constraints, model profiles in that area were not created. Additional constraints such as more well and/or seismic information would greatly enhance

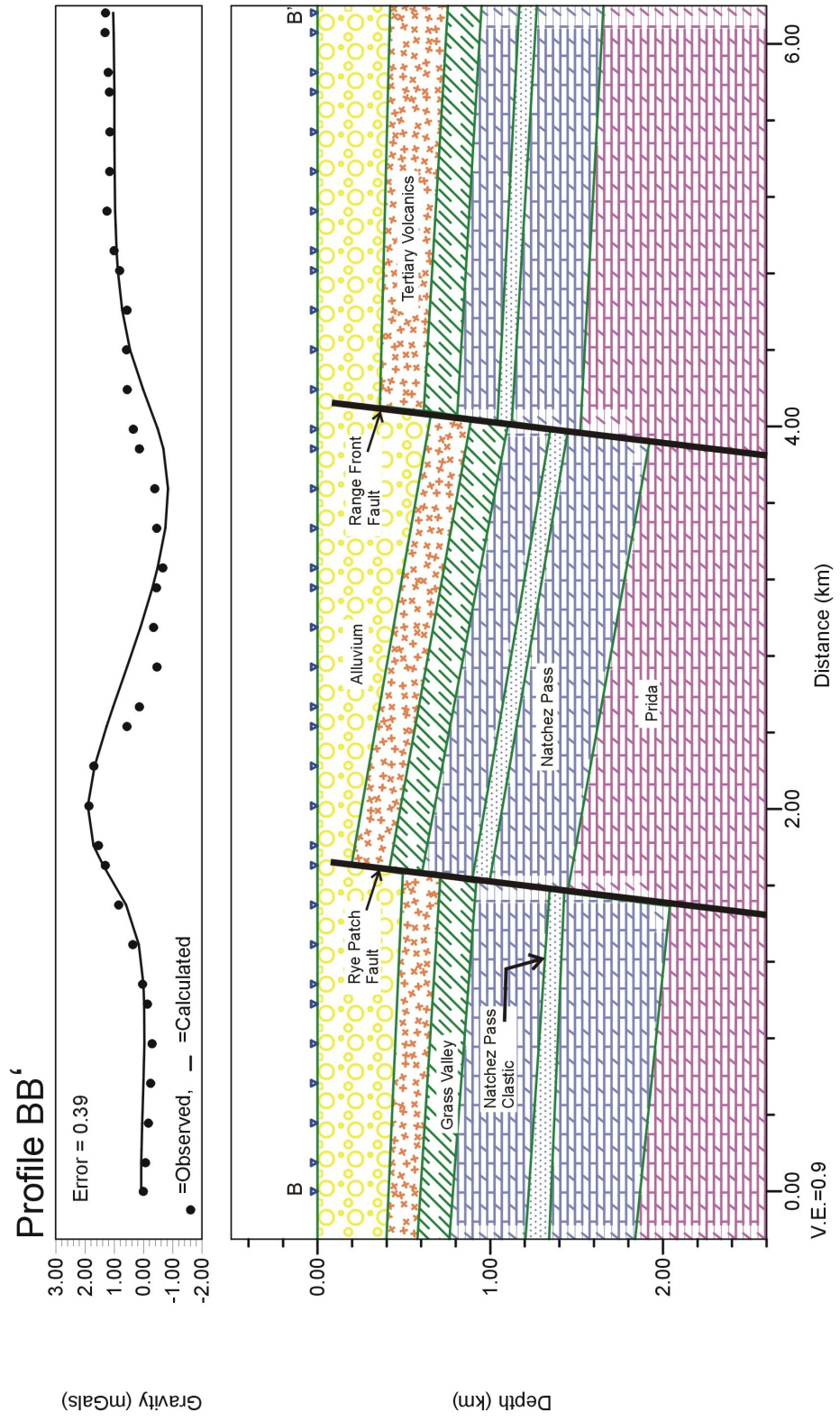


Figure 33. Model results for profile B-B'.

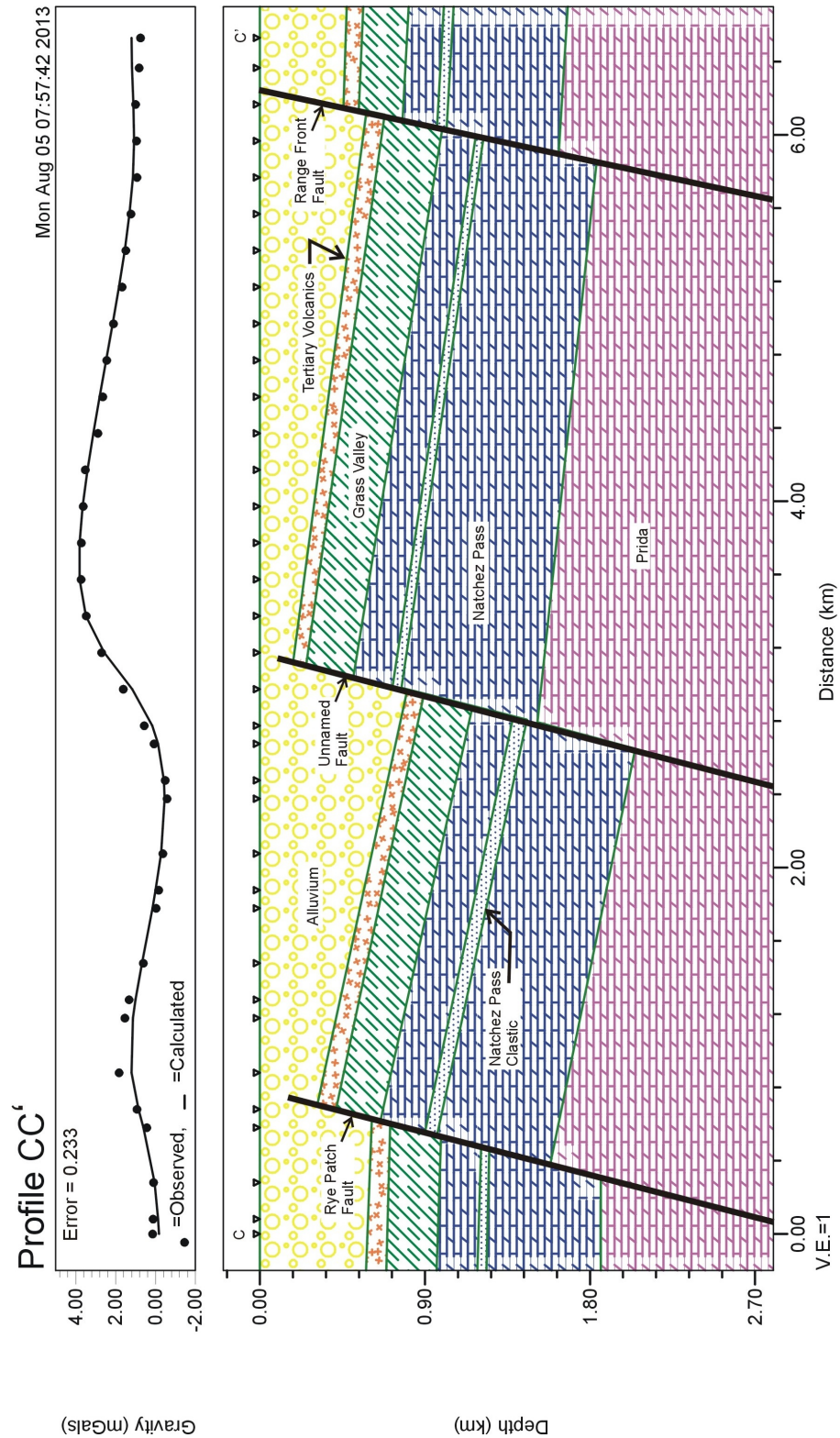


Figure 34. Model results for profile C-C'.

the ability to create a model more definitive of such things as structures, formation thicknesses and depths.

CHAPTER V - DISCUSSION AND CONCLUSIONS

The results of the survey indicate that the gravity method can be useful in identifying structural features that may be conduits for fluid flow per the currently accepted model of Basin and Range geothermal systems. However, due to the typical structure of the Basin and Range of mountain ranges separated by wide valleys as the result of crustal extension and normal faulting, removal of the regional trend is necessary. While terrain corrections reduce the influence of topography, due to the large density contrast between the low density valley fill and alluvium with the near surface or outcropping higher density bedrock formations in the higher elevations, a strong regional field significantly overprints local anomalies. Neither the Nettleton (1971) nor the Parasnis (1979) methods were found to be effective for determining a more suitable site-specific reduction density for similar reasons.

Filtering by removal of the regional polynomial trend surface was rapid using modern software and generally retains linear features, however it appears to over- or under-correct in areas and the anomalies were more diffuse than what the wavelength filtering technique could accommodate. Wavelength filtering appears to be effective in removal of the regional trend although it may truncate linear features if the wavelength filter is too low. It also required trial and error to achieve results which satisfactorily remove the regional trend and allow discernment of the local

features of interest such as the Rye Patch and Range Front Faults and the possible transfer or accommodation zones.

The filtered results clearly show anomalies from the Rye Patch Fault and the Range Front Fault, particularly in the area of the existing plant (Figures 22 and 35). Also of note in this area is the gravity high trending to the northeast with an azimuth of about 82 degrees. This is at the approximate location as the “southeast” fault noted by Feighner (1998, 1999), Teplow (1999), Gritto et al. (2003) and Sanyal (2006). Another smaller feature parallel to the southeast fault appears to be present slightly to the south. These features are most likely an accommodation or transfer zone with oblique-slip movement as the gravity high indicates some vertical offset. The large anomaly at the south end of the study area may also be a normal fault that is terminated by another transfer or accommodation zone as postulated by Ellis (2011). These features are shown on the shaded relief map in Figure 35.

In the area of the Humboldt House and the sinter deposits, northeast trending features such as those identified by MacNight et al. (2005) or the antithetic faults suggested by Ellis (2011) are not discernable although there is a significant gravity low in this area. If these faults are present, it may be that there is insufficient offset to generate a well defined gravity signal or that the majority of offset is located to the west of the study area. Higher resolution (closer spacing) of gravity meter readings might also improve the results.

Estimates of fault dip angles appear to confirm that they are high angle (on the order of 80°) as the previous conceptual models suggest. Estimates of the

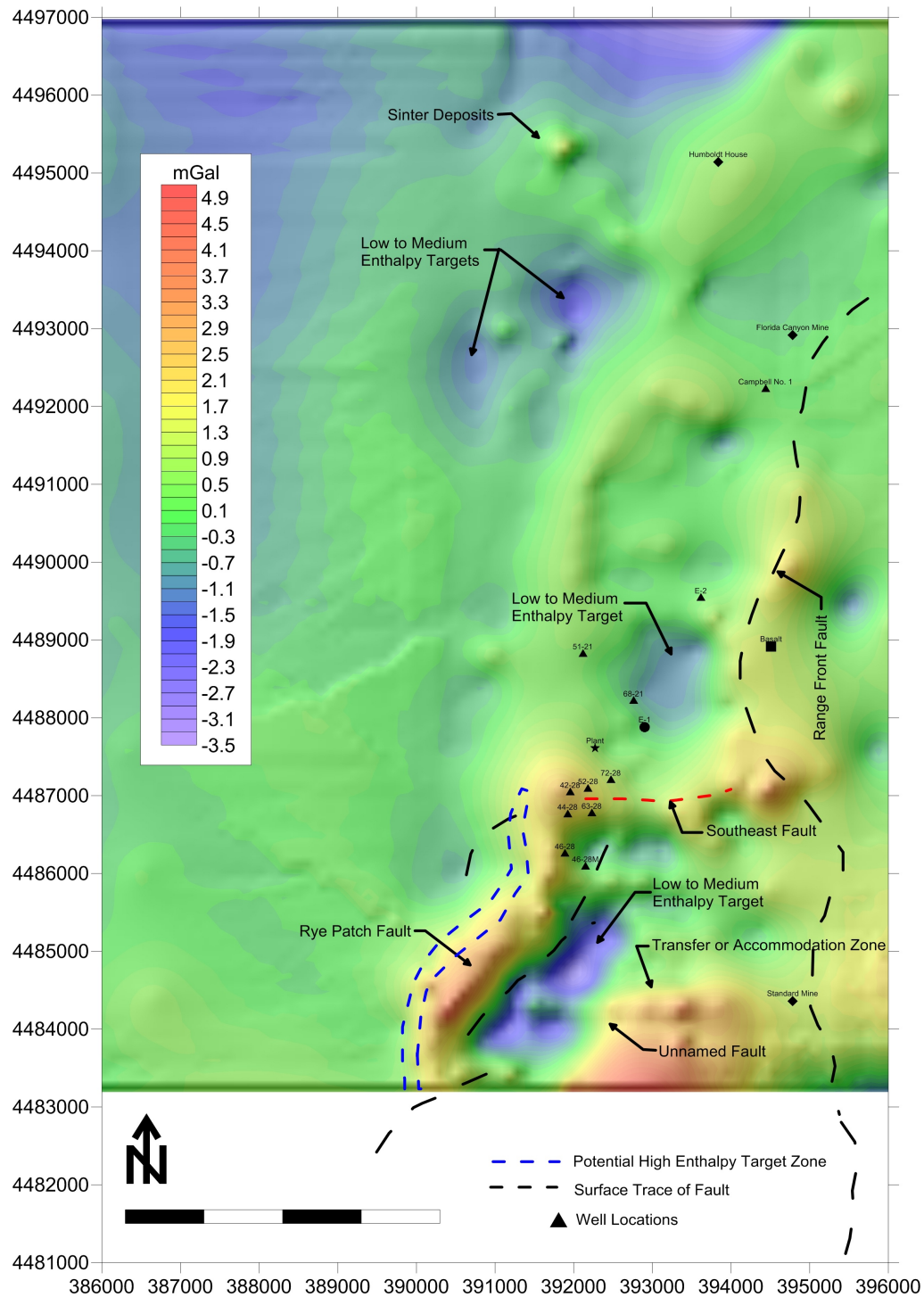


Figure 35. Shaded relief map of 1 to 4 km filtered gravity anomalies. Low to medium enthalpy targets include gravity anomaly lows south of the sinter deposits, northeast of the existing plant, and at the southern end of the study area between the Rye Patch and unnamed faults. High enthalpy targets may exist on the west side of the Rye Patch Fault.

depths to the bottom of the alluvium are tenuous at best although the estimates arrived at using the half-maximum (without multiplier) anomaly width arrive at estimates of approximately 460 m. This estimate appears to compare with well 44-28 (620 m) if it is located on the down-dip side of a rotated block as discussed below.

Results of the ground-based magnetics were poor at best principally due to operator error. In addition, it was only performed during the 2012 survey and therefore covered only portions of the study area. It did however indicate an anomaly in the southern-most area that is coincident with the filtered gravity and aeromagnetics. It can also be performed much more rapidly than the gravity survey as it is not as dependent on having as stringent location data and use of a handheld GPS unit would suffice. For this site, it is believed that there would be a sufficient contrast in magnetic susceptibilities between the Paleogene volcanics with the alluvium and principally carbonates of the other formations such that the location of structural features such as faults could be discerned if diurnal variations were accurately recorded, and could be considered as part of a future study.

The model results indicate that the gross geologic structure of the KGRA follows the general structure of similar Basin and Range systems. While previous conceptual models of the site generally have parallel or west dipping horst blocks, the model results suggest steep normal faults with a rotation and tilting of the blocks in the opposite direction (to the east). This configuration appears to create smaller "sub-basins" between the range front fault and subsequent piedmont faults.

It should again be cautioned that the models developed for this study are non-unique although they appear to adequately produce calculated gravity signals that are similar to the observed (albeit filtered) gravity data. On that note, the regional trend was removed by the filtering and the regional dip to the west may need to be added to more accurately depict the actual geometry. Depths, thicknesses, and fault dip angles of the models should also be viewed with caution as they are largely a function of assumed density contrasts. Greater control such as more well or seismic information and data on actual rock densities would undoubtedly improve the models.

However, on the basis of even the simple models presented above, it appears that the majority of the production wells, with the possible exception of the western-most wells (in particular 42-28, 44-28 and 46-28), are located on the east side of the Rye Patch Fault. Wells 42-28, 44-28, and 46-28 appear to be located very near to the edge of the fault. The apparent oblique-slip fault that has been termed the “southeast” fault in prior investigations may also represent a southern divide or barrier as postulated by Sanyal, et al. (2006).

The production wells were principally located on the basis of shallow temperature gradient borings and wells. While near surface temperatures may be higher in the areas previously identified as “anomalous” (the Humboldt House and Rye Patch anomaly areas), these areas may be more indicative of shallow outflow systems per scenario b) of Figure 8 and the low enthalpy zone of Ellis (2011).

As Michels (2002) suggests, the zone of higher pressure geothermal fluids at deeper depths is indicative of a reservoir confined by impermeable boundaries. This zone would be consistent with the medium enthalpy zone of Ellis (2011). The faulting and tilting of the fault blocks to the east could provide lateral structural barriers while the Paleogene volcanics and alluvium sealed by sinter and silica deposits could provide an upper cap. The sub-basins created by the tilting of the horst blocks would provide a reservoir for these fluids. Potential targets for both the low and medium enthalpy zones include the gravity lows located to the south of the sinter deposits, northeast of the existing plant, and near the southern end of the study area between the Rye Patch Fault and unnamed fault (Figure 35).

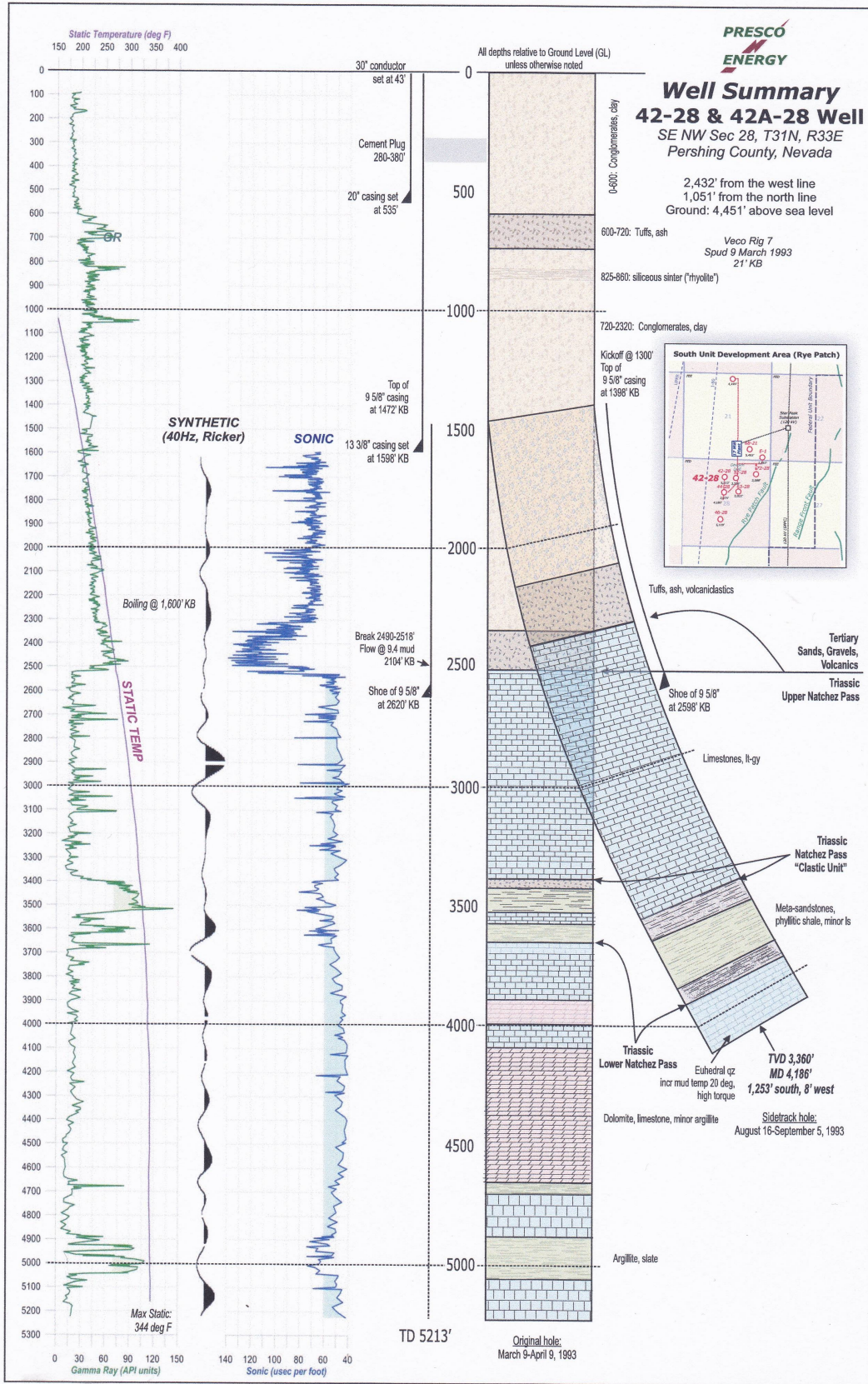
While the high enthalpy zone of Ellis (2011) may exist within the clastic unit of the Natchez Pass Formation, this target has been somewhat elusive as a drilling target. The high noise-to-signal ratios of seismic studies and the variable thickness and heterogeneous nature of this unit complicate the definition of its location. Geothermometry indicates that the temperature of the source of all of the hot fluids is above 200°C and is likely on the order of 250°C. Based on the temperature measurements from the existing wells and calculated temperature gradients, the depth of the common resource water would be on the order of 4 km, however higher temperature fluids may be at shallower depths due to convection and flow along more permeable layers such as the clastic unit of the Natchez Pass Formation.

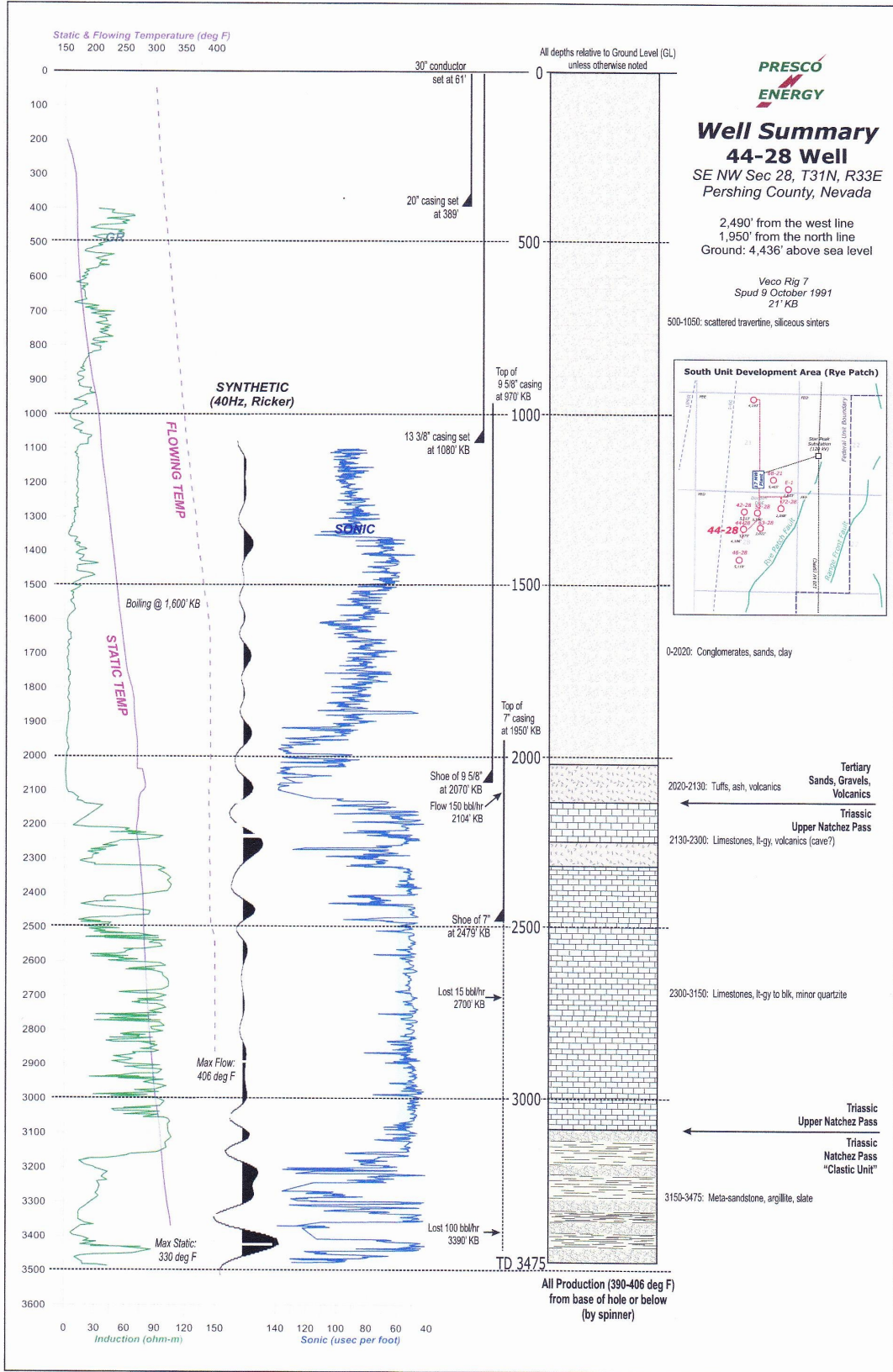
The Rye Patch Fault may again serve as a barrier and a structural trap could therefore be located to the west of the existing wells although it would necessitate

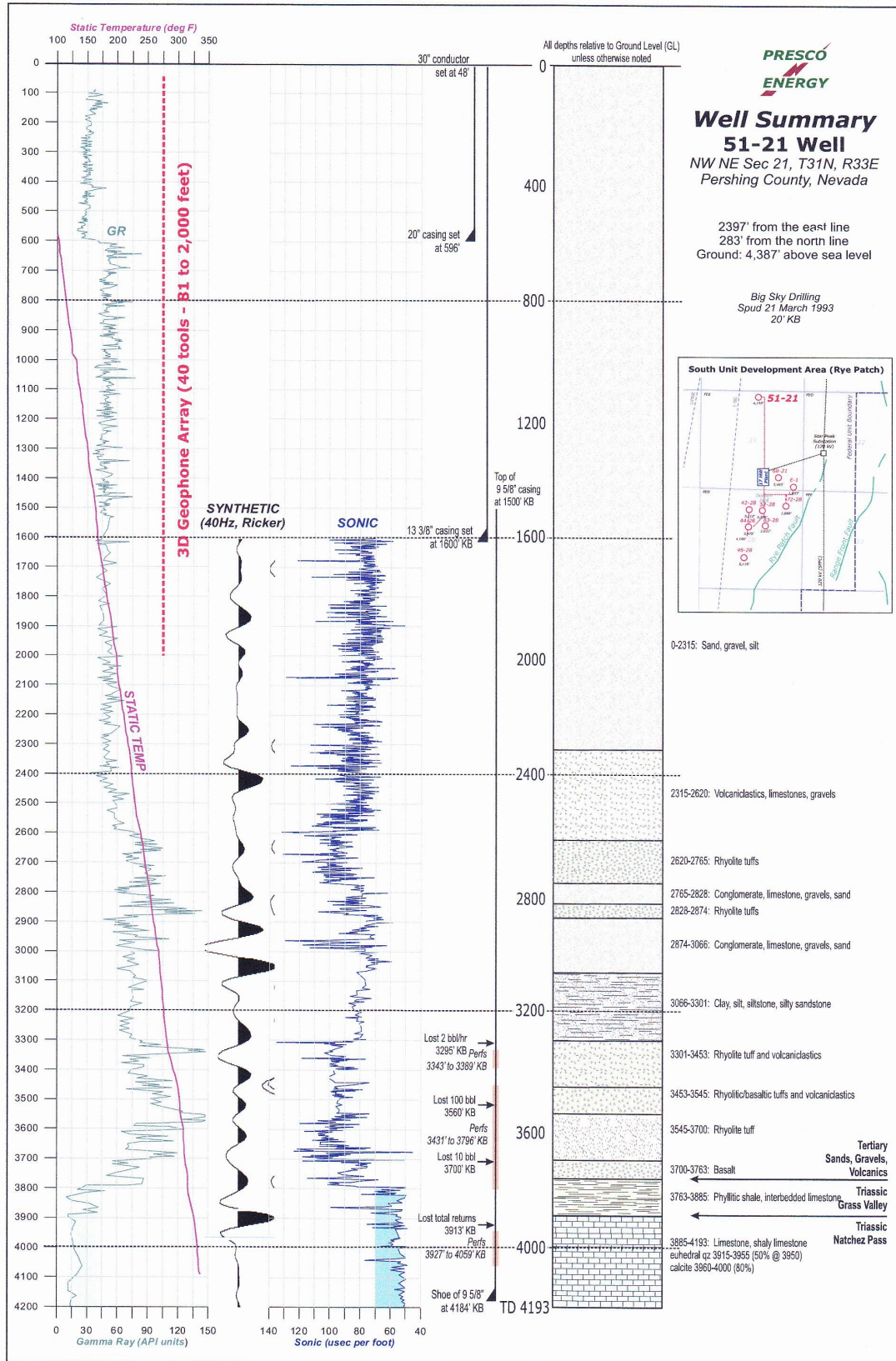
drilling to greater depths. However, if the blocks are tilted back to the east as indicated by the modeling and the geothermal fluids are flowing upward along the faults as postulated, they may be more likely to have entered the permeable Natchez Pass clastic unit in the down-dropped block prior to reaching the upper block. This, combined with the structural barrier noted above, indicates that the west side of the Rye Patch Fault may represent a drilling target for the high enthalpy zone.

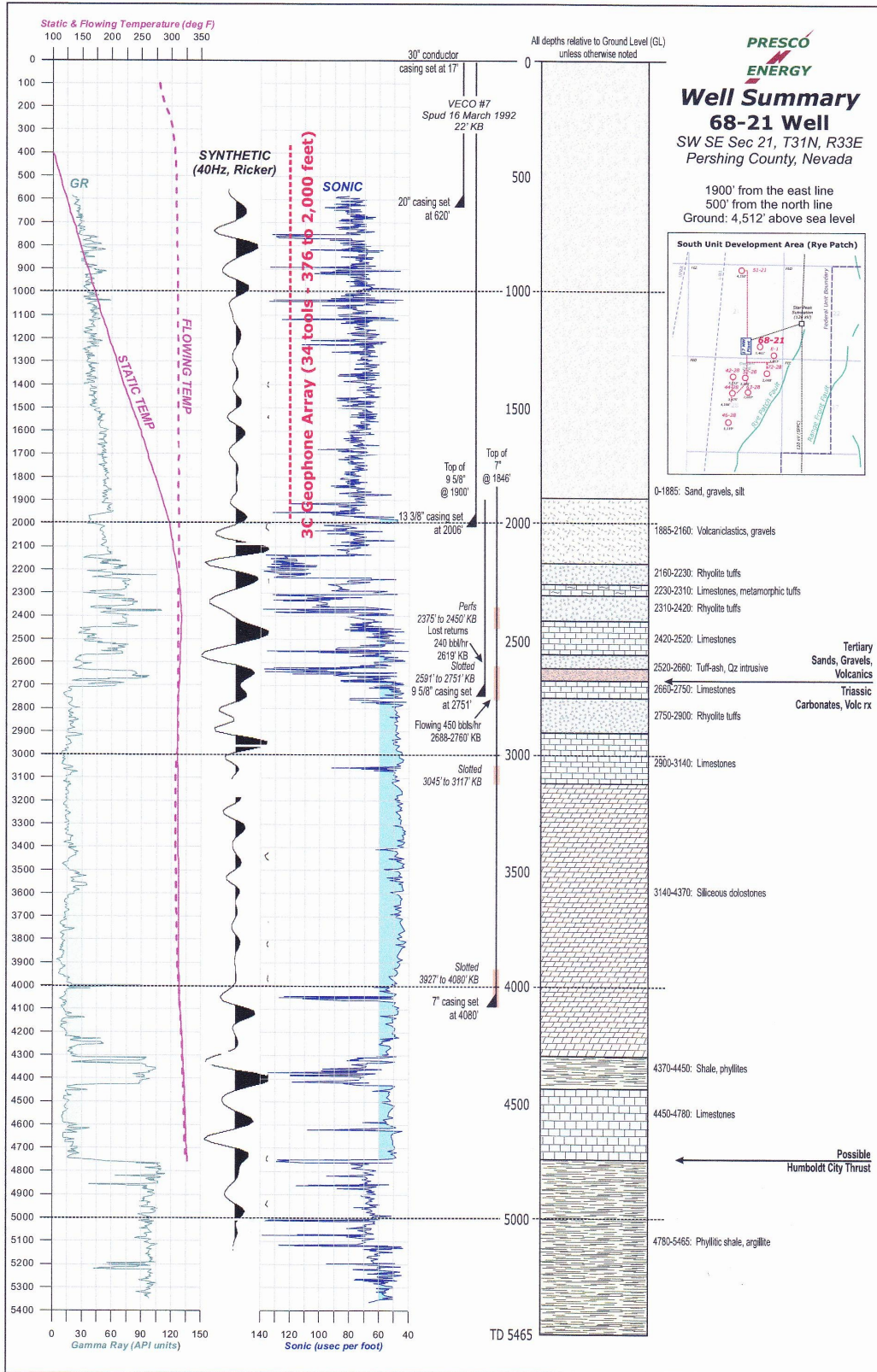
In conclusion, the results of the survey indicate that a gravity survey can be an effective method of defining approximate fault locations, lengths, and approximate trends and dip angles leading to the identification of potential geothermal drilling targets although the need for applying filtering techniques is evident. However, development of realistic models based on gravity would require sufficient constraining information from seismic surveys, well logs and other geological and geophysical information. The method could be utilized as a precursor to more expensive surveys such as seismic. This study shows that the method would provide an indication of the approximate location and geometry of features and of interest where additional work could be focused after which, it could be used as an aid in the development of conceptual models.

APPENDIX A
Well Logs









APPENDIX B
Station Location Data

Table 2. GPS Data

Project Information		Coordinate System	
Name:	D:\Dissertation\2012 Field\GPS\Process	Name:	Default
Size:	3 MB	Datum:	WGS 1984
Modified:	6/23/2012 8:19:09 AM (UTC:-5)	Zone:	Default
Time zone:	Central Standard Time	Geoid:	
Reference number:		Vertical datum:	
Description:			

Baseline Processing Report

Processing Summary

Observation	From	To	Solution Type	H. Prec.	V. Prec.	Geodetic	Ellipsoid	ΔHeight
BASE1 --- 25 (B15)	BASE1	25	Fixed	0.032	0.044	196°48'16"	10654.444	-1.130
BASE1 --- 4 (B14)	BASE1	4	Fixed	0.035	0.057	196°29'43"	10847.202	12.135
BASE1 --- 3 (B13)	BASE1	3	Fixed	0.014	0.029	197°28'49"	10907.084	0.168
BASE1 --- 46 (B11)	BASE1	46	Fixed	0.031	0.038	197°08'14"	10466.918	-4.747
BASE1 --- 67 (B10)	BASE1	67	Fixed	0.048	0.054	197°28'53"	10276.497	-4.311
BASE1 --- 88 (B9)	BASE1	88	Fixed	0.028	0.024	197°50'09"	10086.735	-6.304
BASE1 --- 107 (B8)	BASE1	107	Fixed	0.016	0.019	198°12'24"	9899.329	-7.984
BASE1 --- 114 (B7)	BASE1	114	Fixed	0.021	0.029	198°32'08"	9719.924	-9.518
BASE1 --- 115 (B6)	BASE1	115	Fixed	0.016	0.025	197°27'46"	9644.791	-5.104
BASE1 --- 108 (B5)	BASE1	108	Fixed	0.014	0.024	197°06'01"	9833.399	-4.125
BASE1 --- 89 (B4)	BASE1	89	Fixed	0.014	0.026	196°45'37"	10024.484	0.612
BASE1 --- 68 (B3)	BASE1	68	Fixed	0.015	0.026	196°24'37"	10215.921	1.308
BASE1 --- 47 (B2)	BASE1	47	Fixed	0.016	0.030	196°05'43"	10409.965	1.033
BASE1 --- 26 (B1)	BASE1	26	Fixed	0.017	0.025	195°46'20"	10598.429	12.908
FLCYNBASE --- 66	FLCYNBASE	66	Fixed	0.023	0.035	198°35'49"	10338.628	-11.881
166 (B56)	FLCYNBASE	166	Fixed	0.020	0.021	197°05'16"	8569.406	1.722
165 (B57)	FLCYNBASE	165	Fixed	0.018	0.020	198°15'20"	8631.002	-3.243
154 (B58)	FLCYNBASE	154	Fixed	0.015	0.021	198°55'04"	9085.827	-6.381
159 (B59)	FLCYNBASE	159	Fixed	0.014	0.021	199°06'59"	8897.948	-7.194
164 (B60)	FLCYNBASE	164	Fixed	0.013	0.022	199°33'06"	8693.536	-7.041
160 (B61)	FLCYNBASE	160	Fixed	0.014	0.027	197°49'33"	8820.399	-2.314
161 (B62)	FLCYNBASE	161	Fixed	0.015	0.026	196°40'32"	8754.654	2.754
162 (B63)	FLCYNBASE	162	Fixed	0.016	0.028	195°26'14"	8699.539	7.856
163 (B64)	FLCYNBASE	163	Fixed	0.016	0.025	194°10'03"	8650.157	12.081
158 (B65)	FLCYNBASE	158	Fixed	0.016	0.024	193°55'00"	8837.452	17.570
157 (B66)	FLCYNBASE	157	Fixed	0.019	0.027	194°58'14"	8887.172	12.632
156 (B67)	FLCYNBASE	156	Fixed	0.016	0.023	196°15'36"	8943.010	6.030
FLCYNBASE --- 45	FLCYNBASE	45	Fixed	0.020	0.030	198°26'57"	10533.512	-13.821
FLCYNBASE --- 44	FLCYNBASE	44	Fixed	0.018	0.026	199°12'07"	10592.630	-15.078
FLCYNBASE --- 23	FLCYNBASE	23	Fixed	0.017	0.024	198°50'47"	10783.777	-15.526
FLCYNBASE --- 2	FLCYNBASE	2	Fixed	0.059	0.042	198°28'39"	10976.390	-8.641

Table 2. (Cont.)

Observation	From	To	Solution Type	H. Prec.	V. Prec.	Geodetic	Ellipsoid	ΔHeight
FLCYNBASE --- 1	FLCYNBASE	1	Fixed	0.018	0.025	199°28'11"	11037.478	-16.215
FLCYNBASE --- 22	FLCYNBASE	22	Fixed	0.022	0.035	199°49'59"	10854.433	-16.686
FLCYNBASE --- 43	FLCYNBASE	43	Fixed	0.017	0.029	200°13'27"	10665.142	-16.854
FLCYNBASE --- 64	FLCYNBASE	64	Fixed	0.015	0.031	200°36'34"	10478.430	-17.209
FLCYNBASE --- 85	FLCYNBASE	85	Fixed	0.013	0.030	201°00'32"	10292.531	-17.997
FLCYNBASE --- 86	FLCYNBASE	86	Fixed	0.013	0.030	199°58'22"	10223.994	-15.549
FLCYNBASE --- 65	FLCYNBASE	65	Fixed	0.013	0.023	199°34'27"	10408.623	-15.398
FLCYNBASE --- 87	FLCYNBASE	87	Fixed	0.030	0.030	198°54'56"	10151.496	-12.407
FLCYNBASE --- 113	FLCYNBASE	113	Fixed	0.022	0.029	199°41'02"	9834.350	-18.590
FLCYNBASE --- 120	FLCYNBASE	120	Fixed	0.014	0.021	200°07'41"	9588.844	-14.993
FLCYNBASE --- 137	FLCYNBASE	137	Fixed	0.013	0.023	200°34'08"	9402.843	-15.603
FLCYNBASE --- 138	FLCYNBASE	138	Fixed	0.016	0.030	199°25'47"	9330.085	-11.313
FLCYNBASE --- 139	FLCYNBASE	139	Fixed	0.014	0.026	198°15'47"	9262.481	-5.242
FLCYNBASE --- 123	FLCYNBASE	123	Fixed	0.029	0.044	196°38'50"	9379.574	-0.285
FLCYNBASE --- 124	FLCYNBASE	124	Fixed	0.025	0.038	195°33'14"	9309.791	4.684
FLCYNBASE --- 117	FLCYNBASE	117	Fixed	0.017	0.025	195°11'24"	9523.993	11.096
FLCYNBASE --- 116	FLCYNBASE	116	Fixed	0.018	0.025	196°20'47"	9581.750	3.354
FLCYNBASE --- 178	FLCYNBASE	178	Fixed	0.018	0.022	200°01'51"	8508.544	-8.064
FLCYNBASE --- 197	FLCYNBASE	197	Fixed	0.020	0.024	201°01'37"	8134.473	-8.398
FLCYNBASE --- 198	FLCYNBASE	198	Fixed	0.020	0.029	199°45'31"	8068.469	-1.331
FLCYNBASE --- 199	FLCYNBASE	199	Fixed	0.017	0.025	198°17'42"	7994.424	5.628
FLCYNBASE --- 200	FLCYNBASE	200	Fixed	0.017	0.024	197°01'17"	7934.217	12.015
FLCYNBASE --- 196	FLCYNBASE	196	Fixed	0.017	0.023	195°14'36"	8069.805	17.193
FLCYNBASE --- 195	FLCYNBASE	195	Fixed	0.031	0.060	196°30'23"	8123.471	10.934
FLCYNBASE --- 194	FLCYNBASE	194	Fixed	0.018	0.039	197°53'51"	8191.865	4.484
FLCYNBASE --- 193	FLCYNBASE	193	Fixed	0.015	0.029	199°11'16"	8257.168	-2.070
FLCYNBASE --- 192	FLCYNBASE	192	Fixed	0.014	0.030	200°29'20"	8322.968	-8.843
FLCYNBASE --- 180	FLCYNBASE	180	Fixed	0.020	0.038	197°26'23"	8378.204	3.367
FLCYNBASE --- 181	FLCYNBASE	181	Fixed	0.014	0.022	196°11'24"	8310.079	9.637
FLCYNBASE --- 182	FLCYNBASE	182	Fixed	0.023	0.035	194°51'23"	8260.335	16.003
FLCYNBASE --- 167	FLCYNBASE	167	Fixed	0.019	0.021	195°44'42"	8506.807	7.328
FLCYNBASE --- 155	FLCYNBASE	155	Fixed	0.025	0.036	197°26'01"	9008.039	0.021
FLCYNBASE --- 111	FLCYNBASE	111	Fixed	0.058	0.084	194°06'21"	9665.797	19.638
FLCYNBASE --- 110	FLCYNBASE	110	Fixed	0.020	0.030	195°01'03"	9716.749	13.445
FLCYNBASE --- 109	FLCYNBASE	109	Fixed	0.019	0.027	195°59'38"	9775.790	5.654
FLCYNBASE --- 112	FLCYNBASE	112	Fixed	0.018	0.025	193°04'40"	9659.668	28.588
FLCYNBASE --- 140	FLCYNBASE	140	Fixed	0.019	0.026	197°05'44"	9200.209	0.058
FLCYNBASE --- 141	FLCYNBASE	141	Fixed	0.020	0.031	195°54'06"	9142.902	6.256
FLCYNBASE --- 142	FLCYNBASE	142	Fixed	0.017	0.028	194°41'31"	9085.905	13.644
FLCYNBASE --- 143	FLCYNBASE	143	Fixed	0.014	0.027	193°41'09"	9048.000	21.525
FLCYNBASE --- 126	FLCYNBASE	126	Fixed	0.014	0.032	193°29'42"	9231.312	25.070

Table 2. (Cont.)

Observation	From	To	Solution Type	H. Prec.	V. Prec.	Geodetic	Ellipsoid	ΔHeight
FLCYNBASE --- 118	FLCYNBASE	118	Fixed	0.015	0.032	194°14'45"	9474.076	19.791
FLCYNBASE --- 125	FLCYNBASE	125	Fixed	0.013	0.024	194°30'05"	9283.246	12.573
FLCYNBASE --- 92	FLCYNBASE	92	Fixed	0.027	0.022	193°28'19"	9855.224	23.308
FLCYNBASE --- 91	FLCYNBASE	91	Fixed	0.022	0.021	194°32'38"	9903.470	15.239
FLCYNBASE --- 90	FLCYNBASE	90	Fixed	0.018	0.020	195°38'07"	9965.546	7.618
FLCYNBASE --- 69	FLCYNBASE	69	Fixed	0.015	0.020	195°22'06"	10156.850	7.869
FLCYNBASE --- 71	FLCYNBASE	71	Fixed	0.025	0.042	193°10'04"	10051.883	23.200
BASE1 --- 24 (B12)	BASE1	24	Fixed	0.027	0.063	197°48'21"	10712.480	-8.065
FLCYNBASE --- 106	FLCYNBASE	106	Fixed	0.019	0.021	199°18'59"	9964.009	-14.163
FLCYNBASE --- 201	FLCYNBASE	201	Fixed	0.016	0.022	195°36'04"	7869.860	18.817
FLCYNBASE --- 179	FLCYNBASE	179	Fixed	0.013	0.027	198°42'04"	8451.667	-2.455
FLCYNBASE --- 168	FLCYNBASE	168	Fixed	0.018	0.021	194°23'33"	8443.100	13.956
FLCYNBASE --- 119	FLCYNBASE	119	Fixed	0.013	0.029	193°17'18"	9440.047	27.572
FLCYNBASE --- 70	FLCYNBASE	70	Fixed	0.014	0.022	194°16'56"	10099.459	14.883
FLCYNBASE --- 8	FLCYNBASE	8	Fixed	0.019	0.024	192°23'06"	10645.178	28.098
FLCYNBASE --- 29	FLCYNBASE	29	Fixed	0.019	0.023	192°34'58"	10449.841	26.394
FLCYNBASE --- 50	FLCYNBASE	50	Fixed	0.019	0.023	192°55'28"	10256.600	23.635
FLCYNBASE --- 49	FLCYNBASE	49	Fixed	0.020	0.028	193°56'32"	10291.738	17.806
FLCYNBASE --- 48	FLCYNBASE	48	Fixed	0.020	0.031	195°03'30"	10344.875	8.883
FLCYNBASE --- 27	FLCYNBASE	27	Fixed	0.018	0.027	194°44'45"	10540.091	21.378
FLCYNBASE --- 28	FLCYNBASE	28	Fixed	0.017	0.025	193°42'01"	10487.363	23.597
FLCYNBASE --- 7	FLCYNBASE	7	Fixed	0.017	0.025	193°21'55"	10669.952	24.762
FLCYNBASE --- 6	FLCYNBASE	6	Fixed	0.018	0.029	194°28'51"	10732.307	20.614
FLCYNBASE --- 5	FLCYNBASE	5	Fixed	0.022	0.040	195°27'22"	10788.262	17.486
FLCYNBASE --- 121	FLCYNBASE	121	Fixed	0.015	0.030	199°00'03"	9520.468	-10.468
FLCYNBASE --- 122	FLCYNBASE	122	Fixed	0.014	0.030	197°52'48"	9452.881	-5.121
FLCYNBASE --- 94	FLCYNBASE	94	Fixed	0.019	0.022	191°08'34"	9764.882	39.508
FLCYNBASE --- 95	FLCYNBASE	95	Fixed	0.022	0.022	190°01'11"	9729.772	49.419
FLCYNBASE --- 96	FLCYNBASE	96	Fixed	0.028	0.021	188°51'25"	9699.778	60.992
FLCYNBASE --- 97	FLCYNBASE	97	Fixed	0.021	0.021	187°42'24"	9648.994	69.936
FLCYNBASE --- 98	FLCYNBASE	98	Fixed	0.016	0.020	186°29'47"	9631.432	77.819
FLCYNBASE --- 99	FLCYNBASE	99	Fixed	0.015	0.021	185°21'32"	9610.343	83.804
FLCYNBASE --- 78	FLCYNBASE	78	Fixed	0.014	0.021	185°11'45"	9806.442	86.199
FLCYNBASE --- 77	FLCYNBASE	77	Fixed	0.010	0.018	186°17'49"	9829.900	77.174
FLCYNBASE --- 76	FLCYNBASE	76	Fixed	0.014	0.026	187°29'42"	9862.608	68.925
FLCYNBASE --- 75	FLCYNBASE	75	Fixed	0.015	0.027	188°43'22"	9879.440	57.681
FLCYNBASE --- 72	FLCYNBASE	72	Fixed	0.032	0.049	191°57'21"	10001.587	32.585
FLCYNBASE --- 51	FLCYNBASE	51	Fixed	0.019	0.026	191°42'00"	10201.297	35.247
FLCYNBASE --- 52	FLCYNBASE	52	Fixed	0.017	0.025	190°42'35"	10156.255	42.443
FLCYNBASE --- 53	FLCYNBASE	53	Fixed	0.017	0.024	189°34'17"	10127.551	51.300
FLCYNBASE --- 54	FLCYNBASE	54	Fixed	0.016	0.023	188°29'58"	10081.569	59.648

Table 2. (Cont.)

Observation	From	To	Solution Type	H. Prec.	V. Prec.	Geodetic	Ellipsoid	ΔHeight
FLCYNBASE --- 55	FLCYNBASE	55	Fixed	0.016	0.023	187°20'46"	10044.308	68.440
FLCYNBASE --- 56	FLCYNBASE	56	Fixed	0.019	0.029	186°17'14"	10023.575	76.989
FLCYNBASE --- 57	FLCYNBASE	57	Fixed	0.027	0.041	185°07'36"	10003.694	86.556
FLCYNBASE --- 73	FLCYNBASE	73	Fixed	0.023	0.035	190°57'31"	9971.158	40.275
FLCYNBASE --- 93	FLCYNBASE	93	Fixed	0.042	0.075	192°05'05"	9839.078	31.848
FLCYNBASE --- 74	FLCYNBASE	74	Fixed	0.016	0.027	189°48'58"	9924.337	49.904
FLCYNBASE --- 81	FLCYNBASE	81	Fixed	0.016	0.022	181°42'13"	9764.193	115.247
36 (B130)	FLCYNBASE	36	Fixed	0.019	0.022	184°56'01"	10198.257	88.087
35 (B131)	FLCYNBASE	35	Fixed	0.019	0.023	186°03'58"	10225.867	77.700
34 (B132)	FLCYNBASE	34	Fixed	0.019	0.024	187°09'31"	10260.562	68.901
33 (B133)	FLCYNBASE	33	Fixed	0.016	0.023	188°12'58"	10281.428	60.824
32 (B134)	FLCYNBASE	32	Fixed	0.019	0.027	189°22'36"	10327.941	51.583
31 (B135)	FLCYNBASE	31	Fixed	0.017	0.026	190°25'24"	10344.592	43.922
30 (B136)	FLCYNBASE	30	Fixed	0.017	0.023	191°30'18"	10404.795	35.054
9 (B137)	FLCYNBASE	9	Fixed	0.018	0.023	191°20'10"	10577.782	34.190
10 (B138)	FLCYNBASE	10	Fixed	0.019	0.025	190°17'04"	10544.920	42.113
11 (B139)	FLCYNBASE	11	Fixed	0.023	0.036	189°12'40"	10521.501	51.068
12 (B140)	FLCYNBASE	12	Fixed	0.017	0.029	188°11'49"	10483.459	59.926
13 (B141)	FLCYNBASE	13	Fixed	0.015	0.028	187°05'36"	10454.079	68.560
14 (B142)	FLCYNBASE	14	Fixed	0.014	0.030	186°00'06"	10436.440	78.583
15 (B143)	FLCYNBASE	15	Fixed	0.013	0.030	184°53'52"	10407.696	88.835
100 (B144)	FLCYNBASE	100	Fixed	0.013	0.023	184°05'47"	9590.285	93.996
101 (B145)	FLCYNBASE	101	Fixed	0.014	0.022	182°57'47"	9569.028	103.677
102 (B146)	FLCYNBASE	102	Fixed	0.016	0.021	181°44'29"	9564.682	114.890
103 (B147)	FLCYNBASE	103	Fixed	0.023	0.022	180°32'37"	9559.727	126.301
104 (B148)	FLCYNBASE	104	Fixed	0.020	0.020	179°41'46"	9568.540	134.946
83 (B149)	FLCYNBASE	83	Fixed	0.023	0.025	179°43'30"	9767.659	136.923
82 (B150)	FLCYNBASE	82	Fixed	0.016	0.019	180°33'26"	9753.687	127.214
FLCYNBASE --- 80	FLCYNBASE	80	Fixed	0.021	0.033	182°51'37"	9777.556	104.644
FLCYNBASE --- 16	FLCYNBASE	16	Fixed	0.018	0.028	183°45'07"	10396.217	100.075
FLCYNBASE --- 208	FLCYNBASE	208	Fixed	0.016	0.023	192°02'31"	7327.804	48.702
FLCYNBASE --- 209	FLCYNBASE	209	Fixed	0.017	0.025	190°26'28"	7298.027	56.503
FLCYNBASE --- 210	FLCYNBASE	210	Fixed	0.023	0.034	188°52'56"	7263.274	65.030
FLCYNBASE --- 211	FLCYNBASE	211	Fixed	0.023	0.034	187°15'55"	7224.652	84.103
FLCYNBASE --- 79	FLCYNBASE	79	Fixed	0.015	0.026	184°02'18"	9791.422	94.956
FLCYNBASE --- 58	FLCYNBASE	58	Fixed	0.014	0.027	183°57'11"	9996.969	96.528
250 (B228)	FLCYNBASE	250	Fixed	0.009	0.019	284°30'21"	1687.404	-32.930
245 (B229)	FLCYNBASE	245	Fixed	0.011	0.015	267°02'25"	2031.171	-35.538
244 (B230)	FLCYNBASE	244	Fixed	0.010	0.012	270°15'29"	2425.411	-38.922
243 (B231)	FLCYNBASE	243	Fixed	0.015	0.016	270°09'58"	2825.067	-39.445
247 (B232)	FLCYNBASE	247	Fixed	0.019	0.022	278°08'14"	2860.241	-40.109

Table 2. (Cont.)

Observation	From	To	Solution Type	H. Prec.	V. Prec.	Geodetic	Ellipsoid	ΔHeight
248 (B233)	FLCYNBASE	248	Fixed	0.011	0.014	279°33'46"	2471.523	-38.968
FLCYNBASE --- 212	FLCYNBASE	212	Fixed	0.018	0.022	185°51'34"	7198.739	86.478
FLCYNBASE --- 214	FLCYNBASE	214	Fixed	0.020	0.029	182°39'14"	7171.483	106.721
FLCYNBASE --- 207	FLCYNBASE	207	Fixed	0.018	0.027	182°26'24"	7359.104	101.282
FLCYNBASE --- 206	FLCYNBASE	206	Fixed	0.017	0.025	184°05'49"	7381.653	91.895
FLCYNBASE --- 205	FLCYNBASE	205	Fixed	0.016	0.023	185°37'49"	7387.753	81.068
FLCYNBASE --- 204	FLCYNBASE	204	Fixed	0.016	0.022	187°04'41"	7422.112	74.826
FLCYNBASE --- 202	FLCYNBASE	202	Fixed	0.029	0.044	190°07'38"	7494.018	49.829
FLCYNBASE --- 183	FLCYNBASE	183	Fixed	0.014	0.026	192°11'49"	8161.410	30.632
FLCYNBASE --- 184	FLCYNBASE	184	Fixed	0.013	0.028	190°42'08"	8121.337	39.297
FLCYNBASE --- 185	FLCYNBASE	185	Fixed	0.013	0.028	189°23'31"	8080.317	51.915
FLCYNBASE --- 186	FLCYNBASE	186	Fixed	0.012	0.027	188°00'36"	8043.525	60.409
FLCYNBASE --- 187	FLCYNBASE	187	Fixed	0.014	0.024	186°34'21"	8024.108	68.756
FLCYNBASE --- 189	FLCYNBASE	189	Fixed	0.027	0.036	183°44'48"	7970.285	89.948
FLCYNBASE --- 190	FLCYNBASE	190	Fixed	0.019	0.021	182°19'26"	7965.847	101.412
FLCYNBASE --- 191	FLCYNBASE	191	Fixed	0.022	0.021	180°44'13"	7967.878	116.479
FLCYNBASE --- 177	FLCYNBASE	177	Fixed	0.022	0.021	180°47'24"	8178.993	115.894
FLCYNBASE --- 176	FLCYNBASE	176	Fixed	0.018	0.020	182°08'51"	8163.604	103.786
FLCYNBASE --- 175	FLCYNBASE	175	Fixed	0.019	0.026	183°30'42"	8190.840	94.910
FLCYNBASE --- 174	FLCYNBASE	174	Fixed	0.016	0.023	184°55'20"	8187.255	88.077
FLCYNBASE --- 173	FLCYNBASE	173	Fixed	0.013	0.022	186°20'48"	8214.280	74.598
FLCYNBASE --- 172	FLCYNBASE	172	Fixed	0.014	0.025	187°49'57"	8252.597	59.487
FLCYNBASE --- 171	FLCYNBASE	171	Fixed	0.019	0.036	189°02'11"	8276.656	51.720
FLCYNBASE --- 170	FLCYNBASE	170	Fixed	0.023	0.041	190°27'29"	8304.834	35.022
FLCYNBASE --- 169	FLCYNBASE	169	Fixed	0.026	0.044	191°51'37"	8355.236	26.118
FLCYNBASE --- 150	FLCYNBASE	150	Fixed	0.018	0.027	184°30'59"	8788.924	90.268
FLCYNBASE --- 149	FLCYNBASE	149	Fixed	0.022	0.041	185°49'42"	8820.082	83.357
FLCYNBASE --- 148	FLCYNBASE	148	Fixed	0.018	0.032	187°17'38"	8824.786	69.293
FLCYNBASE --- 147	FLCYNBASE	147	Fixed	0.025	0.043	188°25'26"	8862.399	63.028
FLCYNBASE --- 145	FLCYNBASE	145	Fixed	0.015	0.021	190°59'35"	8879.121	42.675
FLCYNBASE --- 144	FLCYNBASE	144	Fixed	0.029	0.032	192°10'06"	9002.150	33.382
FLCYNBASE --- 146	FLCYNBASE	146	Fixed	0.020	0.029	189°39'37"	8882.133	51.428
FLCYNBASE --- 188	FLCYNBASE	188	Fixed	0.014	0.022	185°11'17"	8003.842	79.120
FLCYNBASE --- 151	FLCYNBASE	151	Fixed	0.018	0.026	183°18'17"	8777.241	97.242
FLCYNBASE --- 213	FLCYNBASE	213	Fixed	0.027	0.033	184°14'27"	7182.244	97.434
FLCYNBASE --- 203	FLCYNBASE	203	Fixed	0.017	0.022	188°38'22"	7460.163	63.386
FLCYNBASE --- 127	FLCYNBASE	127	Fixed	0.020	0.022	191°54'27"	9171.201	39.218
133 (B198)	FLCYNBASE	133	Fixed	0.021	0.024	184°28'21"	8993.190	90.474
134 (B199)	FLCYNBASE	134	Fixed	0.018	0.025	183°12'52"	8982.051	100.001
135 (B200)	FLCYNBASE	135	Fixed	0.022	0.035	181°58'10"	8975.997	110.081
136 (B201)	FLCYNBASE	136	Fixed	0.017	0.028	180°41'48"	8955.339	123.406

Table 2. (Cont.)

Observation	From	To	Solution Type	H. Prec.	V. Prec.	Geodetic	Ellipsoid	ΔHeight
153 (B202)	FLCYNBASE	153	Fixed	0.015	0.030	180°38'48"	8764.716	123.785
152 (B203)	FLCYNBASE	152	Fixed	0.013	0.030	181°54'52"	8766.665	110.383
215 (B204)	FLCYNBASE	215	Fixed	0.011	0.019	197°25'35"	3944.240	33.622
216 (B205)	FLCYNBASE	216	Fixed	0.013	0.019	191°45'34"	3840.768	56.398
219 (B206)	FLCYNBASE	219	Fixed	0.013	0.016	186°24'51"	3380.334	82.382
222 (B207)	FLCYNBASE	222	Fixed	0.013	0.015	188°37'49"	2998.144	62.789
225 (B208)	FLCYNBASE	225	Fixed	0.012	0.014	188°30'28"	2585.988	58.509
224 (B209)	FLCYNBASE	224	Fixed	0.012	0.013	197°13'39"	2671.551	36.458
223 (B193)	FLCYNBASE	223	Fixed	0.008	0.012	204°53'51"	2832.143	16.463
217 (B194)	FLCYNBASE	217	Fixed	0.009	0.016	199°18'02"	3577.504	30.450
218 (B195)	FLCYNBASE	218	Fixed	0.017	0.031	193°03'23"	3450.704	53.803
220 (B196)	FLCYNBASE	220	Fixed	0.010	0.018	201°48'01"	3202.398	24.911
221 (B197)	FLCYNBASE	221	Fixed	0.011	0.019	194°47'08"	3069.558	44.107
FLCYNBASE --- 128	FLCYNBASE	128	Fixed	0.019	0.024	190°43'54"	9141.169	48.342
FLCYNBASE --- 129	FLCYNBASE	129	Fixed	0.022	0.028	189°30'26"	9108.353	58.370
FLCYNBASE --- 130	FLCYNBASE	130	Fixed	0.021	0.031	188°16'23"	9056.860	65.259
FLCYNBASE --- 131	FLCYNBASE	131	Fixed	0.019	0.028	187°02'01"	9034.401	76.296
FLCYNBASE --- 132	FLCYNBASE	132	Fixed	0.017	0.025	185°45'02"	9011.957	83.034
FLCYNBASE --- 229	FLCYNBASE	229	Fixed	0.014	0.022	236°34'51"	2881.536	-27.613
FLCYNBASE --- 230	FLCYNBASE	230	Fixed	0.011	0.017	231°56'13"	2558.352	-19.925
FLCYNBASE --- 227	FLCYNBASE	227	Fixed	0.011	0.015	230°37'22"	3130.797	-25.387
FLCYNBASE --- 226	FLCYNBASE	226	Fixed	0.017	0.025	234°36'16"	3430.978	-29.728
FLCYNBASE --- 231	FLCYNBASE	231	Fixed	0.009	0.014	247°06'11"	3047.992	-34.520
FLCYNBASE --- 232	FLCYNBASE	232	Fixed	0.010	0.015	243°54'58"	2687.078	-31.789
FLCYNBASE --- 228	FLCYNBASE	228	Fixed	0.010	0.015	240°20'44"	3222.902	-31.864
268 (B234)	FLCYNBASE	268	Fixed	0.011	0.021	332°36'28"	1839.305	-32.507
274 (B235)	FLCYNBASE	274	Fixed	0.011	0.018	337°07'31"	2204.165	-35.234
280 (B236)	FLCYNBASE	280	Fixed	0.013	0.020	340°33'09"	2580.382	-37.111
279 (B237)	FLCYNBASE	279	Fixed	0.023	0.034	332°39'05"	2737.564	-40.310
273 (B238)	FLCYNBASE	273	Fixed	0.010	0.015	328°16'59"	2390.881	-36.213
267 (B239)	FLCYNBASE	267	Fixed	0.009	0.012	322°28'25"	2074.697	-29.946
251 (B240)	FLCYNBASE	251	Fixed	0.010	0.015	285°52'44"	2952.094	-38.681
252 (B241)	FLCYNBASE	252	Fixed	0.009	0.014	288°36'25"	2567.405	-34.351
253 (B242)	FLCYNBASE	253	Fixed	0.008	0.013	291°48'51"	2207.110	-35.650
254 (B243)	FLCYNBASE	254	Fixed	0.008	0.012	297°28'49"	1836.816	-34.256
255 (B244)	FLCYNBASE	255	Fixed	0.006	0.009	303°28'37"	1502.217	-29.440
256 (B245)	FLCYNBASE	256	Fixed	0.006	0.009	314°22'49"	1190.928	-27.470
262 (B246)	FLCYNBASE	262	Fixed	0.007	0.011	325°20'07"	1492.343	-31.416
261 (B247)	FLCYNBASE	261	Fixed	0.011	0.018	314°18'46"	1741.725	-31.490
260 (B248)	FLCYNBASE	260	Fixed	0.017	0.033	306°45'48"	2053.218	-35.015
259 (B249)	FLCYNBASE	259	Fixed	0.008	0.016	299°48'24"	2392.607	-36.264

Table 2. (Cont.)

Observation	From	To	Solution Type	H. Prec.	V. Prec.	Geodetic	Ellipsoid	ΔHeight
FLCYNBASE --- 233	FLCYNBASE	233	Fixed	0.020	0.025	239°39'00"	2333.794	-24.640
FLCYNBASE --- 238	FLCYNBASE	238	Fixed	0.024	0.034	244°18'43"	1797.262	-21.074
FLCYNBASE --- 237	FLCYNBASE	237	Fixed	0.014	0.021	248°59'07"	2158.961	-29.146
FLCYNBASE --- 236	FLCYNBASE	236	Fixed	0.010	0.015	251°45'17"	2538.178	-34.701
FLCYNBASE --- 239	FLCYNBASE	239	Fixed	0.011	0.019	262°03'35"	2859.511	-38.988
FLCYNBASE --- 240	FLCYNBASE	240	Fixed	0.017	0.035	260°58'16"	2458.599	-36.830
FLCYNBASE --- 242	FLCYNBASE	242	Fixed	0.006	0.014	256°58'14"	1667.131	-24.773
FLCYNBASE --- 246	FLCYNBASE	246	Fixed	0.007	0.014	270°48'47"	1624.339	-29.881
FLCYNBASE --- 17	FLCYNBASE	17	Fixed	0.016	0.026	182°35'56"	10362.373	111.857
FLCYNBASE --- 234	FLCYNBASE	234	Fixed	0.013	0.015	233°50'53"	1999.052	-14.542
FLCYNBASE --- 241	FLCYNBASE	241	Fixed	0.010	0.022	259°25'10"	2067.679	-32.905
FLCYNBASE --- 257	FLCYNBASE	257	Fixed	0.012	0.015	292°59'42"	3084.676	-39.128
FLCYNBASE --- 263	FLCYNBASE	263	Fixed	0.012	0.014	299°24'55"	3271.274	-40.945
FLCYNBASE --- 264	FLCYNBASE	264	Fixed	0.012	0.017	303°19'55"	2935.250	-39.936
FLCYNBASE --- 265	FLCYNBASE	265	Fixed	0.016	0.025	308°16'29"	2609.919	-36.039
FLCYNBASE --- 266	FLCYNBASE	266	Fixed	0.014	0.023	314°31'22"	2316.243	-35.500
FLCYNBASE --- 272	FLCYNBASE	272	Fixed	0.023	0.041	320°43'25"	2617.817	-35.781
FLCYNBASE --- 278	FLCYNBASE	278	Fixed	0.008	0.017	325°39'03"	2939.437	-41.079
FLCYNBASE --- 277	FLCYNBASE	277	Fixed	0.008	0.017	319°37'17"	3179.132	-41.149
FLCYNBASE --- 271	FLCYNBASE	271	Fixed	0.013	0.024	314°37'55"	2885.144	-34.093
FLCYNBASE --- 270	FLCYNBASE	270	Fixed	0.012	0.017	309°24'34"	3174.199	-39.754
FLCYNBASE --- 276	FLCYNBASE	276	Fixed	0.026	0.033	314°26'08"	3445.082	-43.414
FLCYNBASE --- 269	FLCYNBASE	269	Fixed	0.015	0.015	305°03'52"	3488.578	-44.076
FLCYNBASE --- 258	FLCYNBASE	258	Fixed	0.016	0.017	296°17'25"	2736.367	-34.839
FLCYNBASE --- 275	FLCYNBASE	275	Fixed	0.026	0.028	310°04'36"	3738.128	-42.780
FLCYNBASE --- 249	FLCYNBASE	249	Fixed	0.012	0.015	282°04'06"	2076.093	-35.558
FLCYNBASE --- 235	FLCYNBASE	235	Fixed	0.010	0.015	254°19'14"	2925.365	-37.259

APPENDIX C
Gravity Data

Table 3. Gravity Data

Station	Easting (m)	Northing (m)	Elevation (m)	Free Air Anomaly (mGal)	Simple Bouguer Anomaly rho = 2.67 (mGal)	Terrain Correction (mGal)	Complete Bouguer Anomaly (mGal)
1	389800.90	4483202.71	1289.35	-72.05	-215.23	2.09	-213.14
2	390000.91	4483195.61	1296.92	-71.11	-215.14	1.58	-213.56
3	390201.13	4483201.94	1305.59	-69.89	-214.89	1.26	-213.63
4	390397.45	4483201.77	1317.55	-69.15	-215.50	1.01	-214.49
5	390604.75	4483199.63	1323.03	-69.08	-216.04	1.43	-214.61
6	390796.15	4483203.65	1326.15	-68.72	-216.04	2.09	-213.95
7	391013.45	4483210.94	1330.28	-68.21	-216.00	2.11	-213.89
8	391196.45	4483191.85	1333.62	-67.52	-215.68	2.32	-213.36
9	391399.54	4483214.12	1339.66	-66.26	-215.10	2.49	-212.61
10	391596.00	4483207.25	1347.56	-64.82	-214.55	2.53	-212.02
11	391794.21	4483194.11	1356.52	-62.77	-213.51	2.54	-210.97
12	391983.76	4483200.88	1365.36	-58.33	-210.06	2.54	-207.52
13	392187.47	4483200.27	1373.98	-57.58	-210.29	2.67	-207.63
14	392387.06	4483192.25	1384.00	-54.98	-208.82	2.67	-206.14
15	392589.73	4483198.91	1394.24	-52.64	-207.63	2.82	-204.81
16	392797.92	4483191.70	1405.52	-50.55	-206.81	2.83	-203.98
17	393008.58	4483210.90	1417.30	-48.45	-206.03	2.93	-203.10
18	393008.58	4483210.90	1417.30	-50.16	-207.75	2.93	-204.82
22	389799.91	4483398.41	1288.87	-71.80	-214.92	2.03	-212.89
23	389999.08	4483400.52	1290.01	-71.03	-214.27	2.19	-212.08
24	390204.50	4483405.92	1297.33	-69.86	-213.93	1.87	-212.06
25	390399.99	4483403.00	1304.29	-69.90	-214.76	1.79	-212.97
26	390599.36	4483400.23	1318.35	-68.74	-215.18	1.18	-214.01
27	390799.88	4483401.95	1326.93	-68.35	-215.76	1.14	-214.62
28	390998.78	4483403.10	1329.12	-67.88	-215.54	1.53	-214.01
29	391205.94	4483390.27	1331.91	-66.19	-214.16	2.09	-212.07
30	391405.97	4483389.69	1340.52	-65.84	-214.78	2.37	-212.41
31	391609.95	4483408.63	1349.38	-64.40	-214.33	2.39	-211.95
32	391798.50	4483389.89	1357.03	-62.69	-213.49	2.44	-211.04
33	392012.04	4483400.89	1366.26	-60.05	-211.89	2.56	-209.33
34	392202.54	4483393.49	1374.32	-57.49	-210.23	2.63	-207.61
35	392400.66	4483402.64	1383.12	-54.91	-208.65	2.79	-205.85
36	392604.24	4483407.88	1393.49	-52.52	-207.43	2.87	-204.56
43	389798.58	4483601.40	1288.68	-71.53	-214.63	1.99	-212.65
44	390001.55	4483602.79	1290.46	-70.28	-213.58	2.07	-211.51
45	390152.11	4483611.80	1291.70	-69.73	-213.17	2.19	-210.98
46	390398.86	4483600.24	1300.64	-69.34	-213.79	2.13	-211.66
47	390596.99	4483597.71	1306.48	-69.06	-214.17	2.21	-211.96
48	390797.92	4483605.26	1314.43	-68.99	-214.99	2.11	-212.89
49	391005.78	4483603.42	1323.33	-68.01	-215.01	2.01	-213.00
50	391191.28	4483592.55	1329.17	-67.24	-214.91	2.19	-212.72
51	391416.63	4483596.76	1340.78	-65.80	-214.77	2.31	-212.46
52	391598.03	4483604.17	1347.96	-64.72	-214.49	2.32	-212.17

Table 3. (Cont.)

Station	Easting (m)	Northing (m)	Elevation (m)	Free Air Anomaly (mGal)	Simple Bouguer Anomaly rho = 2.67 (mGal)	Terrain Correction (mGal)	Complete Bouguer Anomaly (mGal)
53	391801.30	4483594.05	1356.79	-62.89	-213.66	2.37	-211.28
54	391995.36	4483607.00	1365.12	-60.54	-212.25	2.46	-209.79
55	392201.17	4483613.06	1373.92	-57.76	-210.46	2.69	-207.77
56	392387.66	4483608.97	1382.41	-55.21	-208.87	2.78	-206.09
57	392591.38	4483605.68	1392.00	-52.73	-207.47	2.86	-204.62
58	392794.72	4483592.43	1401.95	-50.65	-206.51	3.00	-203.50
64	389799.94	4483801.13	1288.28	-71.24	-214.29	1.96	-212.33
65	390001.10	4483798.99	1290.09	-70.01	-213.27	2.04	-211.23
66	390191.24	4483804.56	1293.64	-68.94	-212.60	1.98	-210.62
67	390398.91	4483800.55	1301.06	-68.64	-213.13	2.08	-211.06
68	390599.72	4483799.81	1306.72	-68.52	-213.65	2.23	-211.42
69	390795.81	4483800.84	1313.47	-69.50	-215.40	2.41	-212.99
70	390996.13	4483804.33	1320.48	-69.04	-215.73	2.47	-213.26
71	391197.74	4483801.17	1328.80	-67.72	-215.35	2.52	-212.82
72	391416.37	4483801.46	1338.08	-65.76	-214.43	2.69	-211.74
73	391592.60	4483794.24	1345.79	-64.76	-214.29	2.59	-211.70
74	391796.23	4483801.62	1355.36	-63.06	-213.67	2.66	-211.01
75	391990.10	4483812.73	1363.17	-60.90	-212.39	3.00	-209.39
76	392201.58	4483796.55	1374.39	-57.71	-210.47	3.00	-207.47
77	392409.95	4483801.33	1382.63	-54.90	-208.58	3.10	-205.49
78	392600.01	4483803.06	1391.65	-52.61	-207.30	2.97	-204.33
79	392797.32	4483798.43	1400.40	-50.68	-206.36	3.19	-203.17
80	392998.90	4483797.30	1410.08	-49.00	-205.78	3.24	-202.53
81	393196.54	4483799.98	1420.65	-47.21	-205.17	3.46	-201.71
82	393391.98	4483803.85	1432.56	-44.62	-203.92	3.59	-200.33
83	393533.50	4483787.52	1442.26	-44.32	-204.72	3.69	-201.02
85	389801.13	4484000.56	1287.50	-71.28	-214.25	1.89	-212.36
86	389998.83	4483997.00	1289.92	-69.90	-213.15	1.79	-211.36
87	390200.22	4483999.93	1293.17	-68.55	-212.15	1.94	-210.21
88	390399.26	4484000.46	1299.10	-67.89	-212.16	2.09	-210.07
89	390597.98	4484000.92	1306.00	-67.98	-213.03	2.07	-210.96
90	390804.57	4483997.56	1313.22	-68.91	-214.78	2.11	-212.67
91	391003.53	4484005.39	1320.83	-68.59	-215.31	2.34	-212.97
92	391194.48	4484004.74	1328.89	-67.87	-215.50	2.41	-213.10
93	391430.67	4483964.81	1337.37	-65.52	-214.11	2.80	-211.30
94	391603.98	4484002.58	1344.99	-64.86	-214.31	2.71	-211.60
95	391798.18	4483999.22	1354.90	-63.30	-213.86	2.74	-211.12
96	391997.45	4483993.63	1366.47	-60.85	-212.71	2.61	-210.10
97	392197.20	4484013.08	1375.39	-57.97	-210.84	2.62	-208.22
98	392401.27	4484002.42	1383.26	-55.09	-208.85	2.78	-206.07
99	392593.39	4484000.94	1389.23	-53.01	-207.44	3.21	-204.23
100	392804.63	4483999.63	1399.37	-50.81	-206.37	3.26	-203.11
101	392995.14	4484006.46	1409.04	-49.14	-205.80	3.29	-202.51

Table 3. (Cont.)

Station	Easting (m)	Northing (m)	Elevation (m)	Free Air Anomaly (mGal)	Simple Bouguer Anomaly rho = 2.67 (mGal)	Terrain Correction (mGal)	Complete Bouguer Anomaly (mGal)
102	393198.98	4483999.53	1420.24	-47.32	-205.24	3.32	-201.91
103	393398.88	4483997.65	1431.63	-45.67	-204.87	3.38	-201.49
104	393540.17	4483986.53	1440.27	-44.49	-204.66	3.36	-201.30
106	390198.00	4484200.11	1291.38	-68.41	-211.82	1.71	-210.11
107	390398.56	4484198.65	1297.40	-65.58	-209.67	1.91	-207.75
108	390600.13	4484200.83	1301.26	-66.71	-211.23	2.37	-208.86
109	390799.70	4484197.00	1311.25	-67.71	-213.35	2.09	-211.26
110	390975.63	4484206.99	1319.03	-67.46	-213.99	2.05	-211.94
111	391137.81	4484215.17	1325.30	-67.38	-214.60	2.13	-212.47
112	391307.19	4484178.02	1334.16	-66.30	-214.53	2.52	-212.01
113	390183.50	4484343.72	1286.95	-68.86	-211.77	2.30	-209.46
114	390404.35	4484386.55	1295.89	-66.09	-210.00	2.12	-207.88
115	390600.12	4484399.19	1300.27	-65.27	-209.68	2.32	-207.36
116	390800.01	4484400.16	1308.86	-65.54	-210.91	2.12	-208.79
117	391001.20	4484400.49	1316.57	-66.64	-212.89	1.94	-210.94
118	391164.82	4484406.40	1325.36	-66.98	-214.21	1.68	-212.53
119	391326.28	4484399.55	1333.14	-66.41	-214.52	2.00	-212.52
120	390199.92	4484599.90	1290.51	-67.41	-210.72	1.89	-208.83
121	390400.07	4484598.71	1295.06	-66.73	-210.55	2.00	-208.55
122	390597.53	4484601.30	1300.40	-65.21	-209.63	2.31	-207.32
123	390812.63	4484607.93	1305.19	-64.50	-209.46	2.54	-206.92
124	391003.49	4484622.80	1310.17	-64.56	-210.09	2.65	-207.43
125	391174.42	4484601.48	1318.15	-66.46	-212.88	2.50	-210.38
126	391344.86	4484610.11	1330.63	-65.57	-213.40	2.01	-211.39
127	391606.19	4484608.76	1344.73	-63.79	-213.21	1.96	-211.24
128	391796.16	4484598.62	1353.84	-62.65	-213.09	2.12	-210.97
129	391993.80	4484593.84	1363.84	-61.18	-212.75	2.38	-210.37
130	392195.24	4484611.62	1370.72	-59.38	-211.72	2.41	-209.32
131	392392.04	4484605.00	1381.76	-56.18	-209.76	2.42	-207.34
132	392595.29	4484601.91	1388.49	-53.62	-207.96	2.73	-205.24
133	392797.39	4484600.05	1395.96	-51.67	-206.85	3.21	-203.64
134	392994.97	4484595.11	1405.47	-49.81	-206.07	3.14	-202.93
135	393190.03	4484589.56	1415.54	-48.12	-205.51	3.33	-202.18
136	393389.77	4484602.73	1428.85	-46.31	-205.20	3.45	-201.74
137	390198.96	4484799.69	1289.93	-69.30	-212.54	1.67	-210.87
138	390398.82	4484801.51	1294.20	-67.11	-210.84	1.92	-208.92
139	390599.77	4484801.49	1300.22	-65.42	-209.82	2.25	-207.58
140	390797.34	4484800.62	1305.65	-64.44	-209.46	2.33	-207.12
141	390996.77	4484798.45	1311.83	-63.81	-209.52	2.40	-207.12
142	391197.41	4484799.80	1319.21	-63.90	-210.45	2.43	-208.02
143	391360.99	4484795.18	1327.08	-64.62	-212.05	2.23	-209.83
144	391604.00	4484782.93	1338.93	-63.49	-212.25	1.95	-210.30
145	391810.12	4484863.37	1348.17	-62.32	-212.12	2.20	-209.92

Table 3. (Cont.)

Station	Easting (m)	Northing (m)	Elevation (m)	Free Air Anomaly (mGal)	Simple Bouguer Anomaly rho = 2.67 (mGal)	Terrain Correction (mGal)	Complete Bouguer Anomaly (mGal)
146	392012.17	4484820.50	1356.91	-61.26	-212.05	2.69	-209.36
147	392204.15	4484807.17	1368.52	-59.29	-211.39	2.39	-208.99
148	392382.19	4484818.02	1374.77	-57.16	-209.96	2.37	-207.59
149	392606.50	4484793.72	1388.80	-53.56	-207.94	2.38	-205.56
150	392810.22	4484803.67	1396.66	-51.53	-206.79	3.05	-203.74
151	392996.23	4484800.01	1402.66	-50.13	-206.07	3.38	-202.69
152	393208.59	4484798.19	1415.84	-48.10	-205.52	3.20	-202.32
153	393402.42	4484793.04	1429.23	-46.21	-205.14	3.30	-201.83
154	390558.50	4485002.67	1299.13	-65.92	-210.20	1.98	-208.22
155	390805.33	4484999.94	1305.55	-64.29	-209.30	2.20	-207.09
156	391000.17	4485006.14	1311.53	-63.21	-208.89	2.19	-206.70
157	391208.36	4485002.94	1318.09	-62.71	-209.12	2.17	-206.96
158	391378.66	4485008.00	1323.05	-62.76	-209.74	2.16	-207.58
159	390592.90	4485189.96	1298.30	-66.52	-210.71	2.27	-208.44
160	390806.80	4485197.23	1303.17	-64.93	-209.67	2.35	-207.31
161	390994.86	4485205.02	1308.23	-63.71	-209.01	2.38	-206.64
162	391191.31	4485202.99	1313.34	-62.81	-208.69	2.48	-206.21
163	391389.68	4485198.81	1317.53	-62.38	-208.73	2.80	-205.93
164	390600.57	4485404.82	1298.45	-67.03	-211.23	2.17	-209.07
165	390806.07	4485397.56	1302.24	-65.11	-209.75	2.46	-207.28
166	390991.81	4485400.37	1307.19	-63.75	-208.94	2.56	-206.38
167	391201.42	4485400.89	1312.81	-62.46	-208.28	2.71	-205.58
168	391411.21	4485407.40	1319.42	-61.53	-208.10	2.81	-205.29
169	391793.76	4485402.83	1331.61	-60.45	-208.40	3.09	-205.31
170	392003.57	4485409.84	1340.47	-59.94	-208.89	3.22	-205.67
171	392210.93	4485399.82	1357.14	-58.24	-209.06	2.63	-206.43
172	392386.13	4485395.65	1364.93	-57.03	-208.73	2.98	-205.75
173	392602.82	4485404.24	1380.04	-54.18	-207.58	2.56	-205.01
174	392808.41	4485408.16	1393.48	-51.63	-206.54	2.40	-204.14
175	393008.86	4485386.92	1400.32	-50.08	-205.76	2.83	-202.93
176	393204.85	4485401.72	1409.18	-48.45	-205.12	3.18	-201.95
177	393397.60	4485378.63	1421.26	-46.66	-204.70	3.46	-201.23
178	390598.38	4485603.22	1297.44	-67.65	-211.75	2.12	-209.62
179	390802.66	4485588.71	1303.02	-65.71	-210.44	2.34	-208.10
180	391001.65	4485598.25	1308.84	-64.03	-209.41	2.44	-206.97
181	391195.69	4485608.05	1315.09	-62.53	-208.62	2.49	-206.13
182	391394.68	4485601.52	1321.44	-61.24	-208.03	2.62	-205.42
183	391789.54	4485602.55	1336.09	-60.56	-209.01	2.69	-206.31
184	392005.55	4485596.59	1344.74	-58.96	-208.38	2.86	-205.52
185	392195.18	4485601.95	1357.34	-57.12	-207.96	2.47	-205.50
186	392392.96	4485606.08	1365.83	-55.68	-207.48	2.76	-204.72
187	392595.18	4485596.87	1374.17	-53.93	-206.67	3.06	-203.61
188	392789.81	4485594.42	1384.52	-52.14	-206.04	3.16	-202.88

Table 3. (Cont.)

Station	Easting (m)	Northing (m)	Elevation (m)	Free Air Anomaly (mGal)	Simple Bouguer Anomaly rho = 2.67 (mGal)	Terrain Correction (mGal)	Complete Bouguer Anomaly (mGal)
189	392992.93	4485609.32	1395.33	-50.38	-205.50	3.41	-202.09
190	393190.58	4485600.46	1406.79	-48.53	-204.94	3.55	-201.39
191	393410.89	4485589.40	1421.84	-46.23	-204.33	3.65	-200.69
192	390602.33	4485800.54	1296.62	-67.88	-211.88	2.19	-209.68
193	390801.66	4485795.69	1303.42	-65.93	-210.70	2.42	-208.28
194	390997.98	4485795.90	1309.96	-64.18	-209.68	2.49	-207.19
195	391207.43	4485799.68	1316.38	-62.57	-208.79	2.56	-206.23
196	391393.73	4485799.81	1322.62	-61.32	-208.25	2.67	-205.58
197	390599.75	4486004.18	1297.09	-68.05	-212.11	2.17	-209.94
198	390790.81	4486000.83	1304.14	-66.28	-211.13	2.35	-208.78
199	391008.86	4486000.83	1311.10	-64.23	-209.87	2.77	-207.10
200	391195.80	4486001.83	1317.47	-62.72	-209.07	2.74	-206.33
201	391401.88	4486005.65	1324.26	-61.16	-208.28	2.79	-205.48
202	392204.52	4486196.46	1355.27	-56.26	-206.87	3.54	-203.33
203	392401.53	4486195.39	1368.81	-54.09	-206.22	3.06	-203.16
204	392607.68	4486202.41	1380.24	-52.10	-205.51	3.44	-202.08
205	392797.56	4486213.15	1386.47	-50.80	-204.92	3.94	-200.99
206	392994.78	4486199.66	1397.29	-49.08	-204.42	3.84	-200.58
207	393208.92	4486206.96	1406.66	-47.37	-203.77	4.27	-199.49
208	391995.44	4486410.01	1354.14	-56.31	-206.79	2.86	-203.93
209	392201.39	4486396.46	1361.94	-55.14	-206.50	3.09	-203.40
210	392402.44	4486394.61	1370.46	-53.85	-206.16	3.33	-202.83
211	392610.35	4486401.15	1389.52	-51.01	-205.47	2.68	-202.79
212	392790.21	4486404.21	1391.88	-50.01	-204.74	3.68	-201.06
213	392993.90	4486399.85	1402.82	-48.24	-204.19	3.90	-200.30
214	393192.87	4486395.81	1412.09	-46.55	-203.55	4.25	-199.30
215	392391.80	4489807.61	1339.08	-56.75	-205.54	2.53	-203.01
216	392790.17	4489804.98	1361.84	-53.05	-204.40	2.82	-201.59
217	392396.10	4490194.26	1335.91	-57.58	-206.02	2.40	-203.61
218	392799.07	4490203.45	1359.24	-53.64	-204.70	2.37	-202.33
219	393200.87	4490200.04	1387.80	-49.40	-203.67	2.35	-201.33
220	392395.02	4490597.27	1330.37	-58.95	-206.76	2.31	-204.45
221	392800.87	4490596.94	1349.55	-55.31	-205.28	2.62	-202.66
222	393134.27	4490595.90	1368.21	-52.12	-204.19	2.77	-201.42
223	392397.74	4491001.62	1321.92	-60.51	-207.37	2.42	-204.95
224	392798.95	4491013.12	1341.90	-56.82	-205.93	2.41	-203.52
225	393207.36	4491001.46	1363.93	-52.86	-204.45	2.88	-201.57
226	390801.59	4491605.74	1275.79	-73.11	-214.77	1.98	-212.80
227	391178.25	4491601.39	1280.11	-71.13	-213.28	2.14	-211.15
228	390803.24	4491998.38	1273.63	-74.33	-215.75	1.94	-213.81
229	391198.88	4492000.27	1277.88	-72.10	-214.00	1.97	-212.04
230	391589.73	4492004.40	1285.54	-70.46	-213.22	1.93	-211.29
231	390802.03	4492407.01	1270.98	-75.52	-216.64	1.93	-214.71

Table 3. (Cont.)

Station	Easting (m)	Northing (m)	Elevation (m)	Free Air Anomaly (mGal)	Simple Bouguer Anomaly rho = 2.67 (mGal)	Terrain Correction (mGal)	Complete Bouguer Anomaly (mGal)
232	391196.37	4492405.81	1273.67	-73.44	-214.86	2.07	-212.79
233	391595.57	4492402.65	1280.78	-71.17	-213.39	2.01	-211.38
234	391995.25	4492396.87	1290.85	-68.84	-212.20	1.90	-210.30
235	390798.87	4492802.59	1268.20	-76.30	-217.11	2.03	-215.08
236	391204.61	4492792.72	1270.74	-74.55	-215.65	2.04	-213.61
237	391599.97	4492807.53	1276.28	-72.63	-214.35	2.04	-212.31
238	391995.48	4492797.05	1284.30	-70.78	-213.41	2.12	-211.29
239	390788.95	4493198.25	1266.49	-76.63	-217.25	2.04	-215.21
240	391192.89	4493201.68	1268.64	-75.35	-216.21	2.03	-214.18
241	391588.45	4493202.19	1272.53	-73.98	-215.28	2.11	-213.17
242	391996.67	4493200.16	1280.67	-72.38	-214.60	2.12	-212.48
243	390802.36	4493601.12	1266.09	-77.04	-217.61	1.90	-215.71
244	391201.93	4493598.14	1266.60	-76.13	-216.76	2.03	-214.73
245	391597.06	4493476.72	1269.96	-74.79	-215.80	2.28	-213.52
247	390801.64	4493997.72	1265.42	-77.84	-218.34	1.88	-216.46
248	391195.84	4493997.83	1266.60	-77.11	-217.74	1.97	-215.77
249	391603.00	4494015.49	1270.02	-75.80	-216.82	1.99	-214.83
250	391999.29	4493998.43	1272.56	-74.18	-215.49	2.14	-213.35
251	390799.38	4494400.54	1266.85	-78.52	-219.18	1.67	-217.50
252	391205.65	4494406.24	1271.17	-77.47	-218.62	1.73	-216.89
253	391589.66	4494401.71	1269.85	-76.49	-217.49	1.95	-215.54
254	392009.40	4494423.14	1271.23	-74.74	-215.89	1.98	-213.91
255	392385.55	4494398.81	1276.03	-72.69	-214.39	1.76	-212.63
256	392787.31	4494397.41	1277.98	-70.51	-212.43	1.98	-210.45
257	390804.94	4494797.74	1266.41	-79.17	-219.78	1.65	-218.13
258	391191.14	4494799.18	1270.68	-78.35	-219.43	1.36	-218.07
259	391567.92	4494771.12	1269.24	-77.36	-218.29	1.75	-216.54
260	391999.55	4494804.51	1270.47	-75.92	-216.99	1.94	-215.05
261	392397.83	4494786.68	1273.98	-73.98	-215.44	1.71	-213.74
262	392795.31	4494791.72	1274.03	-72.25	-213.73	1.99	-211.74
263	390800.69	4495199.34	1264.58	-79.75	-220.15	1.79	-218.36
264	391197.00	4495200.52	1265.44	-79.27	-219.76	1.78	-217.99
265	391601.18	4495197.94	1269.47	-78.13	-219.08	1.75	-217.33
266	391997.85	4495200.31	1269.85	-77.14	-218.14	1.87	-216.27
267	392386.47	4495215.43	1275.52	-75.53	-217.17	1.54	-215.63
268	392803.68	4495197.18	1272.94	-73.54	-214.89	1.81	-213.08
269	390799.71	4495597.44	1261.30	-80.52	-220.56	2.09	-218.47
270	391203.45	4495602.06	1265.76	-79.81	-220.34	1.69	-218.65
271	391602.78	4495608.14	1271.40	-78.88	-220.05	1.27	-218.79
272	391998.57	4495601.99	1269.70	-78.04	-219.02	1.56	-217.45
273	392398.83	4495603.63	1269.25	-76.65	-217.59	1.70	-215.89
274	392798.79	4495594.93	1270.21	-74.66	-215.70	1.76	-213.94
275	390800.52	4495999.83	1262.60	-79.83	-220.01	2.07	-217.94

Table 3. (Cont.)

Station	Easting (m)	Northing (m)	Elevation (m)	Free Air Anomaly (mGal)	Simple Bouguer Anomaly rho = 2.67 (mGal)	Terrain Correction (mGal)	Complete Bouguer Anomaly (mGal)
276	391201.68	4495998.78	1262.09	-80.40	-220.53	2.03	-218.50
277	391602.04	4496002.93	1264.34	-79.56	-219.94	1.86	-218.08
278	392002.99	4496002.25	1264.40	-78.75	-219.13	1.93	-217.20
279	392403.80	4496001.26	1265.15	-77.56	-218.03	1.98	-216.05
280	392802.21	4495997.16	1268.34	-75.75	-216.58	1.87	-214.71
9999	393626.29	4493552.61	1305.40	-60.59	-205.59	1.87	-203.73
RP1	392444.80	4487323.55	1376.49	-49.47	-204.91	1.91	-203.01
RP10	395961.54	4486520.61	1641.13	-19.14	-204.31	13.69	-190.63
RP100	390295.10	4486079.01	1288.17	-67.86	-213.37	0.87	-212.51
RP101	390199.35	4485686.71	1287.80	-68.25	-213.72	0.86	-212.86
RP102	390089.80	4485238.65	1281.03	-68.64	-213.35	0.74	-212.61
RP103	394510.51	4496894.51	1277.03	-64.88	-209.14	1.23	-207.91
RP104	393940.10	4496283.97	1275.17	-67.12	-211.16	0.92	-210.24
RP105	392650.04	4494210.68	1276.32	-68.69	-212.86	0.94	-211.92
RP106	394089.57	4496977.21	1268.68	-69.77	-213.08	0.68	-212.41
RP107	393526.07	4496360.27	1270.10	-70.69	-214.17	0.69	-213.48
RP109	391892.44	4495324.94	1271.17	-74.32	-217.91	0.49	-217.41
RP11	393777.60	4487122.93	1470.69	-35.73	-201.76	3.01	-198.75
RP110	391434.69	4496026.75	1264.17	-76.80	-219.61	0.27	-219.34
RP112	391957.11	4493767.70	1275.96	-71.99	-216.12	0.83	-215.29
RP114	391882.31	4492871.11	1277.24	-69.99	-214.27	0.85	-213.41
RP115	391107.19	4492996.87	1264.36	-74.01	-216.83	0.62	-216.22
RP116	390294.56	4493023.56	1261.41	-76.30	-218.80	0.40	-218.39
RP117	395198.50	4496297.34	1295.62	-56.25	-202.59	1.26	-201.33
RP118	394876.78	4496026.42	1298.43	-56.04	-202.70	1.42	-201.28
RP119	394646.88	4495685.48	1300.05	-56.54	-203.39	1.44	-201.94
RP12	394315.98	4487158.93	1514.75	-30.28	-201.26	3.31	-197.95
RP120	394421.87	4495351.48	1300.80	-56.81	-203.74	1.62	-202.12
RP121	394201.10	4495019.19	1301.21	-57.27	-204.25	1.69	-202.55
RP122	393980.39	4494673.93	1299.09	-58.43	-205.17	1.61	-203.56
RP123	393804.51	4494311.59	1297.08	-59.34	-205.85	1.51	-204.34
RP124	393628.38	4493949.60	1296.36	-59.79	-206.22	1.63	-204.59
RP125	393452.45	4493591.16	1298.19	-59.80	-206.43	1.64	-204.79
RP126	393279.01	4493236.91	1302.56	-59.70	-206.82	1.63	-205.19
RP127	393098.82	4492866.88	1307.45	-59.55	-207.23	1.72	-205.50
RP128	392924.98	4492510.20	1311.73	-59.06	-207.22	1.79	-205.42
RP129	392742.16	4492136.67	1313.73	-59.06	-207.44	1.77	-205.68
RP13	394830.90	4487165.20	1568.50	-24.21	-201.23	3.74	-197.49
RP130	392571.11	4491787.84	1314.55	-59.16	-207.63	1.70	-205.93
RP132	392214.38	4491053.76	1313.61	-59.84	-208.21	1.50	-206.72
RP133	392119.30	4490650.21	1316.60	-59.19	-207.89	1.47	-206.42
RP134	392072.99	4490258.84	1320.59	-58.15	-207.31	1.53	-205.77
RP135	392048.05	4489851.95	1324.30	-56.97	-206.54	1.56	-204.98

Table 3. (Cont.)

Station	Easting (m)	Northing (m)	Elevation (m)	Free Air Anomaly (mGal)	Simple Bouguer Anomaly rho = 2.67 (mGal)	Terrain Correction (mGal)	Complete Bouguer Anomaly (mGal)
RP136	391988.61	4489454.77	1324.31	-56.84	-206.41	1.50	-204.91
RP137	391932.33	4489066.10	1327.19	-56.33	-206.23	1.50	-204.73
RP138	391874.52	4488671.46	1331.79	-55.93	-206.34	1.50	-204.84
RP139	391823.06	4488276.28	1337.43	-55.41	-206.45	1.57	-204.89
RP14	395276.93	4487327.02	1655.33	-14.84	-201.60	4.88	-196.73
RP140	391789.00	4487866.63	1344.70	-54.09	-205.96	1.76	-204.20
RP141	391873.58	4487424.96	1349.52	-53.24	-205.65	1.72	-203.94
RP142	391845.09	4487083.85	1347.91	-52.87	-205.09	1.71	-203.38
RP143	391808.51	4486681.79	1347.77	-54.41	-206.62	1.56	-205.06
RP144	391771.09	4486274.75	1343.23	-55.29	-206.99	1.48	-205.52
RP146	391647.22	4485077.00	1328.93	-59.68	-209.77	1.70	-208.07
RP147	391594.86	4484622.33	1344.56	-60.85	-212.70	1.93	-210.77
RP148	386643.53	4484360.29	1283.91	-63.52	-208.55	0.23	-208.32
RP149	386476.93	4485968.65	1278.79	-62.92	-207.37	0.16	-207.21
RP15	395845.91	4487554.10	1732.87	-6.71	-202.17	7.92	-194.25
RP150	386299.13	4487563.98	1284.66	-62.50	-207.62	0.14	-207.47
RP151	386151.34	4489238.37	1288.73	-63.73	-209.30	0.09	-209.20
RP152	386011.36	4490753.98	1287.98	-65.90	-211.38	0.11	-211.27
RP153	385896.80	4492370.58	1281.16	-68.06	-212.78	0.10	-212.67
RP154	385774.35	4493959.55	1273.97	-68.73	-212.63	0.11	-212.53
RP155	385104.14	4495513.22	1277.28	-65.01	-209.29	0.18	-209.10
RP156	393334.67	4485116.44	1418.45	-44.96	-205.12	2.67	-202.45
RP157	393736.96	4485129.69	1448.26	-40.88	-204.39	2.91	-201.48
RP158	394142.96	4485154.35	1471.01	-38.42	-204.48	3.49	-201.00
RP159	394382.60	4485189.70	1504.35	-34.24	-204.05	4.08	-199.97
RP16	393981.28	4488013.25	1479.78	-34.90	-201.95	3.25	-198.71
RP160	392538.86	4485128.18	1379.75	-53.27	-209.08	2.85	-206.23
RP161	392155.87	4485266.82	1348.89	-58.30	-210.64	1.79	-208.85
RP162	392202.09	4486730.83	1364.83	-51.39	-205.52	1.87	-203.65
RP163	392603.73	4486740.37	1387.29	-47.99	-204.65	2.22	-202.42
RP164	393294.64	4486739.23	1430.83	-40.96	-202.51	2.46	-200.05
RP165	393696.31	4486727.28	1459.61	-37.04	-201.82	3.08	-198.74
RP166	394099.78	4486710.33	1525.38	-29.78	-201.96	4.37	-197.59
RP168	394186.80	4486364.25	1526.65	-29.66	-201.98	4.48	-197.50
RP169	393857.29	4486424.00	1482.47	-34.78	-202.13	3.11	-199.02
RP170	393436.43	4486469.74	1429.44	-41.52	-202.91	2.60	-200.31
RP171	393866.07	4487416.67	1476.99	-34.56	-201.29	3.28	-198.01
RP172	394051.17	4487750.79	1490.36	-32.40	-200.64	3.44	-197.20
RP173	394464.12	4487863.29	1522.82	-28.76	-200.65	4.33	-196.32
RP174	393936.96	4488214.62	1473.23	-35.13	-201.44	3.65	-197.79
RP175	394050.52	4488588.28	1462.98	-35.88	-201.04	3.37	-197.67
RP176	394007.72	4488985.92	1449.63	-37.64	-201.31	3.14	-198.17
RP177	393625.98	4488884.76	1443.05	-39.61	-202.53	4.16	-198.37

Table 3. (Cont.)

Station	Easting (m)	Northing (m)	Elevation (m)	Free Air Anomaly (mGal)	Simple Bouguer Anomaly rho = 2.67 (mGal)	Terrain Correction (mGal)	Complete Bouguer Anomaly (mGal)
RP178	393248.77	4488733.72	1408.63	-44.87	-203.92	2.83	-201.09
RP179	392867.96	4488610.16	1377.43	-48.78	-204.33	2.45	-201.88
RP18	394425.44	4489578.43	1498.13	-31.02	-200.13	4.20	-195.93
RP180	392443.83	4488625.70	1352.31	-52.41	-205.13	1.96	-203.17
RP183	393958.64	4488083.52	1474.63	-36.00	-202.47	3.21	-199.27
RP184	393581.24	4488052.03	1453.47	-39.66	-203.75	2.65	-201.09
RP185	393216.04	4487890.60	1423.21	-43.43	-204.12	2.52	-201.60
RP187	392473.08	4487587.17	1376.64	-49.98	-205.44	1.91	-203.53
RP188	392616.19	4487247.58	1387.89	-47.80	-204.53	2.08	-202.45
RP189	393187.70	4489271.96	1390.67	-46.19	-203.23	2.68	-200.55
RP19	395004.06	4489513.08	1553.63	-24.16	-199.50	6.61	-192.89
RP190	392789.70	4489311.65	1366.11	-49.74	-204.01	2.35	-201.67
RP191	392384.19	4489365.34	1342.63	-53.47	-205.10	1.86	-203.23
RP192	394001.76	4491218.65	1426.09	-41.10	-202.11	3.52	-198.60
RP193	393564.61	4491261.19	1389.89	-46.79	-203.73	3.00	-200.73
RP194	393175.83	4491246.43	1357.50	-51.71	-205.01	2.25	-202.76
RP195	392789.71	4491410.41	1330.78	-56.26	-206.56	1.95	-204.61
RP196	392897.19	4492302.65	1315.55	-58.30	-206.89	1.81	-205.08
RP197	393922.96	4491554.30	1406.69	-43.97	-202.80	4.07	-198.73
RP198	393546.57	4491676.14	1364.94	-49.99	-204.13	2.65	-201.48
RP199	393167.72	4491826.78	1337.64	-54.62	-205.69	2.07	-203.62
RP2	392819.67	4487228.45	1400.51	-46.43	-204.57	2.18	-202.39
RP20	395553.56	4489448.41	1608.02	-18.56	-200.02	9.09	-190.93
RP200	392728.32	4491998.53	1315.27	-58.78	-207.34	1.73	-205.60
RP201	392243.37	4488194.25	1358.53	-51.61	-205.03	2.00	-203.03
RP202	392684.06	4487943.86	1389.27	-47.15	-204.03	2.42	-201.62
RP203	393858.50	4486711.43	1497.59	-33.17	-202.23	4.29	-197.94
RP204	394248.00	4486689.36	1534.47	-28.63	-201.82	3.63	-198.19
RP21	396044.03	4489194.19	1670.23	-11.62	-200.05	8.25	-191.80
RP22	396528.79	4488942.08	1727.31	-5.69	-200.53	9.04	-191.49
RP23	396807.34	4488720.50	1771.07	-2.35	-202.10	7.77	-194.33
RP24	393782.64	4489263.36	1436.68	-39.50	-201.71	2.74	-198.97
RP25	393073.44	4489230.41	1384.27	-47.14	-203.46	2.66	-200.80
RP26	392663.45	4488990.15	1358.54	-51.17	-204.59	1.93	-202.66
RP27	392253.56	4489023.04	1339.36	-54.05	-205.31	1.70	-203.61
RP28	393907.67	4484285.02	1458.29	-38.90	-203.54	2.93	-200.61
RP29	393389.44	4484262.97	1427.77	-42.46	-203.66	2.65	-201.02
RP3	393216.04	4487173.58	1430.44	-41.80	-203.30	2.51	-200.79
RP30	392931.29	4484270.19	1405.93	-47.01	-205.76	2.32	-203.44
RP31	392502.25	4484274.02	1388.80	-51.01	-207.84	2.02	-205.82
RP32	392141.79	4484279.22	1372.59	-56.19	-211.19	1.77	-209.42
RP33	391750.54	4484283.21	1353.90	-60.10	-213.00	1.56	-211.43
RP34	391460.83	4484292.52	1340.63	-62.06	-213.47	1.40	-212.07

Table 3. (Cont.)

Station	Easting (m)	Northing (m)	Elevation (m)	Free Air Anomaly (mGal)	Simple Bouguer Anomaly rho = 2.67 (mGal)	Terrain Correction (mGal)	Complete Bouguer Anomaly (mGal)
RP35	397275.20	4493525.92	1597.76	-14.98	-195.28	5.55	-189.74
RP36	396898.44	4493855.21	1537.48	-21.61	-195.14	4.21	-190.92
RP37	396483.06	4494187.28	1487.79	-27.59	-195.54	3.84	-191.70
RP38	396116.03	4494451.64	1442.86	-32.23	-195.13	3.31	-191.82
RP39	395929.28	4494871.71	1400.53	-37.54	-195.69	3.68	-192.00
RP4	393612.32	4487129.40	1460.35	-37.11	-201.97	2.88	-199.10
RP40	395826.91	4495273.61	1366.66	-41.65	-195.98	2.60	-193.39
RP41	395655.28	4495647.52	1346.78	-45.11	-197.20	2.69	-194.51
RP42	395464.84	4495999.82	1325.04	-48.76	-198.41	2.14	-196.27
RP44	392920.48	4485094.61	1392.77	-48.97	-206.24	2.38	-203.86
RP45	392900.40	4485910.50	1389.68	-48.35	-205.27	2.40	-202.87
RP46	392886.00	4486726.76	1401.51	-46.10	-204.35	2.41	-201.94
RP47	392876.84	4487511.19	1405.61	-45.20	-203.91	2.36	-201.55
RP48	392906.24	4488314.50	1389.69	-47.68	-204.60	2.52	-202.09
RP49	393004.79	4489126.70	1376.48	-49.06	-204.50	2.23	-202.27
RP5	394055.81	4487092.78	1483.61	-33.25	-200.73	3.09	-197.64
RP50	393123.65	4489938.60	1383.41	-47.87	-204.09	2.33	-201.76
RP51	393543.75	4489924.60	1416.14	-43.45	-203.34	2.82	-200.53
RP52	393950.32	4489917.81	1450.40	-38.82	-202.57	3.41	-199.16
RP53	394347.75	4489898.96	1462.03	-36.62	-201.67	3.27	-198.40
RP54	394745.06	4489902.55	1515.71	-28.62	-199.71	4.04	-195.67
RP55	395318.70	4491215.92	1566.25	-22.13	-198.89	6.14	-192.75
RP56	394906.16	4490931.50	1507.83	-29.25	-199.45	4.52	-194.93
RP57	394514.10	4491050.73	1477.22	-33.94	-200.70	3.73	-196.98
RP58	394115.91	4491178.39	1438.94	-39.37	-201.83	3.84	-198.00
RP59	393844.84	4491853.75	1386.06	-45.23	-201.74	3.50	-198.24
RP6	394459.70	4487059.30	1516.51	-27.64	-198.82	4.26	-194.55
RP60	393461.86	4492017.09	1364.89	-48.30	-202.43	3.56	-198.87
RP61	393044.27	4492245.13	1329.16	-55.11	-205.22	2.45	-202.78
RP62	391682.38	4485929.96	1333.12	-56.92	-207.48	1.40	-206.08
RP63	392081.58	4485890.10	1346.14	-55.71	-207.74	1.65	-206.09
RP64	392493.92	4485856.50	1370.40	-51.58	-206.33	2.10	-204.23
RP65	392886.69	4485829.32	1390.88	-48.19	-205.25	2.59	-202.66
RP66	393289.12	4485801.68	1415.37	-44.54	-204.35	2.92	-201.44
RP67	393695.96	4485779.78	1440.96	-40.91	-203.59	3.11	-200.49
RP68	394102.91	4485718.15	1470.89	-37.30	-203.35	3.30	-200.05
RP69	394504.37	4485735.34	1507.90	-31.84	-202.05	3.86	-198.19
RP7	394925.73	4486956.13	1549.26	-25.66	-200.52	5.72	-194.80
RP70	394906.22	4485714.58	1548.65	-27.31	-202.09	4.39	-197.70
RP71	394820.34	4496643.42	1287.76	-59.23	-204.69	1.29	-203.41
RP72	394543.49	4496350.34	1286.40	-60.41	-205.72	1.20	-204.52
RP73	394260.35	4496050.58	1286.83	-61.60	-206.95	1.34	-205.61
RP74	393968.92	4495741.29	1286.59	-62.81	-208.14	1.40	-206.75

Table 3. (Cont.)

Station	Easting (m)	Northing (m)	Elevation (m)	Free Air Anomaly (mGal)	Simple Bouguer Anomaly rho = 2.67 (mGal)	Terrain Correction (mGal)	Complete Bouguer Anomaly (mGal)
RP75	393719.90	4495351.03	1285.66	-63.81	-209.04	1.19	-207.85
RP76	393576.09	4495088.17	1285.14	-64.11	-209.28	1.21	-208.06
RP77	393383.50	4494717.42	1283.61	-64.74	-209.73	1.20	-208.53
RP78	393186.46	4494356.41	1281.05	-65.36	-210.07	1.17	-208.90
RP79	392990.53	4493991.27	1283.77	-65.49	-210.50	1.17	-209.34
RP8	395305.01	4486731.97	1585.33	-22.18	-201.08	5.91	-195.17
RP80	392800.35	4493645.04	1282.59	-66.82	-211.70	1.09	-210.61
RP81	392614.29	4493309.53	1285.68	-66.73	-211.95	1.09	-210.87
RP82	392408.23	4492956.10	1285.58	-66.83	-212.05	1.05	-211.00
RP83	392213.12	4492600.41	1286.34	-66.77	-212.07	1.04	-211.03
RP84	392022.60	4492252.54	1286.99	-66.92	-212.30	1.01	-211.29
RP85	391834.20	4491871.66	1287.73	-67.34	-212.80	0.99	-211.81
RP86	391677.18	4491512.43	1287.78	-67.51	-212.98	0.98	-212.00
RP87	391538.77	4491136.17	1292.93	-66.22	-212.26	1.02	-211.24
RP88	391426.75	4490700.02	1293.57	-65.73	-211.85	1.03	-210.82
RP89	391335.32	4490335.84	1296.83	-64.72	-211.20	1.03	-210.18
RP9	395578.08	4486623.67	1603.16	-22.86	-203.77	7.60	-196.17
RP90	391243.51	4489962.68	1296.09	-64.26	-210.65	0.98	-209.67
RP91	391152.30	4489585.40	1295.61	-64.06	-210.41	1.00	-209.40
RP92	391055.56	4489189.77	1297.67	-63.68	-210.26	0.96	-209.29
RP93	390961.68	4488798.55	1298.19	-62.45	-209.08	0.96	-208.13
RP94	390863.97	4488413.04	1299.69	-63.57	-210.37	0.97	-209.40
RP95	390771.02	4488017.36	1303.04	-63.13	-210.31	1.05	-209.25
RP96	390675.04	4487624.39	1301.07	-63.94	-210.90	1.07	-209.83
RP97	390577.32	4487239.34	1300.16	-64.38	-211.24	1.02	-210.22
RP98	390483.35	4486851.45	1297.89	-65.28	-211.88	1.14	-210.74
RP99	390386.98	4486456.49	1289.69	-67.23	-212.91	0.87	-212.04
RPG8	392289.91	4487485.89	1364.82	-51.22	-205.35	1.72	-203.63
RPG82	393719.90	4495351.03	1285.66	-63.84	-209.06	1.19	-207.87

APPENDIX D
Magnetic Data

Table 4. Magenometer Data

Station	Latitude	Longitude	Elevation	Magnetometer	Interpolated Latitude	Interpolated Longitude	Diff Main Field - Mag	Interpolated Base	Interp Base - Interp Base Min	Diurnal Corrected
1	40.49221	-118.30037	1269.3	51935.2	51128.9	51129.0	806.2	51208.9	18.2	788.0
2	40.49217	-118.29800	1276.2	51947.9	51128.9	51128.9	819.0	51212.7	22.0	797.0
3	40.49224	-118.29566	1285.3	51920.0	51128.9	51128.9	791.1	51215.3	24.7	766.4
4	40.49228	-118.29333	1296.0	51931.0	51128.9	51128.9	802.1	51215.1	24.4	777.7
5	40.49229	-118.29088	1300.0	51876.0	51128.9	51128.9	747.1	51199.3	8.6	738.4
6	40.49235	-118.28863	1302.4	51853.4	51129.0	51129.0	724.4	51199.2	8.5	715.9
7	40.49244	-118.28607	1305.9	51889.1	51129.0	51129.0	760.1	51202.4	11.7	748.4
9	40.49252	-118.28152	1315.4	51908.9	51129.1	51129.1	779.8	51225.8	35.1	744.7
10	40.49249	-118.27919	1323.6	51949.1	51129.1	51129.1	820.0	51221.7	31.0	789.0
11	40.49239	-118.27686	1332.5	51984.1	51129.0	51129.0	855.1	51217.2	26.6	828.5
12	40.49248	-118.27462	1341.4	51953.0	51129.1	51129.1	823.9	51213.2	22.5	801.4
13	40.49250	-118.27222	1351.0	51961.2	51129.1	51129.1	832.1	51206.6	15.9	816.2
14	40.49244	-118.26988	1363.8	51946.8	51129.0	51129.0	817.8	51201.7	11.1	806.7
15	40.49253	-118.26748	1374.7	51905.4	51129.1	51129.1	776.3	51196.4	5.7	770.6
16	40.49253	-118.26500	1384.0	51799.0	51129.1	51129.1	669.9	51213.8	23.1	646.8
22	40.49398	-118.30041	1268.9	51909.0	51129.9	51129.9	779.1	51204.4	13.8	765.3
23	40.49402	-118.29806	1269.8	51962.6	51129.9	51129.9	832.7	51215.3	24.6	808.1
24	40.49408	-118.29565	1276.3	51923.0	51129.9	51129.9	793.1	51216.4	25.8	767.3
25	40.49410	-118.29333	1282.7	51938.0	51130.0	51130.0	808.0	51227.0	36.3	771.7
26	40.49410	-118.29098	1295.6	51899.0	51130.0	51130.0	769.0	51247.9	57.2	711.8
27	40.49414	-118.28862	1302.2	51898.0	51130.0	51130.0	768.0	51212.8	22.1	745.9
28	40.49418	-118.28627	1304.3	51892.2	51130.0	51130.0	762.2	51206.9	16.2	746.0
29	40.49408	-118.28382	1308.9	51915.7	51129.9	51129.9	785.8	51227.2	36.5	749.2
30	40.49411	-118.28147	1316.0	51901.0	51130.0	51130.0	771.0	51229.2	38.5	732.5
31	40.49431	-118.27907	1324.6	51920.1	51130.1	51130.1	790.0	51231.4	40.7	749.3
32	40.49417	-118.27684	1331.9	51971.2	51130.0	51130.0	841.2	51232.7	42.1	799.1
33	40.49429	-118.27432	1341.1	51971.9	51130.1	51130.1	841.8	51234.5	43.8	798.0
34	40.49425	-118.27207	1349.9	51977.7	51130.0	51130.0	847.7	51234.0	43.4	804.3
35	40.49435	-118.26973	1359.9	51975.9	51130.1	51130.1	845.8	51231.5	40.8	805.0
36	40.49443	-118.26734	1371.1	51904.1	51130.1	51130.1	774.0	51230.7	40.1	733.9
43	40.49581	-118.30046	1270.0	51951.8	51130.9	51130.9	820.9	51200.6	9.9	811.0

Table 4. (Cont.)

Station	Latitude	Longitude	Elevation	Magnetometer	Interpolated Latitude	Interpolated Longitude	Diff Main Field - Mag	Interpolated Base	Interp Base - Interp Base Min	Diurnal Corrected
44	40.49584	-118.29807	1270.0	51986.6	51130.9	51130.9	855.7	51222.5	31.9	823.8
45	40.49594	-118.29630	1271.6	51939.5	51131.0	51131.0	808.5	51228.6	37.9	770.6
46	40.49586	-118.29338	1277.3	51930.0	51130.9	51130.9	799.1	51223.0	32.4	766.7
47	40.49588	-118.29104	1283.4	51914.0	51131.0	51131.0	783.0	51247.9	57.2	725.8
48	40.49597	-118.28868	1290.1	51892.8	51131.0	51131.0	761.8	51217.1	26.5	735.3
49	40.49597	-118.28622	1299.4	51891.6	51131.0	51131.0	760.6	51221.6	31.0	729.6
50	40.49590	-118.28403	1305.6	51913.8	51131.0	51131.0	782.8	51225.5	34.8	748.0
51	40.49598	-118.28138	1318.5	51859.8	51131.0	51131.0	728.8	51232.3	41.7	687.1
52	40.49607	-118.27923	1325.3	51864.4	51131.1	51131.1	733.3	51231.9	41.2	692.1
53	40.49601	-118.27684	1334.1	51938.0	51131.0	51131.0	807.0	51236.7	46.0	761.0
54	40.49615	-118.27455	1344.1	51934.6	51131.1	51131.1	803.5	51239.6	49.0	754.5
55	40.49623	-118.27212	1353.6	51946.1	51131.2	51131.2	814.9	51236.9	46.2	768.7
56	40.49622	-118.26992	1362.3	51945.3	51131.1	51131.1	814.2	51238.1	47.4	766.7
57	40.49620	-118.26751	1369.7	51958.0	51131.1	51131.1	826.9	51241.1	50.4	776.4
58	40.49614	-118.26511	1381.5	51854.0	51131.1	51131.1	722.9	51213.3	22.6	700.3
64	40.49760	-118.30048	1268.5	51960.0	51131.9	51131.9	828.1	51200.0	9.3	818.8
65	40.49760	-118.29811	1270.4	51958.0	51131.9	51131.9	826.1	51203.7	13.0	813.1
66	40.49768	-118.29587	1272.5	51936.3	51132.0	51132.0	804.3	51232.4	41.7	762.6
67	40.49767	-118.29341	1278.6	51867.0	51132.0	51132.0	735.0	51227.7	37.1	698.0
68	40.49770	-118.29105	1286.7	51812.0	51132.0	51132.0	680.0	51245.5	54.9	625.2
69	40.49773	-118.28871	1291.8	51842.0	51132.0	51132.0	710.0	51217.2	26.5	683.5
70	40.49778	-118.28635	1298.7	51873.0	51132.0	51132.0	741.0	51216.2	25.6	715.4
71	40.49778	-118.28398	1306.9	51851.0	51132.0	51132.0	719.0	51218.0	27.3	691.7
72	40.49782	-118.28141	1316.7	51851.2	51132.0	51132.0	719.2	51225.9	35.2	683.9
73	40.49778	-118.27934	1324.8	51890.0	51132.0	51132.0	758.0	51217.3	26.7	731.3
74	40.49785	-118.27694	1332.2	51822.0	51132.1	51132.1	689.9	51211.6	20.9	669.0
75	40.49799	-118.27465	1340.9	51923.0	51132.1	51132.1	790.9	51211.8	21.1	769.7
76	40.49787	-118.27215	1351.0	51904.0	51132.1	51132.1	771.9	51211.2	20.5	751.4
77	40.49794	-118.26969	1359.5	51900.2	51132.1	51132.1	768.1	51202.8	12.1	756.0
78	40.49798	-118.26745	1368.7	51890.0	51132.1	51132.1	757.9	51212.1	21.5	736.4
81	40.49805	-118.26039	1400.4	51886.0	51132.2	51132.2	753.8	51205.5	14.9	738.9

Table 4. (Cont.)

Station	Latitude	Longitude	Elevation	Magnetometer	Interpolated Latitude	Interpolated Longitude	Diff Main Field - Mag	Interpolated Base	Interp Base - Interp Base Min	Diurnal Corrected
82	40.49811	-118.25809	1413.0	51924.0	51132.2	51132.2	791.8	51208.5	17.8	774.0
83	40.49798	-118.25642	1421.4	51942.0	51132.1	51132.1	809.9	51209.2	18.5	791.3
85	40.49939	-118.30051	1269.7	52005.0	51132.9	51132.9	872.1	51199.7	9.1	863.0
86	40.49938	-118.29817	1271.3	51981.0	51132.9	51132.9	848.1	51200.7	10.0	838.1
87	40.49945	-118.29579	1273.6	51935.0	51133.0	51133.0	802.0	51209.7	19.1	783.0
88	40.49948	-118.29344	1275.9	51865.0	51133.0	51133.0	732.0	51231.1	40.4	691.6
89	40.49952	-118.29111	1286.1	51884.0	51133.0	51133.0	751.0	51243.7	53.1	697.9
90	40.49950	-118.28864	1291.0	51803.8	51133.0	51133.0	670.8	51211.2	20.6	650.2
91	40.49959	-118.28629	1299.1	51779.1	51133.0	51133.0	646.1	51210.4	19.8	626.3
92	40.49961	-118.28404	1306.5	51753.7	51133.0	51133.0	620.7	51210.5	19.8	600.8
93	40.49929	-118.28128	1315.9	51737.6	51132.9	51132.9	604.7	51225.8	35.2	569.5
95	40.49965	-118.27693	1332.8	51723.1	51133.1	51133.1	590.0	51200.8	10.1	579.9
96	40.49963	-118.27458	1344.0	51874.0	51133.1	51133.1	740.9	51205.4	14.7	726.2
97	40.49983	-118.27223	1352.9	51889.6	51133.2	51133.2	756.4	51205.6	14.9	741.5
98	40.49976	-118.26982	1360.6	51855.0	51133.1	51133.1	721.9	51204.5	13.8	708.1
99	40.49976	-118.26756	1366.6	51904.0	51133.1	51133.1	770.9	51208.7	18.1	752.8
100	40.49976	-118.26507	1379.2	51923.3	51133.1	51133.1	790.2	51190.7	0.0	790.2
102	40.49982	-118.26041	1398.6	51977.2	51133.2	51133.2	844.0	51207.4	16.8	827.2
103	40.49984	-118.25805	1409.5	51891.0	51133.2	51133.2	757.8	51208.2	17.5	740.3
104	40.49976	-118.25638	1418.6	51878.0	51133.1	51133.1	744.9	51209.6	18.9	725.9
106	40.50125	-118.29585	1272.1	51941.0	51134.0	51134.0	807.0	51208.9	18.3	788.8
107	40.50127	-118.29348	1274.4	51894.0	51134.0	51134.0	760.0	51234.9	44.2	715.8
108	40.50131	-118.29111	1278.8	51799.0	51134.0	51134.0	665.0	51237.6	46.9	618.1
109	40.50131	-118.28874	1285.9	51850.0	51134.0	51134.0	716.0	51214.3	23.6	692.4
110	40.50142	-118.28667	1293.4	51668.0	51134.1	51134.1	533.9	51218.6	27.9	506.0
112	40.50119	-118.28275	1310.7	51772.0	51133.9	51133.9	638.1	51206.9	16.3	621.8
113	40.50254	-118.29604	1267.3	51959.0	51134.7	51134.7	824.3	51209.5	18.9	805.4
114	40.50296	-118.29345	1273.3	51976.0	51134.9	51134.9	841.1	51237.1	46.4	794.6
115	40.50310	-118.29115	1278.1	51791.0	51135.0	51135.0	656.0	51238.8	48.2	607.8
116	40.50313	-118.28879	1286.5	51451.0	51135.0	51135.0	316.0	51233.5	42.8	273.2
117	40.50309	-118.28641	1295.3	51784.0	51135.0	51135.0	649.0	51234.6	43.9	605.1

Table 4. (Cont.)

Station	Latitude	Longitude	Elevation	Magnetometer	Interpolated Latitude	Interpolated Longitude	Diff Main Field - Mag	Interpolated Base	Interp Base - Interp Base Min	Diurnal Corrected
118	40.50322	-118.28447	1305.2	51803.0	51135.1	51135.1	667.9	51201.4	10.7	657.2
119	40.50318	-118.28257	1313.1	51852.0	51135.1	51135.1	716.9	51199.3	8.6	708.3
120	40.50485	-118.29589	1270.9	52006.0	51136.0	51136.0	870.0	51217.8	27.2	842.8
121	40.50487	-118.29354	1272.2	51980.0	51136.0	51136.0	844.0	51197.5	6.8	837.2
122	40.50491	-118.29121	1278.0	51937.2	51136.0	51136.0	801.2	51197.1	6.4	794.8
123	40.50500	-118.28867	1285.0	51804.0	51136.1	51136.1	667.9	51229.4	38.8	629.2
124	40.50516	-118.28642	1288.9	51898.0	51136.2	51136.2	761.8	51234.0	43.4	718.5
125	40.50498	-118.28439	1295.9	51845.0	51136.1	51136.1	708.9	51204.3	13.6	695.3
126	40.50508	-118.28239	1310.8	51793.0	51136.1	51136.1	656.9	51198.1	7.4	649.4
127	40.50510	-118.27930	1322.0	51886.0	51136.1	51136.1	749.9	51234.5	43.8	706.1
128	40.50503	-118.27706	1330.8	51923.1	51136.1	51136.1	787.0	51232.8	42.1	744.9
129	40.50502	-118.27473	1340.0	51939.5	51136.1	51136.1	803.4	51230.5	39.9	763.6
130	40.50522	-118.27235	1345.2	51948.5	51136.2	51136.2	812.3	51228.1	37.5	774.9
131	40.50518	-118.27003	1357.3	51974.2	51136.2	51136.2	838.0	51225.4	34.8	803.2
132	40.50519	-118.26764	1363.4	51935.6	51136.2	51136.2	799.4	51223.6	33.0	766.4
133	40.50519	-118.26525	1372.7	52007.0	51136.2	51136.2	870.8	51222.2	31.5	839.3
134	40.50518	-118.26292	1382.5	51900.0	51136.2	51136.2	763.8	51219.5	28.9	734.9
135	40.50515	-118.26061	1393.5	51989.1	51136.2	51136.2	852.9	51216.7	26.1	826.9
136	40.50529	-118.25825	1407.0	51968.9	51136.2	51136.2	832.7	51213.8	23.2	809.5
137	40.50664	-118.29594	1270.7	52017.0	51137.0	51137.0	880.0	51215.4	24.8	855.2
138	40.50669	-118.29358	1275.5	52026.0	51137.0	51137.0	889.0	51215.3	24.6	864.4
139	40.50671	-118.29121	1281.5	51951.0	51137.0	51137.0	814.0	51217.0	26.3	787.6
140	40.50675	-118.28887	1283.5	51922.0	51137.1	51137.1	784.9	51195.1	4.5	780.5
141	40.50675	-118.28651	1290.3	51909.0	51137.1	51137.1	771.9	51194.4	3.7	768.2
142	40.50679	-118.28415	1297.8	51916.0	51137.1	51137.1	778.9	51193.6	3.0	776.0
143	40.50676	-118.28223	1307.4	51888.0	51137.1	51137.1	750.9	51193.3	2.7	748.3
144	40.50668	-118.27937	1315.9	51873.0	51137.0	51137.0	736.0	51238.3	47.7	688.3
145	40.50743	-118.27695	1324.8	51997.0	51137.4	51137.4	859.6	51239.0	48.3	811.3
146	40.50706	-118.27456	1331.5	51930.0	51137.2	51137.2	792.8	51235.6	44.9	747.9
147	40.50697	-118.27229	1342.8	52010.6	51137.2	51137.2	873.4	51233.8	43.1	830.3
148	40.50709	-118.27019	1349.5	51973.6	51137.2	51137.2	836.4	51228.3	37.7	798.7

Table 4. (Cont.)

Station	Latitude	Longitude	Elevation	Magnetometer	Interpolated Latitude	Interpolated Longitude	Diff Main Field - Mag	Interpolated Base	Interp Base - Interp Base Min	Diurnal Corrected
149	40.50690	-118.26754	1364.7	51981.8	51137.1	51137.1	844.7	51224.0	33.3	811.3
150	40.50701	-118.26513	1373.6	51960.7	51137.2	51137.2	823.5	51223.9	33.2	790.3
151	40.50701	-118.26293	1380.3	51940.0	51137.2	51137.2	802.8	51224.5	33.8	769.0
152	40.50703	-118.26043	1393.6	51969.1	51137.2	51137.2	831.9	51207.4	16.7	815.2
153	40.50700	-118.25814	1408.2	51974.3	51137.2	51137.2	837.1	51210.4	19.7	817.4
154	40.50853	-118.29174	1276.6	51890.0	51138.1	51138.1	751.9	51220.8	30.2	721.8
155	40.50852	-118.28884	1276.2	51995.0	51138.0	51138.0	857.0	51231.5	40.9	816.1
156	40.50860	-118.28654	1283.0	51870.0	51138.1	51138.1	731.9	51228.2	37.6	694.4
157	40.50861	-118.28407	1290.7	51911.0	51138.1	51138.1	772.9	51227.8	37.1	735.8
158	40.50868	-118.28206	1295.8	51898.0	51138.1	51138.1	759.9	51225.9	35.2	724.6
159	40.51021	-118.29137	1274.9	51729.0	51139.0	51139.0	590.0	51221.4	30.8	559.3
160	40.51031	-118.28884	1277.0	51964.1	51139.0	51139.0	825.1	51221.1	30.5	794.6
161	40.51040	-118.28662	1282.6	51981.9	51139.1	51139.1	842.8	51222.3	31.7	811.1
162	40.51041	-118.28430	1286.0	51977.0	51139.1	51139.1	837.9	51223.7	33.0	804.9
163	40.51040	-118.28196	1290.3	51973.0	51139.1	51139.1	833.9	51225.7	35.1	798.8
164	40.51215	-118.29131	1274.4	51942.0	51140.1	51140.1	801.9	51221.6	30.9	771.0
165	40.51211	-118.28889	1279.0	51872.0	51140.1	51140.1	731.9	51221.2	30.6	701.4
166	40.51217	-118.28670	1284.5	51841.0	51140.1	51140.1	700.9	51221.9	31.3	669.6
167	40.51219	-118.28422	1289.2	51901.0	51140.1	51140.1	760.9	51221.8	31.2	729.7
168	40.51228	-118.28175	1295.0	51924.0	51140.2	51140.2	783.8	51214.5	23.8	760.0
169	40.51228	-118.27723	1308.5	51866.9	51140.2	51140.2	726.7	51222.5	31.9	694.9
170	40.51237	-118.27476	1318.7	51944.1	51140.2	51140.2	803.9	51221.3	30.7	773.2
171	40.51231	-118.27231	1335.2	51991.9	51140.2	51140.2	851.7	51219.5	28.9	822.9
172	40.51230	-118.27024	1342.4	51972.1	51140.2	51140.2	831.9	51218.8	28.2	803.8
173	40.51240	-118.26769	1356.5	51928.1	51140.2	51140.2	787.9	51218.0	27.3	760.6
174	40.51246	-118.26526	1370.3	51988.4	51140.3	51140.3	848.1	51219.6	29.0	819.2
175	40.51230	-118.26288	1377.3	51935.0	51140.2	51140.2	794.8	51221.8	31.1	763.7
176	40.51245	-118.26058	1386.0	51826.8	51140.3	51140.3	686.5	51221.3	30.6	655.9
177	40.51227	-118.25829	1398.6	51786.1	51140.1	51140.1	646.0	51220.8	30.1	615.8
179	40.51383	-118.28896	1279.1	51938.3	51141.0	51141.0	797.3	51203.3	12.6	784.6
180	40.51394	-118.28662	1285.3	51891.0	51141.1	51141.1	749.9	51204.0	13.4	736.6

Table 4. (Cont.)

Station	Latitude	Longitude	Elevation	Magnetometer	Interpolated Latitude	Interpolated Longitude	Diff Main Field - Mag	Interpolated Base	Interp Base - Interp Base Min	Diurnal Corrected
181	40.51406	-118.28433	1290.7	51938.2	51141.2	51141.2	797.0	51208.3	17.7	779.4
182	40.51403	-118.28198	1296.9	51928.2	51141.1	51141.1	787.1	51210.9	20.2	766.8
183	40.51408	-118.27731	1314.9	51871.0	51141.2	51141.2	729.8	51220.4	29.7	700.1
184	40.51405	-118.27476	1324.6	51954.0	51141.1	51141.1	812.9	51219.7	29.0	783.8
185	40.51412	-118.27253	1336.8	51754.0	51141.2	51141.2	612.8	51219.4	28.8	584.0
186	40.51418	-118.27020	1345.0	51887.0	51141.2	51141.2	745.8	51218.0	27.3	718.4
187	40.51413	-118.26780	1351.5	51907.0	51141.2	51141.2	765.8	51216.5	25.9	740.0
188	40.51413	-118.26550	1361.9	51908.0	51141.2	51141.2	766.8	51218.4	27.7	739.1
189	40.51429	-118.26256	1373.6	51794.0	51141.3	51141.3	652.7	51220.0	29.4	623.4
190	40.51424	-118.26077	1384.8	51870.0	51141.3	51141.3	728.7	51219.9	29.3	699.5
191	40.51417	-118.25817	1399.5	51893.5	51141.2	51141.2	752.3	51218.8	28.2	724.1
192	40.51571	-118.29136	1272.7	51952.0	51142.1	51142.1	809.9	51195.5	4.8	805.1
193	40.51570	-118.28900	1279.8	51914.8	51142.1	51142.1	772.7	51196.2	5.5	767.2
194	40.51573	-118.28669	1285.5	51911.2	51142.1	51142.1	769.1	51200.6	9.9	759.2
195	40.51580	-118.28421	1292.5	51885.0	51142.1	51142.1	742.9	51207.3	16.7	726.2
196	40.51582	-118.28201	1298.1	51866.0	51142.1	51142.1	723.9	51206.9	16.3	707.6
197	40.51754	-118.29141	1273.5	52003.0	51143.1	51143.1	859.9	51243.6	52.9	807.0
198	40.51754	-118.28916	1278.8	51875.0	51143.1	51143.1	731.9	51237.8	47.1	684.8
199	40.51757	-118.28659	1284.7	51856.0	51143.1	51143.1	712.9	51232.0	41.4	671.5
200	40.51761	-118.28438	1292.3	51791.0	51143.1	51143.1	647.9	51224.9	34.3	613.6
201	40.51767	-118.28195	1299.2	51858.0	51143.2	51143.2	714.8	51215.9	25.2	689.6
202	40.51948	-118.27252	1331.7	51899.0	51144.2	51144.2	754.8	51225.3	34.6	720.2
203	40.51951	-118.27019	1346.0	51960.0	51144.2	51144.2	815.8	51227.5	36.8	779.0
204	40.51959	-118.26776	1356.9	51860.0	51144.3	51144.3	715.7	51229.5	38.8	676.9
205	40.51972	-118.26552	1363.3	51878.0	51144.3	51144.3	733.7	51230.3	39.6	694.1
206	40.51962	-118.26320	1372.6	51822.0	51144.3	51144.3	677.7	51230.0	39.4	638.4
207	40.51972	-118.26066	1382.1	51882.0	51144.3	51144.3	737.7	51230.2	39.5	698.2
208	40.52138	-118.27503	1327.9	51894.8	51145.3	51145.3	749.5	51225.2	34.5	715.0
209	40.52128	-118.27260	1335.3	51898.1	51145.2	51145.2	752.9	51230.6	39.9	713.0
210	40.52128	-118.27023	1344.7	51918.2	51145.2	51145.2	773.0	51233.6	42.9	730.1
211	40.52137	-118.26778	1364.7	51936.7	51145.3	51145.3	791.4	51239.1	48.4	743.0

Table 4. (Cont.)

Station	Latitude	Longitude	Elevation	Magnetometer	Interpolated Latitude	Interpolated Longitude	Diff Main Field - Mag	Interpolated Base	Interp Base - Interp Base Min	Diurnal Corrected
212	40.52143	-118.26564	1369.7	51829.0	51145.3	51145.3	683.7	51233.8	43.2	640.5
213	40.52142	-118.26324	1379.7	51884.0	51145.3	51145.3	738.7	51232.1	41.4	697.3
214	40.52142	-118.26089	1387.7	51833.0	51145.3	51145.3	687.7	51231.1	40.4	647.3
215	40.55205	-118.27093	1314.7	51931.7	51162.5	51162.5	769.2	51201.5	10.8	758.4
216	40.55207	-118.26622	1338.7	51958.6	51162.5	51162.5	796.1	51198.5	7.9	788.3
217	40.55552	-118.27094	1312.7	51924.0	51164.4	51164.4	759.6	51219.1	28.5	731.1
218	40.55566	-118.26618	1336.6	51938.0	51164.5	51164.5	773.5	51222.0	31.3	742.2
219	40.55568	-118.26143	1365.8	51948.0	51164.5	51164.5	783.5	51198.0	7.4	776.1
220	40.55915	-118.27102	1307.9	51898.0	51166.4	51166.4	731.6	51225.5	34.8	696.7
221	40.55920	-118.26623	1324.1	51847.0	51166.5	51166.5	680.5	51225.6	34.9	645.6
222	40.55924	-118.26229	1346.4	52001.7	51166.5	51166.5	835.2	51202.7	12.0	823.2
223	40.56279	-118.27105	1298.6	51949.0	51168.5	51168.5	780.5	51213.2	22.5	758.0
224	40.56294	-118.26633	1317.6	51910.1	51168.6	51168.6	741.5	51209.0	18.4	723.2
225	40.56289	-118.26150	1342.5	51981.4	51168.5	51168.5	812.9	51202.0	11.3	801.5
227	40.56804	-118.28556	1254.1	51769.0	51171.4	51171.4	597.6	51236.7	46.0	551.6
228	40.57157	-118.29006	1247.0	51849.0	51173.4	51173.4	675.6	51242.0	51.4	624.2
229	40.57163	-118.28538	1252.6	51983.0	51173.4	51173.4	809.6	51233.5	42.8	766.7
230	40.57172	-118.28076	1260.4	51751.0	51173.5	51173.5	577.5	51233.5	42.8	534.7
231	40.57524	-118.29015	1243.3	51944.0	51175.5	51175.5	768.5	51243.3	52.7	715.9
232	40.57529	-118.28549	1246.4	51938.0	51175.5	51175.5	762.5	51244.7	54.0	708.5
233	40.57530	-118.28076	1258.8	51849.0	51175.5	51175.5	673.5	51241.0	50.3	623.2
234	40.57531	-118.27604	1267.9	51956.0	51175.5	51175.5	780.5	51240.4	49.7	730.8
235	40.57882	-118.29024	1245.1	51884.0	51177.5	51177.5	706.5	51235.0	44.4	662.1
236	40.57878	-118.28545	1246.3	51979.0	51177.4	51177.4	801.6	51236.6	45.9	755.6
237	40.57896	-118.28078	1251.4	51660.0	51177.5	51177.5	482.5	51237.2	46.6	435.9
238	40.57892	-118.27611	1260.5	51987.0	51177.5	51177.5	809.5	51239.5	48.8	760.7
239	40.58238	-118.29042	1245.8	51670.0	51179.5	51179.5	490.5	51234.4	43.8	446.8
240	40.58247	-118.28563	1251.1	51978.0	51179.5	51179.5	798.5	51233.4	42.8	755.7
241	40.58252	-118.28097	1251.0	51990.0	51179.5	51179.5	810.5	51232.1	41.4	769.0
242	40.58254	-118.27616	1259.0	51860.0	51179.6	51179.6	680.4	51231.1	40.4	640.0
243	40.58600	-118.29035	1245.3	51980.0	51181.5	51181.5	798.5	51223.9	33.2	765.3

Table 4. (Cont.)

Station	Latitude	Longitude	Elevation	Magnetometer	Interpolated Latitude	Interpolated Longitude	Diff Main Field - Mag	Interpolated Base	Interp Base - Interp Base Min	Diurnal Corrected
244	40.58603	-118.28563	1246.3	51995.0	51181.5	51181.5	813.5	51225.4	34.7	778.8
245	40.58498	-118.28094	1248.1	51940.0	51180.9	51180.9	759.1	51230.3	39.7	719.4
247	40.58957	-118.29043	1244.9	51995.0	51183.5	51183.5	811.5	51227.1	36.4	775.1
248	40.58962	-118.28577	1245.4	52007.0	51183.5	51183.5	823.5	51228.8	38.2	785.3
249	40.58983	-118.28096	1248.4	51989.0	51183.6	51183.6	805.4	51241.6	50.9	754.4
250	40.58974	-118.27629	1250.8	51806.0	51183.6	51183.6	622.4	51228.5	37.9	584.5
251	40.59320	-118.29052	1243.8	51987.2	51185.5	51185.5	801.7	51229.5	38.8	762.8
252	40.59330	-118.28572	1248.1	51987.0	51185.6	51185.6	801.4	51231.3	40.7	760.7
253	40.59330	-118.28118	1246.0	51966.0	51185.6	51185.6	780.4	51233.8	43.2	737.2
254	40.59355	-118.27621	1245.8	51932.0	51185.7	51185.7	746.3	51234.9	44.3	702.0
255	40.59338	-118.27178	1252.2	51991.7	51185.6	51185.6	806.1	51235.6	45.0	761.1
256	40.59342	-118.26703	1253.3	51975.8	51185.7	51185.7	790.1	51236.3	45.6	744.5
257	40.59678	-118.29053	1245.0	51919.0	51187.5	51187.5	731.5	51243.4	52.7	678.8
258	40.59685	-118.28596	1250.0	51860.0	51187.6	51187.6	672.4	51212.7	22.1	650.4
259	40.59664	-118.28151	1238.6	51949.5	51187.5	51187.5	762.0	51237.8	47.2	714.9
260	40.59701	-118.27640	1239.8	51844.8	51187.7	51187.7	657.1	51238.1	47.4	609.7
261	40.59690	-118.27168	1242.8	51985.3	51187.6	51187.6	797.7	51237.2	46.6	751.1
262	40.59698	-118.26700	1248.8	52010.9	51187.7	51187.7	823.2	51236.4	45.7	777.5
263	40.60040	-118.29066	1242.8	51957.0	51189.6	51189.6	767.4	51230.3	39.6	727.8
264	40.60047	-118.28596	1243.8	51970.0	51189.6	51189.6	780.4	51227.6	37.0	743.4
265	40.60050	-118.28119	1247.7	51926.0	51189.6	51189.6	736.4	51226.0	35.3	701.1
266	40.60056	-118.27649	1247.5	51955.0	51189.7	51189.7	765.3	51224.3	33.7	731.7
267	40.60075	-118.27191	1253.7	51934.0	51189.8	51189.8	744.2	51229.3	38.6	705.6
268	40.60063	-118.26699	1252.7	51816.0	51189.7	51189.7	626.3	51232.3	41.6	584.7
269	40.60398	-118.29071	1241.8	51846.0	51191.6	51191.6	654.4	51212.0	21.3	633.1
270	40.60408	-118.28596	1244.7	51914.0	51191.6	51191.6	722.4	51215.6	25.0	697.4
271	40.60418	-118.28125	1250.3	51800.0	51191.7	51191.7	608.3	51219.8	29.1	579.2
272	40.60418	-118.27656	1248.3	51929.0	51191.7	51191.7	737.3	51223.5	32.9	704.4
273	40.60424	-118.27182	1248.8	51799.0	51191.7	51191.7	607.3	51231.3	40.6	566.7
274	40.60421	-118.26712	1248.3	51932.0	51191.7	51191.7	740.3	51233.0	42.4	697.9
275	40.60761	-118.29077	1243.2	51901.0	51193.6	51193.6	707.4	51213.4	22.7	684.7

Table 4. (Cont.)

Station	Latitude	Longitude	Elevation	Magnetometer	Interpolated Latitude	Interpolated Longitude	Diff Main Field - Mag	Interpolated Base	Interp Base - Interp Base Min	Diurnal Corrected
276	40.60765	-118.28605	1241.1	51953.0	51193.6	51193.6	759.4	51214.5	23.8	735.6
277	40.60773	-118.28133	1245.3	51966.0	51193.7	51193.7	772.3	51220.7	30.1	742.2
278	40.60778	-118.27659	1246.0	51987.0	51193.7	51193.7	793.3	51221.9	31.2	762.0
279	40.60782	-118.27184	1245.0	51996.0	51193.7	51193.7	802.3	51233.8	43.2	759.1
280	40.60784	-118.26714	1247.8	51910.0	51193.7	51193.7	716.3	51233.7	43.0	673.3

REFERENCES

- Albers, J.P., 1965, Tertiary and Quaternary Rocks, in: Mineral and Water Resources of Nevada, Nevada Bureau of Mines Bulletin 65, p. 30-32.
- Benoit, W.R., and Butler, R.W., 1983, A review of high-temperature geothermal developments in the Northern Basin and Range Province: Geothermal Resources Council Special Report No. 13, p. 62-63.
- Blackwell, D.D., Wisian, K.W., Benoit, D., and Gollan, B., 1999, Structure of the Dixie Valley geothermal system, a "typical" Basin and Range geothermal system, from thermal and gravity data: Geothermal Resources Council Transactions, v. 23, p. 5225-531.
- Blackwell, D.D., Wisian, K.W., Richards, M.C., Leidig, M., Smith, R., and McKenna, J., 2003, Geothermal Resource Analysis and Structure of Basin and Range Systems especially Dixie Valley Geothermal Field, Nevada; Department of Geological Sciences, Southern Methodist University, Dallas, TX, 62 pp.
- Bullard, E.C., 1936, Gravity measurements in East Africa: Philosophical Transactions of the Royal Society of London, v 235, 757, p. 486-497.
- Burke, D.B., and Silberling, N.J., 1973, The Auld Lang Syne Group of Late Triassic and Jurassic (?) Age of North Central Nevada: U.S. Geological Survey Bulletin 1394-E, 14 pp.
- Calvin, W., Lamb, A., and Kratt, C., 2010, Rapid characterization of drill core and cutting mineralogy using infrared spectroscopy: Geothermal Resources Council Transactions, v. 34, p. 761-764.
- Cogbill, A.H., 1990, Gravity terrain corrections calculated using digital elevation models: Geophysics, v. 55(1), 102-106.
- Croft, G.A., 1872, Croft's Transcontinental Tourist's Guide: George A. Croft, New York, New York, p. 153.

Davis, D.D., 2011, Descriptive logs, skeletonized samples, and photographs of core from Presco Energy's thermal gradient wells P3-1, P10-1, and P32-2 in the Rye Patch area, Pershing County, Nevada: Nevada Bureau of Mines and Geology Open-File Report 11-10 [available online at www.nbmg.unr.edu/dox/of1110.pdf].

Davis, G.A., 1979, Problems of intraplate extensional tectonics, Western United States, with special emphasis on the Great Basin, in: Newman, G.W., and Goode, H.D. (eds.) Basin and Range Symposium and Great Basin Field Conference, Rocky Mountain Association of Geologists, Denver, CO p. 41-54.

Desormier, W.L., 1979, Desert Peak to Humboldt House and Winnemucca, in: Lane, M.A., (ed) Nevada geothermal areas: Desert Peak, Humboldt House, Beoware: Guidebook for field trip #6, Geothermal Resources Council 1979 Annual Meeting, p. 13-17.

Duffrin, B.G., Berger, D.L., and Schaefer, D.H., 1985, Principal facts for gravity stations in the Humboldt House geothermal area, Pershing County, Nevada: U.S. Geological Survey Open-File Report 85-162, 11 pp.

Eaton, G.P., 1979, Regional geophysics, Cenozoic tectonics and geologic resources of the Basin and Range Province and adjoining regions, in: Newman, G.W., and Goode, H.D., (eds) Basin and Range Symposium and Great Basin Field Conference, Rocky Mountain Association of Geologists, Denver, CO, p. 11-39.

Ecker, E., and Mittermayer, E., 1969, Gravity corrections for the influence of the atmosphere: Bulletin of Theoretical and Applied Geophysics, v. 11, p. 70-80.

Ehni, W.J., 2001, Identification of high angle structures controlling the geothermal system at Rye Patch, Nevada: EOS Transactions, American Geophysical Union, 82(47) Fall Meeting Supplement, Abstract T22A-0905, p. 1144.

Ellis, R.K., 2011, A restated conceptual model for the Humboldt House-Rye Patch geothermal resource area, Pershing County, Nevada: Geothermal Resources Council Transactions, v. 35, p. 769-776.

Faulds, J.E., and Varga, R.J., 1998, The role of accommodation zones and transfer zones in the regional segmentation of extended terranes, in: Faulds, J.E., and Stewart, J.H. (eds.), Accommodation Zones and Transfer Zones and the Regional Segmentation of the Basin and Range Province, Geological Society of America Special Paper 303, p. 1-45.

Feighner, M.A., Daley, T.M., and Majer, E.L., 1998, Results of vertical seismic profiling at Well 46-28, Rye Patch geothermal field, Pershing County, Nevada: Lawrence Berkeley National Laboratory Report LBNL-41800, 16 pp.

- Feighner, M.A., Gritto, R., Daley, T.M., Keers, H. and Majer, E.L., 1999, Three-dimensional seismic imaging of the Rye Patch geothermal reservoir: Lawrence Berkeley National Laboratory Report LBNL-44119, 39 pp.
- Flynn, T., and Buchanan, P.K., 1990, Geothermal fluid genesis in the Great Basin; U.S. Department of Energy Idaho Operations Office, DOE/ID/12784-1, 154 pp.
- Fournier, R.O., 1981, Application of water geochemistry to geothermal exploration and reservoir engineering, in: Rybach, L., and Muffler, L.J.P. (eds), Geothermal Systems: Principles and Case Histories, Wiley and Sons, New York, NY, p. 109-143.
- Garside, L.J., and Schilling, J.H., 1979, Thermal waters of Nevada: Nevada Bureau of Mines and Geology Bulletin 91, 159 pp.
- Geometrics, 2011, MagMap 2000[®] version 4.94: San Jose, CA.
- Geosoft, 2009, GM-SYS[®] Profile Modeling software version 4.1: Toronto, Ontario, Canada.
- Godwin, L.H., Haigler, L.B., Rioux, R.I., White, D.E., Muffler, L.J.P., and Wayland, R.G., 1971, Classification of public lands valuable for geothermal steam and associated geothermal resources: U.S. Geological Survey Circular 647, 18 pp.
- Gritto, R., Daley, T.M., and Majer, E.L., 2000, Seismic mapping of the subsurface structure at the Rye Patch geothermal reservoir: Lawrence Berkeley National Laboratory Report LBNL-47032, 25 pp.
- Gritto, R., Daley, T.M., and Majer, E.L., 2001, A model of the subsurface structure at the Rye Patch geothermal reservoir based on surface-to-borehole seismic data: Geothermal Resources Council Transactions, v. 25, p. 405-409.
- Gritto, R., Daley, T.M., and Majer, E.L., 2002, Integrated seismic studies at the Rye Patch geothermal reservoir: Geothermal Resources Council Transactions, v. 26, p. 431-445.
- Gritto, R., Daley, T.M., and Majer, E.L., 2003, Estimating subsurface topography from surface-to-borehole seismic studies at the Rye Patch geothermal reservoir, Nevada, USA: Geothermics, v. 32, p. 275-295.
- Golden Software, 2002, SURFER[®], v. 9: Golden, CO.
- Hammer, S., 1939, Terrain corrections for gravimeter stations: Geophysics, 4, p. 184-194.

Hastings, J.S., Burkhart, T.H., and Richardson, R.E., 1993, Geology of the Florida Canyon gold deposit, Pershing County, Nevada, in: Gold and Silver Deposits of Western Nevada, Geological Society of Nevada 1993 fall field trip guidebook, September 25 and 26, 1993, Special Publication no. 18, p. 433-452.

Hildenbrand, T.G., 1983, FFTFIL: A filtering program based on two-dimensional Fourier analysis of geophysical data: U.S. Geological Survey Open-File Report 83-287, 60 pp.

Hinze, W., Aiken, C., Brozena, J., Coakley, B., Dater, D., Flanagan, G., Forsberg, R., Hildenbrand, T., Keller, G., Kellogg, J., Kucks, R., Li, X., Mainville, A., Morin, R., Pilkington, M., Plouff, D., Ravat, D., Roman, D., Urrutia-Fucugauchi, J., Véronneau, M., Webring, M., and Winester, D., 2005, New standards for reducing gravity data: The North American gravity database: *Geophysics*, v. 70, no. 4, p. J25-J32.

Holom, D.I., and Oldow, J.S., 2007, Gravity reduction spreadsheet to calculate the Bouguer anomaly using standardized methods and constants: *Geosphere*, v. 3, no. 2, p. 86-90.

Hunt, C.B., 1979, The Great Basin, an overview and hypotheses of its history, in: Newman, G.W., and Goode, H.D., (eds) Basin and Range Symposium and Great Basin Field Conference, Rocky Mountain Association of Geologists, Denver, CO, p. 11-39.

INTERMAGNET, Geomagnetic Data, available at: <http://www.intermagnet.org/data-donnee/download-eng.php> (accessed November 12, 2012).

Johnson, J.L., 2003, Characterization of past hydrothermal fluids in the Humboldt House geothermal area, Pershing County, Nevada - geochemical and paragenetic studies of core samples: unpublished Master's Thesis, University of Nevada Reno.

Johnson, J.L., Tempel, R.N., and Shevenell, L.A., 2004, Characterization of past hydrothermal fluids in the Humboldt House geothermal area, Pershing County, Nevada - geochemical and paragenetic studies of core samples (abstract), *Geological Society of America Abstracts with Programs*, v. 35, no. 6, p. 148.

Johnson, M.G., 1977, Geology and mineral deposits of Pershing County, Nevada: Nevada Bureau of Mines and Geology, Bulletin 89, 115 pp.

Lachenbruch, A.H., and Sass, J.H., 1977, Heat flow in the United States and the thermal regime of the crust, in: Heacock, J.G., (ed.) *The Earth's Crust: American Geophysical Union Monograph 20*, p. 626-675.

Lachenbruch, A.H., and Sass, J.H., 1978, Models of an extending lithosphere and heat flow in the Basin and Range Province, in: Smith, R.B., and Eaton, G.P., (eds.) Cenozoic tectonics and regional geophysics of the western Cordillera: Geological Society of America Memoir 152, p. 209-250.

LaFehr, T.R., 1991, An exact solution for the gravity curvature (Bullard B) correction: *Geophysics*, v. 56, no. 8, p. 1179-1184.

Long, C.L., and Batzle, M.L., 1976, Station location map and audio-magnetotelluric data log for Rye Patch known geothermal resource area, Nevada: U.S. Geological Survey Open-File Report 76-700C, 4 pp.

Longman, I.M. 1959, Formulas for computing the tidal acceleration due to the Moon and the Sun: *Journal of Geophysical Research*, v. 64, p. 2351-2355.

Lyatsky, H., 2004, Detection of subtle basement faults with gravity and magnetic data in the Alberta Basin, Canada: a data-use tutorial: *The Leading Edge*, v. 23, no. 12, p. 1282-1288.

MacKnight, R.B., Silver, E.A., Kennedy-Bowdoin, T., and Pickles, W.L., 2005, Evidence for the structurally controlled deposition of hot spring and fumarolic minerals at the Humboldt House, Nevada: *Geothermal Resources Council Transactions*, v. 29, p. 397-400.

Mansure, A.J., Westmoreland, J.J., Staller, G.E., Jacobson, R.D., Libengood, H., Smith, E., Galbreath D., and Rickard, W.M., 2001, Polyurethane grouting of Rye Patch lost circulation zone: *Geothermal Resources Council Transactions*, v. 25, p. 109-113.

MEGSYSTEMS Ltd., Tide correction utility (tide tables) available at: www.megsystems.ca/webapps/tidecorr/tidecorr.aspx, accessed June 1, 2012.

Michels, D., 2002, Rye Patch geothermal development, hydro-chemistry of thermal water applied to resource definition: Report to Presco Energy, 33 pp.

Miller, E.L., Miller, M.M., Stevens, C.H., Wright, J.E., and Madrid, R., 1992, Late Paleozoic paleogeographic and tectonic evolution of the western U.S. Cordillera, in: Burchfiel, B.C., Lipman, P.W., and Zobach, M.L., (eds.) *The Cordilleran Orogen: Conterminous U.S.*, Geological Society of America, Boulder Colorado, p. 57-106.

Muffler, L.J.P. (ed.), 1978, Assessment of the geothermal resources of the United States: USGS Circular 790, 163 pp.

National Oceanic and Atmospheric Administration (NOAA), National Geophysical Data Center Magnetic Field Calculator: available online at <http://ngdc.noaa.gov/geomag-web/#igrfgrid> (accessed November 12, 2012).

Nevada Bureau of Mines and Geology, 2003, Drilling report - exploratory drilling program to evaluate the lifetime and current potential of the Florida Canyon geothermal system, Pershing County, Nevada: available online at <http://www.nbmng.unr.edu/geothermal/ryepatchdrilling.pdf>, (accessed April 21, 2013).

Nevada Bureau of Mines and Geology, 2005, Report of the Rye Patch (Humboldt House Geothermal Area, available on line at <http://www.nbmng.unr.edu/Geothermal/site.php?sid=Rye%20Patch>, (accessed April 21, 2013).

Nevada Bureau of Mines and Geology, 2012, Geothermal/Geochemical Database: available online at http://www.nbmng.unr.edu/Geothermal/12A26rp_NGDSschema.xlsx, (accessed May, 13, 2013).

Nettleton, L.L. 1971, Elementary gravity and magnetics for geologists and seismologists: Society of Exploration Geophysicists, Monograph Series No. 1, 121 pp.

Nowell, D.A.G., 1977, Gravity terrain corrections – an overview: *Journal of Applied Geophysics*, v. 42, p. 117-134.

Olcutt, G.W., and Spruck, W.H., 1961, Areal economic geology of T32N, R33 and 34E, M.D.M: Land Department, Southern Pacific Co., unpublished map.

Parasnis, D.S., 1979, Principles of Applied Geophysics: Chapman and Hall, London, United Kingdom, 275 pp.

Plouff, D., 1966, Digital terrain corrections based upon geographic coordinates [abstract]: *Geophysics*, v. 31, 1208.

Poole, F.G., Stewart, J.H., Palmer, A.R., Sandberg, C.A., Madrid, R.J., Ross, R.J., Hintze, L.F., Miller, M.M., and Wrucke, C.T., 1992, Latest Precambrian to latest Devonian time; development of a continental margin, in: Burchfiel, B.C., Lipman, P.W., and Zobach, M.L., (eds.) *The Cordilleran Orogen: Conterminous U.S.*, Geological Society of America, Boulder Colorado, p. 9-56.

Price, J.G., 2002, *Geology of Nevada: The Professional Geologist*, v. 39, no. 4, p. 2-8.

Reed, M.J., and Mariner, R.H., 2007, Geothermometer calculations for geothermal assessment: *Geothermal Resources Council Transactions*, v. 31, p. 89-92.

- Reynolds, J.M., 1997, An introduction to applied and environmental geophysics: John Wiley & Sons, New York, NY, 796 pp.
- Richards, M.C. and Blackwell, D.D., 2002, A difficult search, why Basin and Range systems are hard to find; Geothermal Resources Council Bulletin, v. 31, no. 4, p. 143-146.
- Roberts, R.J., 1965, Paleozoic Rocks, in: Mineral and Water Resources of Nevada, Nevada Bureau of Mines Bulletin 65, p. 22-26.
- Robinson, E.S., and Coruh, C., 1988, Basic Exploration Geophysics: John Wiley and Sons, New York, NY, 562 pp.
- Rowan, L.C., and Wetlaufer, P.H., 1981, Geologic evaluation of major LANDSAT lineaments in Nevada and their relationship to ore districts: U.S. Geological Survey Open-file Report 79-544, 64 pp.
- Saleeby, J.B., and Busby-Spera, C., 1992, Early Mesozoic tectonic evolution of the western U.S. Cordillera, in: Burchfiel, B.C., Lipman, P.W., and Zobach, M.L., (eds.) The Cordilleran Orogen: Conterminous U.S., Geological Society of America, Boulder Colorado, p. 107-168.
- Sanyal, S.K., McNitt, J.R., Butler, S.J., Klein, C.W., and Ellis, R.K., 2006, Assessing the Rye Patch geothermal field, a classic Basin-and-Range Resource: Geothermal Resources Council Transactions, v. 30, p. 97-104.
- Schaefer, D.H., 1986, Bouguer gravity anomalies, depth to bedrock, and shallow temperature in the Humboldt House geothermal area, Pershing County, Nevada: U.S. Geological Survey Miscellaneous Investigations Map I-1701, 1 Sheet.
- Sharma, P.V., 1997, Environmental and Engineering Geophysics, Cambridge University Press, Cambridge, United Kingdom
- Sibbett, B.S., and Glenn, W.E., 1981, Lithology and well log study of Campbell "E-2" geothermal test well, Humboldt House geothermal prospect, Pershing County, Nevada: University of Utah Research Institute, Earth Science Lab Report 53, 17 pp.
- Silberling, N.J., and Wallace, R.E., 1969, Stratigraphy of the Star Peak Group (Triassic) and overlying lower Mesozoic rocks, Humboldt Range, Nevada: U. S. Geological Survey Professional Paper 592, 50 pp.
- Silberman, M.L., 1983, Geochronology of hydrothermal alteration and mineralization: Tertiary epithermal precious metal deposits in the Great Basin: Geothermal Resources Council Special Report 13, p. 287-303.

Silver, E.A., MacKnight, R.B., Male, E., Pickles, W.L., Cocks, P., and Waibel, A., 2011, LiDAR and hyperspectral analysis of mineral alteration and faulting on the west side of the Humboldt Range, Nevada: *Geosphere*, v. 7, no. 6, p. 1357-1368.

Smith, R.P., 2003 A geothermal exploration strategy using high-resolution aeromagnetic surveys for the Basin and Range Province: *Proceedings, Twenty-eighth Workshop on Geothermal Reservoir Engineering*, Stanford University, Stanford, CA, 6 pp.

Stewart, J.H., 1998, Regional characteristics, tilt domains, and extensional history of the Late Cenozoic Basin and Range Province, Western North America, in: *Accommodation Zones and Transfer Zones and the Regional Segmentation of the Basin and Range Province*, Faulds, J.E., and Stewart, J.H. (eds.) Geological Society of America Special Paper 303, p. 47-74.

Stanley, J.M., 1977, Simplified gravity interpretation by gradients - the geological contact: *Geophysics*, v. 42, p. 1230 - 1235.

Strecker, U., Smithson, S.B., and Steidtmann, J.R., 1996, Cenozoic basin extension beneath Goshute Valley, Nevada: *Geological Society of America Special Paper 303*, p. 15-26.

Telford, W.M., Geldart, L.P., Sheriff, R.E., and Keys, D.A., 1976, *Applied Geophysics*, Cambridge University Press, Cambridge, England, 860 pp.

Teplov, B., 1999, Integrated geophysical exploration program at the Rye Patch geothermal field, Pershing County, Nevada: *Final Report to Mt. Wheeler Power*.

Thomas, H.E., 1964, *Mineral and Water Resources of Nevada*, Nevada Bureau of Mines and Geology Bulletin 65, 314 pp.

Trimble® Navigation Systems Limited, 2012, Trimble® Business Center software, version 2.70, Dayton, OH.

Vandenburg, W.O., 1936, *Mines of Pershing County, Nevada*: U.S. Bureau of Mines Information Circular 6995, 54 pp.

Waibel, A., Blackwell, D.D., and Ellis, R.K., 2003, The Humboldt House-Rye Patch geothermal district: an interim view: *Geothermal Resources Council Transactions*, v. 27, p. 33-36.

Wallace, R.E., 1964, *Mineral and Water Resources of Nevada*, Nevada Bureau of Mines and Geology Bulletin 65, 314 pp.

Wallace, A.R., Perkins, M.E., and Fleck, R.J., 2008, Late Cenozoic paleogeographic evolution of northeastern Nevada: evidence from sedimentary basins: *Geosphere*, v.4, p. 36-74.

Warpinski, N.R., Sattler, A.R., Fortuna, R., Sanchez, D.A., and Nathwani, J., 2004 Geothermal resource exploration and definition projects: *Geothermal Resources Council Transactions*, v. 28, p. 373-377.

Williams, C.F., Reed, M.J., and Mariner, R.H., 2008, A review of methods applied by the U.S. Geological Survey in the assessment of identified geothermal resources: U.S. Geological Survey Open-File Report 2008-1296, 27 pp.